CFD study of induction and finite blade effect on a floating horizontal-axis wind turbine

Arianna Sala

TU Delft

CFD study of induction and finite blade effect on a floating horizontal-axis wind turbine

by

Arianna Sala

to obtain the degree of Master of Science
at the Delft University of Technology,
to be defended publicly on Wednesday November 24, 2021 at 09:30 AM.

Student number:	5147700	
Project duration:	February 8, 2021 – November 24, 2021	
Thesis committee:	Prof. dr. ir. C.J. Simão Ferreira,	TU Delft
	Dr. W. Yu,	TU Delft
	Dr. ir. A.C. Viré,	TU Delft
	Dr. ir. A.H. van Zuijlen	TU Delft

An electronic version of this thesis is available at http://repository.tudelft.nl/.

TU Delft

Abstract

As the need for abundant and reliable renewable energy increases, there is a growing interest in floating wind turbines, which would allow to harness the wind resource in areas where bottom-founded wind turbines cannot be used. However, the movements of the platform are expected to cause unsteady aerodynamics effects, including different wake dynamics, a variation of the induction field at the rotor and blade-vortex interactions. The effects of these phenomena are not clearly understood yet and there is no general consensus on whether Blade-Element Momentum (BEM) codes could be employed to model the aerodynamics of a floating wind turbine with an acceptable level of accuracy. This poses a serious issue as BEM models present the lowest computational cost among the methods for the analysis of rotor aerodynamics and are thus widely used in industry practice.

This project proposes to analyze the impact of surge motion on the induction field of a horizontal-axis wind turbine. This is done by developing first a suitable actuator disc model, then an actuator line model that allows to study the effect of the finite number of blades on this induction field. Both models are implemented in OpenFOAM, an open-source CFD software, and are extensively validated against momentum theory. The simulations are run for a range of case studies with imposed baseline thrust, amplitude of the thrust variations, surge frequency and surge amplitude, allowing to separate the effects of the thrust variations to the effect of the change in position of the disc. The resulting induction factors are compared to those obtained with a dynamic inflow model, to assess whether a momentum method could lead to accurate predictions. Particular attention is given to the identification of the wake state of the streamtube, since both turbulent wake state and vortex ring state imply a breakdown of momentum theory.

The results of the actuator disc simulations show that the impact of the thrust variations on the induction field decreases as their frequency increases, since the flow does not have time to adapt to the load changes. The impact of the disc motion, on the contrary, increases as its frequency increases since the rotor moves faster than its wake and the rotor-wake interactions are stronger. The surge motion and the thrust coefficient variations cause oscillations of the induction factor that are out of phase and partly cancel each other out when combined, as would happen in real wind turbines. In all cases, there is a good agreement with the induction factors obtained with the examined dynamic inflow model, although for high baseline thrusts the average induction predicted with the CFD model is slightly lower than the one obtained with the dynamic inflow model.

The analysis of the velocity, vorticity and pressure fields of the actuator disc simulations show that turbulent wake state is only entered when a high thrust coefficient is reached at low frequencies, while propeller state is only entered when a negative thrust coefficient is reached at low frequencies. It is expected that in real wind turbines such extreme values of the thrust will be reached at frequencies high enough to keep the streamtube in windmill state. Furthermore, no signs of vortex ring state were detected. This gives confidence in the possibility of using momentum methods for the aerodynamic modelling of floating wind turbines.

Some of the cases considered during the first part of the project were also run with the actuator line model, to study the effect of the finite number of blades on the flow field. A rotor with three blades was modelled. The resulting disc average induction factors are in excellent agreement with those obtained with the actuator disc model, while the induction at the disc center is lower. The contour plots show that the conclusions on the wake states entered by the streamtube remain valid. It is advised to test this model at different tip speed ratios and for rotors with different numbers of blades, to further assess the influence of the finite number of blades.

Overall, this project contributes to a better understanding of the aerodynamics of floating wind turbines and gives confidence in the possibility of using momentum methods during their design phase. Furthermore, the CFD models developed are a flexible tool that may be used for future research on related topics.

Acknowledgements

Writing a thesis is always a challenging task, and even more so during a global pandemic. Despite the difficulties that working from home for many months poses, I was lucky to have a project I enjoyed and the support of many people, to whom I would like to express my gratitude.

First of all, I would like thank to professor Carlos Simão Ferreira, who proposed me this thesis topic and gave me precious suggestions for the entire duration of the project. I also want to thank Dr. Wei Yu, who was always available to help and guide me and with whom it was a pleasure to collaborate. Furthermore, I am thankful to Dr. Axelle Viré for her disponibility in being part of my group of supervisors. Another person who helped me a lot is Dr. Delphine de Tavernier, whose suggestions were vital when I was desperately trying to get the models working.

The support of all my friends was also very important. A special thanks goes to Federica: our weekly chats about our theses (and many other topics) were very precious to me during the long months of lockdown, and knowing that I could always ask her for an opinion was priceless in many occasions. I would also like to thank Fabrizio for taking the time to read all my literature review, for his valuable feedback and for all the support in the delicate final phase of this project.

It is not possible to express in a few lines the gratitude I owe to my family, but I will try. First of all, my Dutch adventure would not have been possible without my uncles Susi and Alberto, who welcomed me in their home. Also, thanks to my cousins Alessandro and Alice who as TU Delft alumni inspired me in pursuing a master there and guided me. Last but not least, I want to thank my parents, who had to deal with my moods during the last nine months and never got tired of encouraging me.

Arianna Sala
Biella, October 2021

Contents

List of Figures

List of Tables

Nomenclature

List of acronyms

BEM Blade Element Momentum theory

CFD Computational Fluid Dynamics

DNS Direct Numerical Simulations

DoF Degree of Freedom

FOWT Floating Offshore Wind Turbine

FVW Free Vortex Wake method

GHGs Greenhouse Gases

LES Large Eddy Simulations

RANS Reynold-Averaged Navier-Stokes

TLP Tension Leg Platform

TSR Tip Speed Ratio

WInDS Wake Induced Dynamics Simulator (free vortex wake code developed by Sebastian and Lackner [46])

List of symbols

α Angle of attack [°]

ΔC_T Amplitude of thrust coefficient oscillations [-]

Γ_b Bound circulation [m^2/s]

ν Kinematic viscosity [m^2/s]

ω Frequency of the sinusoid that describes the platform motion [rad/s]

ω_c Characteristic frequency to characterize the unsteadiness of a flow [rad/s]

ω_{red} Reduced motion frequency [-]

Φ Phase of the sinusoid that describes the platform motion [rad]

$\boldsymbol{\mathcal{F}}$ External force [N]

ρ Air density [kg/m^3]

$\mathbf{u_d}$ Spatial average of the velocity in the actuator disc cells in am OpenFOAM simulation using *ActuationDiskSource* class [m/s]

$\mathbf{u_m}$ Spatial average of the velocity in the cells in the monitored region in an OpenFOAM simulation using *ActuationDiskSource* class [m/s]

$\mathbf{u}$ Flow velocity [m/s]

τ Time constant [s]

A Amplitude of the sinusoid that describes the platform motion [m]

a Axial induction factor [-]

a' Tangential induction factor [-]

A_d Actuator disc area [m^2]

A_{red} Reduced motion amplitude [-]

c Characteristic length [m]

C_T Thrust coefficient [-]

C_{T0} Baseline thrust coefficient [-]

D Rotor diameter [m]

f Surge motion frequency [s^{-1}]

F_T Thrust force [N]

f_t Elementary axial force [N/m]

k Reduced frequency to characterize the unsteadiness of a flow [-]

L Lift per unit span [N/m]

$l_{background}$ Length of the sides of the background mesh in CFD simulations [m]

l_{ref} Length of the sides of the inner refinement zone of the mesh in CFD simulations [m]

N_B Number of blades of the rotor

p Flow pressure [N/m^2]

Q Torque [$N \cdot m$]

t Time [s]

U_d Wind speed at the actuator disc [m/s]

U_w Wind speed in the far wake [m/s]

U_∞ Free-stream wind speed [m/s]

U_{in} Induced velocity [m/s]

u_{qs} Quasi-steady induction velocity [m/s]

U_{str} Streamtube wake-convection reference velocity [m/s]

V Velocity of the rotor in 1D motion [m/s]

V_a Axial velocity at the rotor [m/s]

$V_{max,red}$ Reduced maximum motion velocity [-]

V_s Surge motion velocity [m/s]

W Local flow velocity [m^2/s]

x Displacement of rotor in 1D motion [m]

X_{down} Length of the simulations domain in the direction of the rotor axis, downstream of the rotor [m]

X_{ref} Length of the inner refinement zone of the mesh in CFD simulations [m]

X_{up} Length of the simulations domain in the direction of the rotor axis, upstream of the rotor [m]

Y_{inlet} Length of the inlet of the simulations domain in lateral direction [m]

Z_{inlet} Length of the inlet of the simulations domain in vertical direction [m]

1 Introduction

Nowadays, the need to operate a transition towards a more sustainable society is widely recognised. The fossil fuels that currently power the vast majority of human activities lead to the emission of harmful pollutants and greenhouse gases (GHGs), responsible for global warming. In the Paris agreement, it has been agreed to keep the temperature rise "well below 2°C above pre-industrial levels" [39]. The European Union has resolved to reduce the GHGs emissions by 40%, compared to the levels of 1990 [13]. To meet these goals, a major shift in energy production towards renewable technologies is needed. Among these clean technologies, wind energy is expected to play a key role. At present, it is the second renewable energy technology in terms of total installed capacity after hydropower and it is expected to steadily grow over the next decades [21].

As more and more wind power is installed, there is an increasing interest in offshore wind. At the end of 2019, the total capacity installed offshore amounted to 5% of the total global wind capacity [17]. GWEC Marker Intelligence expects that over 205 GW of offshore wind capacity will be added during the next ten years [17]. This shift towards offshore installations presents some clear advantages: winds are generally more stable and faster offshore, and the impact on human activities is lower. However, traditional bottom-founded wind turbines can only be employed where the sea depth is up to 60 m [29]. Due to this limit, the wind resource cannot be harvested in numerous regions with deep coastal waters. This limitation could be overcome by using floating foundations.

Floating Offshore Wind Turbines (FOWTs) employ different typologies of floating foundations and mooring systems, derived from designs used in the oil and gas industry. At present, floating wind has not reached commercial maturity, but numerous prototypes have been created. At the end of 2019, the total installed capacity was 66 MW and predictions for 2030 range from 3 GW to 19 GW [17]. This depends on how much the cost of this technology will decrease in the next years, which in turn is linked to the technical challenges that wind turbines on floating foundations present.

In this chapter, a brief summary of the state of the art of floating wind is first given in section 1.1. Next, the perspective of this research project is presented in section 1.2. Finally, in section 1.3 the research questions of the project are listed and the outline of the present report is given.

1.1. State of the art of floating wind

The idea of using floating foundations for wind turbines was first proposed by Heronemus in 1972 [20]. However, it was only in the 90s that energy began being produced with bottom-founded offshore wind turbines [56]. In the same period, the FLOAT project was launched, which lead to the realization of a model test for a floating wind turbine [56]. Many more model tests were conducted, and since 2009 full-scale prototypes have also been constructed [56]. The first one was the Hywind project (2009), followed by WindFloat (2011), VERTIWIND (2016) and SeaReed (2018), among others [29]. So far, the design of the projects was conservative to reduce the risks, and this increased the costs [8]. The challenge is thus to develop a methodology for a cost-effective design of floating wind turbines. This task is complicated by the fact that the system is composed of two parts, the floating platform and the wind turbine, strongly linked to one another.

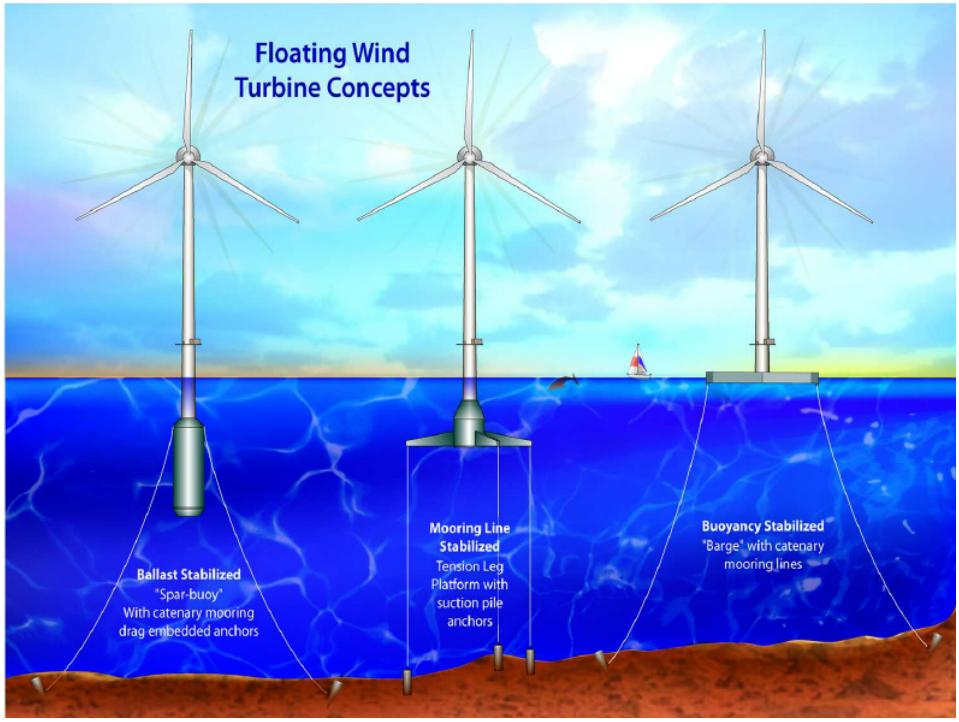

Figure 1.1: Illustration of the three main types of floating platforms: from right to left, spar-buoy, tension leg platform and semi-submersible. Taken from [5].

In the past years, many concepts have been proposed for the floating platform. These concepts can be divided into three groups, based on the strategy used to achieve stability [5]:

- **Spar-buoy** - ballast stabilized: this platform is stable because its centre of gravity is lower than the center of buoyancy. The structure is usually cylindrical and ballast weights are added in its lower part.
- **Tension Leg Platform (TLP)** - mooring line stabilized: this platform achieves stability through mooring line tension.
- **Semi-submersible platform** - buoyancy stabilized: as the name suggests, platforms of these types float semi-submerged. They are stabilized by distributed buoyancy.

These three concepts are illustrated in figure 1.1. In practice, the proposed concepts use all three methods to gain stability, but one method usually prevails over the others [29]. Each of the three typologies presents advantages and disadvantages. The TLP platform is expected to be the steadiest, while the semi-submersible platform is likely to be subjected to higher wave loading [29], which translates in increased motions of the whole system. These motions constitute the main difference between bottom-founded and floating substructures.

1.2. Thesis perspective

The motions of the floating platform affect the aerodynamics of the floating wind turbine. These motions comprise six degrees of freedom, three transitional and three rotational. The transitional degrees of freedom are: surge in the axial direction, sway in the lateral direction and heave in the vertical direction, while the rotational degrees of freedom are: roll about the axial axis, pitch about the lateral axis and yaw about the vertical axis [59]. Figure 1.2 shows a representation of a floating wind turbine with its six degrees of freedom.

At the rotor, the platform motions cause a variation of the apparent wind speed seen by the rotor. It is expected that this will result in unsteady aerodynamic effects: namely, different wake dynamics, a variation of the induction field at the rotor level and enhanced blade-vortex interactions. Further

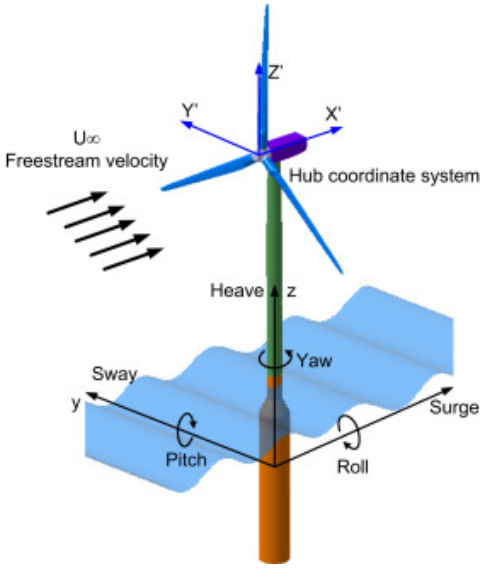

Figure 1.2: Illustration of a horizontal-axis floating wind turbine with its six degrees of freedom. Taken from [59].

understanding of these phenomena is crucial for the design of floating wind turbines, as they affect its loading and performance.

In this project, the induction field of a surging horizontal-axis wind turbine is examined. The choice of focusing on surge motion is made because it is expected to have a strong influence on the aerodynamics of the system, as it modifies the apparent axial velocity at the wind turbine. The effect of the finite number of blades is also examined.

To study these phenomena, two high-fidelity models are used. Next, the results obtained with them are compared to an engineering model, since lower-fidelity models are essential during the design phase of wind turbines due to their reduced computational cost.

1.3. Research questions and report outline

This thesis proposes to answer the following research questions:

1. *What is the impact of platform surge motion on the induction field of a horizontal-axis wind turbine?*
2. *Can a dynamic inflow model accurately predict this induction field?*
3. *What is the effect of the finite number of blades on this induction field?*

An additional objective of this work is the development of an actuator disc and an actuator line model with OpenFOAM, an open-source CFD solver. Besides leading to answers to the research questions enumerated above, these models may serve as a flexible tool for further research on the aerodynamics of floating offshore wind turbines.

This report summarizes the work that has led to answers to the research questions and it is thus structured. First, in chapter 2 a literature review is presented. Next, in chapter 3 the methodology used for the numerical simulations of this project is illustrated. The results obtained from the actuator disc simulations are presented in chapter 4, while the results from the actuator line simulations are discussed in chapter 5. Finally, a conclusion is given in chapter 6.

2

Literature review

In this chapter, a literature review on relevant topics for this project is conducted. First, a general review of the methods used to model the aerodynamics of wind turbines is given in section 2.1. In section 2.2, simplified models for aerodynamic analyses are presented. Next, two phenomena of particular interest for floating wind turbines are described in section 2.3. Finally, an overview of the studies conducted on the aerodynamics of floating horizontal-axis wind turbines is reported in section 2.4.

2.1. Aerodynamic modelling of horizontal axis wind turbines

In this section, the methods used for the aerodynamic analysis of horizontal-axis wind turbines are briefly illustrated. In section 2.1.1 blade element momentum theory is introduced, comprising classical momentum theory and blade-element theory. Next, in section 2.1.2 vorticity-based methods are explained. Finally, Computational Fluid Dynamics (CFD) methods are presented in section 2.1.3.

2.1.1. Blade Element Momentum Theory

Methods based on Blade Element Momentum (BEM) theory are widely used for the aerodynamic analysis of rotors since they present the advantage of a low computational cost. BEM is formed by the union of momentum theory and blade element theory. In this section, it is briefly introduced, taking as reference the work of Burton et al. [4].

Momentum theory was developed by Rankine, W. Fraude and R.E. Fraude for the analysis of propellers and later adapted for wind turbines [66]. In this theory, the wind turbine is approximated by an actuator disc. The basic principle is that the rotor is represented by an infinitely thin and porous disc located in the flow. In its simplest version, the disc is located in steady, incompressible, inviscid axial flow and the load is uniform and normal. Figure 2.1 shows a schematic representation of an actuator disc of this type. The disc causes a step change in flow pressure and a gradual change in flow velocity so that the velocity at the disc U_d is lower than the free-stream velocity U_∞. Therefore, the disc induces a velocity that has to be superimposed to the free-stream velocity. This leads to the definition of the axial induction factor a:

$$a = 1 - \frac{U_d}{U_\infty} \tag{2.1}$$

Using this definition, the induced velocity is $U_{in} = -aU_\infty$ and the velocity at the disc is:

$$U_d = U_\infty(1 - a) \tag{2.2}$$

The air that interacts with the disc forms a streamtube, and it is assumed that there is no mass transfer between the air in it and the surrounding atmosphere. The streamtube expands as the velocity decreases, as prescribed by the continuity equation. After the disc, the flow velocity continues to reduce and the pressure gradually increases until it reaches the atmospheric value again. This area of reduced velocity is called the wake, and once the pressure has reached the atmospheric value it is defined as

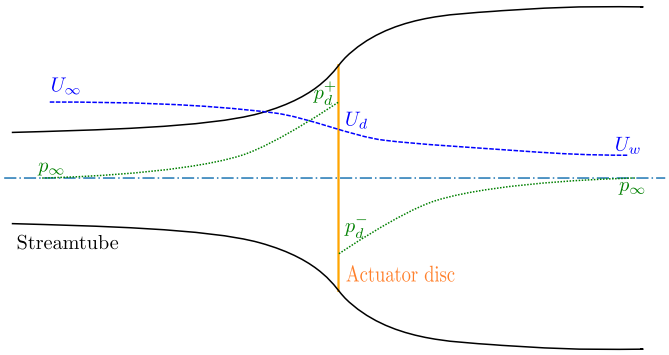

Figure 2.1: Schematic representation of an actuator disc and its streamtube with plots of velocity and pressure. Adapted from [4].

far wake. By applying the energy conservation principle to the flow upstream and downstream the disc, it is found that the velocity in the far wake U_w is:

$$U_w = U_\infty(1 - 2a) \tag{2.3}$$

Overall, the flow is subjected to a change of velocity $U_\infty - U_w$, and consequently to a change of momentum. In this simplified situation, the rate of change of momentum is equal to the thrust force F_t, exerted on the disc in the axial direction. This force is adimensionalized to obtain the thrust coefficient C_T:

$$C_T = \frac{F_T}{\frac{1}{2}\rho A_d U_\infty^2} \tag{2.4}$$

Here, ρ is the air density and A_d is the disc area. From the momentum equation, it is found that the thrust coefficient is linked to the induction factor a by the relation:

$$C_T = 4a(1 - a) \tag{2.5}$$

Hence, momentum theory relates the axial induction and the axial loading on the actuator disc.

This simplified model forms the basis of more complex momentum methods. Glauert introduced a model in which the flow also has a tangential velocity component. The tangential induction factor a' is introduced, and the flow passing the disc is subjected to a change of angular momentum caused by the torque Q. Furthermore, to allow for radial variations of a and a', the disc is divided in annuli. Finally, the rotor loads are coupled to blade loads, resulting in Blade Element Momentum theory (BEM).

Blade element theory assumes that the forces acting at each section of the blades are equal to the forces acting on an identical 2D airfoil. Knowing the relative velocity at the blade element, the angle of attack is calculated, and the lift and drag coefficients are found from look-up tables. The tangential and normal forces acting on the blade are found from the lift and drag. This is illustrated in figure 2.2.

In BEM, it is assumed that the forces at each annulus are solely responsible for the rate of change of momentum of the air passing through that annulus: this means that the annuli are assumed to be independent of one another. Hence, the tangential and axial forces acting on each annulus are equated to the rate of change of momentum of the flow through that annulus. Since both the forces and the rate of change of momentum depend on the induction factors, the equations are solved iteratively.

BEM theory, as formulated so far, needs numerous engineering corrections to be applied to wind turbines in operational conditions. Since it is developed for an actuator disc, which can be considered a rotor with an infinite number of blades, a correction is needed to account for the finite number of blades. Prandtl's tip correction is often used in commercial codes. Furthermore, corrections are needed for predictions in heavily loaded conditions. In fact, for $C_T > 1$ momentum theory predicts an inversion of the flow, which does not occur in practice. What happens instead is that the wake enters the turbulent

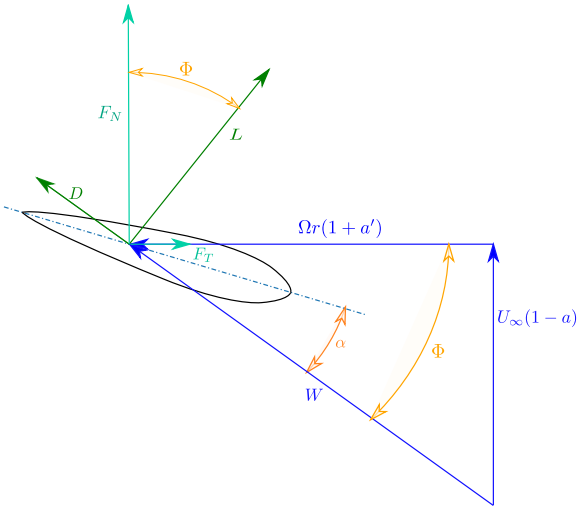

Figure 2.2: Schematic representation of blade element velocities and forces. Adapted from [4].

wake state and mixing between the air in the wake and the surrounding atmosphere takes place. The thrust force predicted by momentum theory has then to be corrected using experimental data. Glauert proposed to fit a parabolic curve in the experimental data [16]. This correction is applied in the Aerodyn code, developed by NREL and used in FAST/OpenFAST for the aeroelastic analysis of wind turbines [37] . However, numerous other fittings to the experimental data have been proposed, and it is still unclear which one describes the experimental results more accurately [42]. As the thrust coefficient further increases, the turbulent wake state leaves place to the vortex ring state, as further explained in section 2.3.2. These states imply a breakdown of momentum theory. Sebastian and Lackner have proposed that the vortex ring state will occur in floating wind turbines as a result of platform motions [45]. This issue is treated in section 2.3.2.

Another fundamental hypothesis of momentum theory is that the flow is steady. Dynamic inflow models are then introduced to account for unsteady effects, as further explained in section 2.3.1. These models become particularly important in floating wind turbines which are subject to additional unsteady effects caused by the floating platform movements.

2.1.2. Vorticity-based methods

Vorticity-based methods, as the name suggests, use vorticity to derive solutions of the flow. Vorticity is a measure of the local rotation of a fluid element and it is defined as the curl of the velocity field. The flow is assumed to be inviscid, incompressible and irrotational. Since potential flow theory can be used, the solution can be found as a superposition of elementary flow solutions. Most vorticity-based methods use the elementary vortex flow: hence, the terms vortex models and vortex methods are also used. These models range from simple analytical models to advanced numerical methods. Consequently, their computational costs and accuracy vary. Low-order vortex methods can be considered as an intermediate approach between BEM engineering models and conventional CFD approaches in terms of accuracy and computational cost [2].

As a lifting surface, circulation is associated to the blade. This circulation is referred to as bound circulation Γ_b. Any change in bound circulation results in vorticity being emitted in the fluid. Usually, this vorticity is divided into trailed vorticity and shed vorticity. The first is emitted as a result of the spatial variations of bound circulation along the span. In an ideal blade with uniformly distributed circulation, there would be two trailed vortices in the wake, namely the root vortex and the tip vortex. In real blades, a bound circulation gradient is found along the entire blade since circulation has to vanish at the blades extremities [2]. Shed vorticity is related to temporal changes of the bound circulation. Together, the two form the model of the wake of the blade. Different representations of the wake vorticity can be found in literature: as vortex filaments, for example in [46], vortex particles as in [31] or vortex rings as in [11]. Figure 2.3 shows a representation of a blade with its bound circulation and wake, where shed and trailed vorticity filaments form a vortex sheet.

To represent the spanwise variations of bound circulation with a finite number of variables, the

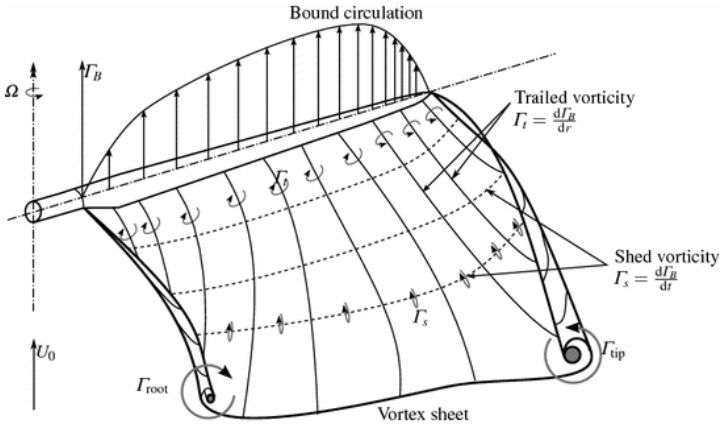

Figure 2.3: Representation of the blade wake as a vortex sheet of trailed and shed vorticity. From [2].

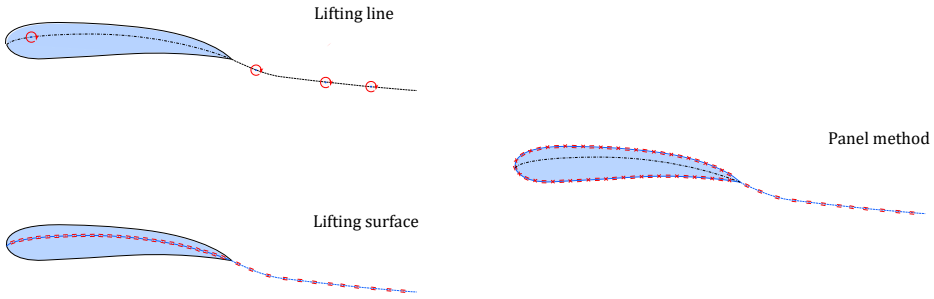

Figure 2.4: Representation of an airfoil with a lifting line, lifting surface and panel method code.

blades are discretized and the bound circulation is represented as distributed vortex strengths [11]. Three different types of vorticity-based methods can be distinguished, on the basis of the representation of the blade: lifting line models, lifting surface models and panel methods. In lifting line models, each blade is simplified as a single spanwise straight line [25] and a single vortex element is placed at each discrete location, while in lifting surface models multiple flow elements (such as vortices, sources or doublets) are located on the mean chord surface. Finally, in panel methods the blade is composed of a series of 3D panels and flow elements are placed around the airfoil geometry. Figure 2.4 illustrates the representation of an airfoil with a lifting line, lifting surface and panel method code.

Another method to classify vorticity-based methods is by distinguishing between prescribed-wake vortex models and free-wake vortex methods. In prescribed-wake vortex models, the position of the vortex elements is prescribed from measurements or semi-empirical rules while in free-wake vortex methods the vortex elements are allowed to convect freely, so that wake deformation occurs [19]. Frozen wake models have a computational cost that is a fraction of the computational cost of free wake models [2]. However, free wake analyses are more suited to the complex flows generated by wind turbines [67]. In particular, they become necessary in unsteady situations [19].

Regardless of the type of vorticity-based method used, the strengths and positions of the bound, trailed and shed vorticity elements are iteratively determined. Knowing these, the velocity can be calculated at each point in the flow domain. Furthermore, the lift per unit span L can be found for each blade element with the Kutta-Joukowsky equation:

$$L = \rho_\infty U_\infty \Gamma_b \tag{2.6}$$

Hence, the loads on the blades are calculated from the bound circulation.

Vorticity-based methods have gained interest in wind energy applications over the last two decades [2]. They have been used in particular to better understand the wake dynamics [19], but also to develop corrections for BEM codes, for example in [3].

2.1.3. Computational Fluid Dynamics methods

Computational Fluid Dynamics (CFD) simulations propose to simulate the behavior of a flow, including its viscous and turbulent effects, numerically. This is achieved by finding an approximate solution to the Navier-Stokes equations that describe the flow.
The Navier-Stokes equations are partial differential equations that express the conservation of momentum, mass and energy of a fluid. For wind turbine simulations, the thermal problem can be neglected and the pressure is assumed to be independent of density. Thus, the problem is described by the incompressible Navier-Stokes equations:

$$\frac{\partial \mathbf{u}}{\partial t} = (\mathbf{u} \cdot \boldsymbol{\nabla})\mathbf{u} - \frac{1}{\rho}\boldsymbol{\nabla}\mathbf{p} + \frac{\boldsymbol{\mathcal{F}}}{\rho} + \nu\boldsymbol{\nabla}^2\mathbf{u} \tag{2.7}$$

If solved, these equations would give the values of fluid velocity $\mathbf{u}$ and pressure p at each point in space, a solution that depends on the external forces $\boldsymbol{\mathcal{F}}$. ν is the kinematic viscosity of the flow. Due to their complexity and non-linearity, however, they can be solved analytically only for very simple cases. Numerical solutions can be found by discretizing the problem. This is achieved with the finite volume approximation: the fluid is divided into non-overlapping control volumes and the conservation laws are applied in their integral form to each volume. The surface integrals are then approximated to obtain a set of algebraic equations that can be solved with an iterative method. This requires appropriate boundary and initial conditions.

A further complication is the presence, in the flow, of turbulent structures. Large structures, or eddies, form and then break up into smaller eddies, until the turbulent energy is dissipated at the smallest scales by viscous effects. There are three main approaches to include turbulent effects in the simulations:

1. DNS (Direct Numerical Simulations): The Navier-Stokes equations are solved without any additional model. The mesh must be fine enough to solve the smallest turbulent structures, and the timestep must capture the fastest oscillations. These simulations are used to obtain fundamental knowledge about turbulence but are too computationally expensive to be used for practical engineering problems

2. LES (Large Eddy Simulations): Only the largest turbulence scales are resolved, while the effect of the smallest scales is modelled

3. RANS (Reynolds-Averaged Navier-Stokes): All turbulence is modelled and a solution for the mean flow is found. An extension of this method has successfully been applied to model slow unsteady effects, for example in [44], [26] and in many studies on floating wind turbines, presented in section 2.4. The term URANS (Unsteady Reynolds-Averaged Navier-Stokes) is often used in literature, although in this work it is chosen to use the term RANS for both steady and unsteady simulations.

RANS models are the least expensive in this list, and represent the current standard in wind turbine simulations [29]. In this approach, the fluid properties are considered to be the sum of a mean and a fluctuating value. Substituting these in the Navier-Stokes equations lead to the Reynolds-averaged Navier-Stokes equations (RANS). This system of equations comprises an additional unknown term, the Reynolds stress. Therefore, there are more unknowns than equations: this is known as the turbulence closure problem. Many different ways of finding an approximate solution to this problem exist, which is the reason why many turbulence models have been developed. For external aerodynamic problems, the $k-\epsilon$ model is widely used. Other popular models are the $k-\omega$ model, which yields better results for boundary layers, and the SST model, which combines the two previous models: the $k-\omega$ model is used near the walls and the $k-\epsilon$ model is used far from them.

From this brief introduction to CFD methods, their complexity is already evident. Setting up a CFD simulation requires the construction of a mesh capable of describing the geometry while meeting some quality requirements that reduce numerical errors. Next, an appropriate turbulence model has to be chosen. Boundary conditions and initial conditions have to be carefully selected. The solution can then be found with a commercial or open-source solver, having selected appropriate convergence schemes and, for unsteady problems, a timestep and a time-marching scheme. It is then necessary to analyze the influence of discretization errors on the solution, as well as the effect of the numerical schemes and turbulence models used.

If the problem has been set up correctly, CFD methods are able to furnish the most accurate representation of the behavior of the flow allowed by a numerical method. Contrary to what happens with vortex methods, viscous effects are also taken into account. Their main drawback, besides the complexity of the setup, is the high computational cost required. For simulations of wind turbines, the complexity and cost are greatly increased by the necessity of having a complex and fine mesh around the blades to solve the boundary layer. The mesh has to rotate with the blades and, for floating wind turbines, it has to move to allow the platform movements. To avoid these problems, simplified models of the rotor can be used. These models are presented in detail in section 2.2.

2.2. Simplified wind turbine models for aerodynamic analysis

In this section, two simplified wind turbine models used in aerodynamic analyses are presented. First, the actuator disc model is treated in section 2.2.1. Next, the actuator line model is presented in section 2.2.2.

2.2.1. Actuator disc model

As explained in section 2.1.1, the approximation of the rotor as an infinitely thin porous disc that perturbs the flow has been used for over a century. It is an important part of momentum theory and blade-element momentum theory. However, the actuator disc concept, in its more general form, is simply a way of inserting discontinuities in the flow field [53], and as such it can be used with other aerodynamic methods. In fact, the first vortex methods were developed for an actuator disc [1]. Furthermore, actuator disc models can be employed in CFD simulations.

In CFD simulations, the actuator disc model is coupled with the full Navier-Stokes equations that describe the motion of the unsteady, 3D flow. In this more general formulation, no additional hypotheses on the flow itself are necessary [53]. Examples of these models can be found in the works by Sørensen et al [53] [52].

When using an actuator disc, the boundary layers on the turbine surfaces are not solved: instead, the forces exerted on the flow are introduced as source terms [19]. This greatly reduces the computational cost of the simulations. The forces can be prescribed and uniformly distributed over the disc, prescribed and radially varying, or they can be calculated from 2D airfoil data, similarly to what happens in BEM models, but without the need for the hypothesis of independence of the annuli. This last type of model is the most complex and has been used by Vaal et al., among others, to analyze the aerodynamics of a floating wind turbine [62].

Actuator disc models are widely used to simulate wakes at the wind-farm level [6] [41] [49]. In rotor aerodynamics, they are a powerful tool to investigate the basic assumptions underlying momentum methods [19]. For example, in the work by Sørensen et al. a uniformly loaded actuator disc is used to study the wake states of a heavily loaded rotor [52]. Actuator disc models are also of particular interest in the study of dynamic inflow phenomena [68].

2.2.2. Actuator line model

The CFD actuator disc model described in section 2.2.1 presents a limitation: at each spanwise location, the forces are distributed evenly in the azimuthal direction [60]. This implies that the method is applicable only for rotationally symmetric flow conditions [60], and that the influence of the tip vortices is not modelled. Sørensen and Shen [54] developed the actuator line (AL) model to overcome these limitations. The main difference with the actuator disc model is that the forces are distributed along three lines that represent the blades and rotate. The forces are usually determined with the use of airfoil data, although they could also be prescribed or calculated assuming constant circulation along the blades.

Sørensen and Shen [54] validated their model against experiments of a 500 kW Nordtank wind turbine and concluded that the computed power distribution was in good agreement with the experiments. Furthermore, they observed that with this method the vortices in the near wake appear as distinct vortex tubes, thus providing a more accurate description of the flow field around the rotor than the actuator disc model does. Many other researchers have done validation studies of actuator line models by comparing them with experimental data, for example Troldborg et al., Shen et al., Porté-Agel et al. [40] and Shen et al. [47].

Troldborg et al. [61] modelled both the near and the far wake of Tjæreborg wind turbine. Good

agreement of the velocity deficit and added turbulence intensity was found two diameters downstream. While Troldborg et al. simulated uniform inflow conditions, Porté-Agel et al. [40] proposed to simulate an atmospherical boundary layer flow. The authors used three models: an actuator disc model without rotation, with uniform thrust force, an actuator disc model with rotation, computing the local drag and lift forces with airfoil data and an actuator line model. The results of the simulations, which used the LES framework to model the turbulence, were compared to wind tunnel measurements and measurements of an operational wind farm. The authors concluded that the actuator disc model with rotation and the actuator line model are capable to capture the velocity deficit in the wake, while the actuator disc model without rotation slightly underestimates this deficit. Shen et al. [47] compared the DTU AL model with the measurements taken during the MEXICO experiments, where a series of experiments were conducted on a model wind turbine rotor. The authors conclude that good agreement with the experimental data exists also for the loading on the rotor, although they highlight the importance of using airfoil data with 3D corrections.

From this brief literature review, it can be deduced that actuator line models can be a useful tool to model the near wake structure and the loading on the blades. The representation of the far wake is also generally in good agreement with experimental data although in that case, an actuator disc model can also provide accurate data with a lower computational cost.

2.3. Phenomena of particular interest for floating wind turbines

In this section, two aerodynamics phenomena of particular interest for floating wind turbines are presented. First, in section 2.3.1 unsteady aerodynamics is briefly treated. Next, section 2.3.2 introduces vortex ring state and propeller state.

2.3.1. Unsteady aerodynamics phenomena

All wind turbines operate in a complex and unsteady environment. The loads on each blade element vary with time because of shear in the ambient wind, ambient turbulence, yawed operating conditions, blade/wake interactions and the effects of wake dynamics, among others [32]. To quantify the unsteadiness of the flow, the reduced frequency k can be introduced:

$$k = \frac{\omega c}{2W} \tag{2.8}$$

Here, ω_c is a characteristic frequency of the flow in rad/s, c is a characteristic length and W is the resultant local flow velocity [32]. Different ranges of k can be associated with steady, quasi-steady, unsteady or highly unsteady flow regions. Strictly speaking, the flow is steady only for $k = 0$, while for $k \leq O(0.01)$ it can be considered quasi-steady [45]. At higher values of k, unsteady aerodynamics effects begin to manifest.

The additional degrees of freedom of a floating wind turbine result in a further increase in the complexity of the aerodynamic environment of the rotor, as described by Sebastian and Lackner [45]. In fact, the platform movements result in rapid local velocity changes, which in turn cause loads oscillations. Enhanced blade-wake interactions can also be expected, since the wind turbine can move directly in its wake. Furthermore, angular motions introduce an effective wind shear and yawed conditions are expected to occur more frequently. All these phenomena increase the unsteadiness of the flow and pose challenges from the modelling point of view. Hence, the investigation of unsteady aerodynamics phenomena is very important in FOWTs.

According to Snel and Schepers [51], unsteady aerodynamics phenomena in rotors can be divided into two groups: unsteady profile aerodynamics and dynamic inflow. The firsts happen at the airfoil level, while dynamic inflow interests the whole rotor.

The basic principle behind unsteady profile aerodynamics can be understood by considering an airfoil undergoing a change in angle of attack. If a quasi-steady assumption is made, it is assumed that the loads adjust instantly to the change in angle of attack. However, the change cannot occur instantly in practice, because time is needed for the flow to adjust around the airfoil in the new position. In wind turbines, the main importance of this phenomenon is in stall [51].

Another time effect is present when the induced velocity at the rotor has to adapt to the loads. In fact, time is needed to accelerate or decelerate the flow after a change in loading. This phenomenon is called 'Dynamic inflow' and it can be better understood by considering that the induction depends on

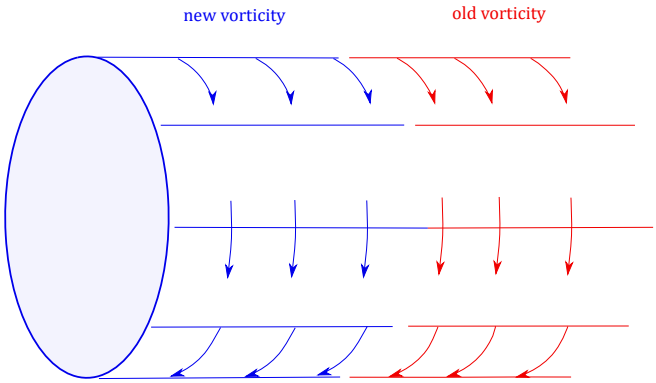

Figure 2.5: Representation of the ”old” and ”new” wake vorticity. Adapted from [43].

the wake vorticity, which convects downstream with the local velocity. When the loading changes, the wake remains a mixture of the ”old” and ”new” vorticity until the ”old” vorticity has convected sufficiently downstream not to influence the velocity at the rotor anymore [43]. This concept is illustrated in figure 2.5. In bottom-founded wind turbines, dynamic inflow can be caused for example by a rapid change of pitch angle, a wind gust or yawed conditions [51]. In floating offshore wind turbines the platform motions are an additional source of unsteadiness.

Free-wake vortex methods and CFD simulations inherently model this phenomenon. This does not happen in BEM models, since a fundamental assumption of momentum theory is that the flow is steady. Hence, this hypothesis has to be relaxed with the introduction of a so-called Dynamic Inflow Model to consider this unsteady effect. This is usually done by adding a time derivative in the momentum theory relation expressed by equation 2.5 [43]. The new equation is:

$$\tau \frac{dU_{in}}{dt} + 4U_{in}(1 - U_{in}) = U_{\infty} C_T \tag{2.9}$$

Here, τ is often referred to as a time constant, although it is not a real constant as it varies, for example, with time and radial position [69]. Different dynamic inflow models have been developed, their main uncertainty is the formulation of τ. The proposed dynamic inflow models include the Pitt-Peters model, the Øye model and the ECN model [69]. In literature, there are not many examples of applications of these models to floating wind turbines and therefore this is an area where further research is needed.

2.3.2. Vortex ring state and propeller state

As described in section 2.1.1, momentum theory is valid for a specific state of the streamtube comprising the actuator disc: namely, windmill state. The different states can be characterized with respect to the induction factor a. For $a < 0$, the thrust force on the rotor is negative (this means that it is in upwind direction) and the rotor injects energy in the flow [42]. This is propeller state. Windmill state corresponds to $0 \leq a \leq 0.5$, while for $0.5 \leq a < 1$ the turbulent wake state is encountered and momentum theory is no longer valid [52]. For $a = 1$ the flow through the actuator disc is blocked and there is toroidal recirculation normal to the disc [10]. This state, called vortex ring state, was first observed in helicopters in descent, thus entering their wake, where it leads to a loss of lift. Finally, for $a > 1$ propeller brake state is entered: the flow across the disc reverts and the wind turbine injects energy in the flow with a thrust directed downwind [42].

Bottom-founded wind turbines are not expected to enter propeller state or vortex ring state. For floating wind turbines, however, the situation is more complex. According to Sebastian and Lackner, a floating wind turbine in axial motion (platform surge or pitch motion) interacts with its wake and can thus enter vortex ring state and propeller state [45]. The mechanism is illustrated in figure 2.7 for a pitching wind turbine. Initially, the turbine is in windmill state. As it pitches back it enters its wake and this is believed to cause the formation of a turbulent region. During this motion, the effective

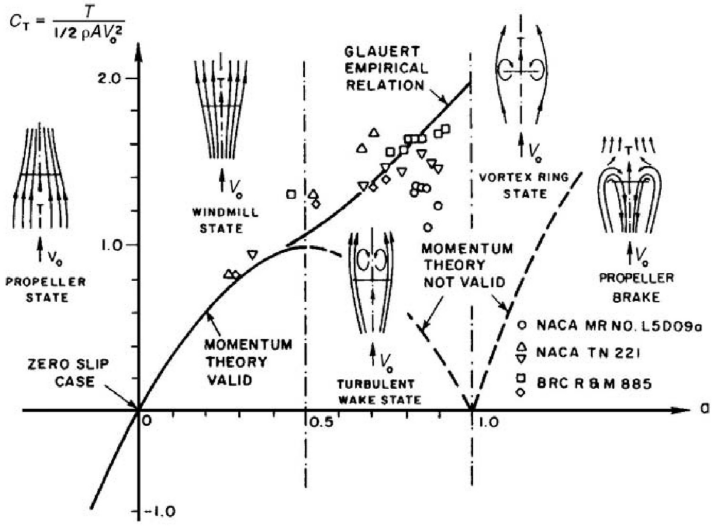

Figure 2.6: Graph of the C_t as a function of the induction factor a with the corresponding wake states. From [12].

wind speed at the rotor may severely drop, and this is expected to cause the formation of the toroidal recirculation typically associated with vortex ring state. Eventually, the wind turbine may start acting like a propeller. The same considerations could apply to a turbine in surge motion. Kyle et al. tested this hypothesis using CFD simulations of NREL 5 MW wind turbine on a semi-submersible barge platform in surge motion. For their simulations, they selected a particular wave state expected to cause a strong surge response in the barge platform. They identified propeller state as the state in which the rotor experiences a negative thrust and observed that when this occurs the tip and root vortices cannot be advected downstream, causing blade-tip vortex interactions and accumulation of vortices at the root [28]. These phenomena are seen as evidence that the vortex ring state also occurs during surge motion.

Vortex ring state and propeller state are a source of concern as they imply a breakdown of momentum theory, which forms the basis of engineering models for the aerodynamic analysis of wind turbines. A frequent occurrence of these two states may compromise the applicability of engineering codes to floating offshore wind turbines. However, there is no general consensus on how to identify these states. Dong and Viré have proposed multiple criteria that could be applied to identify vortex ring state [10]. Furthermore, in [15] the hypothesis that propeller state can be identified from the negative rotor thrust is challenged. The authors claim that it is possible that even as the thrust drops below zero during surge motion, the flow in the streamtube comprising the rotor may not have time to adjust and thus remain in windmill state. In this thesis, this hypothesis is further tested.

2.4. Numerical and experimental studies on floating wind turbines

The complexity of the aerodynamics of FOWTs and the relevance of understanding its peculiarities has motivated several studies in the area. Table 2.1 shows a partial list of scientific papers published on the subject, together with the methodologies used. A review of these studies is presented in this section, to illustrate the state of the art in research on FOWTs aerodynamics.

This section is thus organized: first, a review of the methodologies used is presented in section 2.4.1. Next, the process of choosing the case studies is illustrated in section 2.4.2. Finally, in section 2.4.3, important results obtained by these studies are presented.

2.4.1. Methodologies used

Momentum methods, vorticity-based methods and CFD methods have all been applied to study the aerodynamics of floating offshore wind turbines, as shown in table 2.1. Furthermore, experiments on scaled FOWTs models have been conducted.

Most of the studies simplify the problem by decoupling the platform and the turbine, to reduce the computational cost. However, coupled studies have also been conducted. Sebastian and Lackner

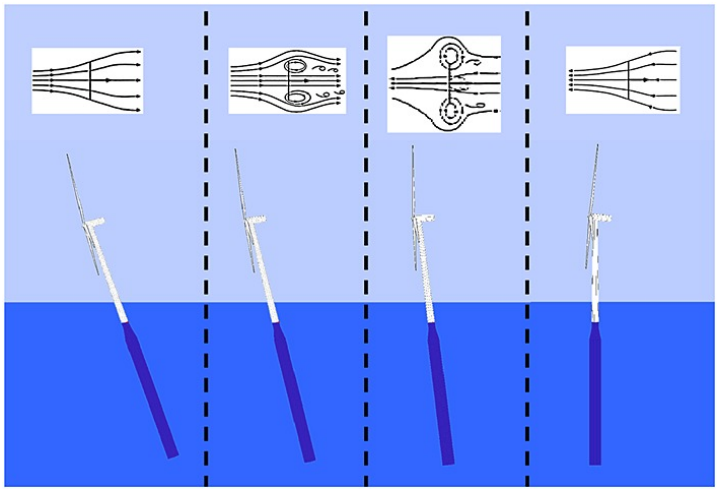

Figure 2.7: Illustration of a pitching wind turbine and the corresponding hypothesized wake states.

[45] pioneered the field by simulating the NREL 5 MW reference wind turbine, together with three different types of floater (barge, spar-buoy, TLP) with NREL FAST code, an aero-hydro-servo-elastic tool for the analysis of wind turbines. The purpose was to identify unsteady aerodynamics effects. The aerodynamic loads are calculated with the AeroDyn subroutine, which alternatively uses a quasi-steady BEM model and a generalized dynamic wake theory, a dynamic inflow model derived from the Pitt-Peters model [22]. This model is applicable only at low tip speed ratios and does not account for wake rotation [37]. Numerous other coupled studies have been conducted with FAST or other analogous tools, such as HAWC2, although most focus on the dynamic response of the wind turbine to the aerodynamic and hydrodynamic loading, for example [23] and [24]. In recent years, some coupled CFD studies have also been conducted, to allow for a more accurate representation of aerodynamic and hydrodynamic phenomena. Examples are the studies conducted by Tran and Kim [58] and Liu et al. [33], in which the NREL 5 MW wind turbine is modelled together with a semisubmersible floating platform and the mooring system. These simulations require advanced methods to capture the free surface between air and waves, handle mesh movements to represent the complex motions of the system and solve the fluid-structure interaction problem, which requires an iterative loop. These studies represent the most accurate representation of a FOWT that can be obtained with numerical methods but are challenging to set up correctly and extremely demanding in terms of computational resources.

A simplified way of studying the aerodynamics of FOWTs is to prescribe a certain platform motion and study its effects. The floater and mooring system are excluded from the simulation. This approach has been adopted by the majority of studies using vortex methods and CFD since it greatly reduces the complexity and computational cost of the simulations.

Examples of uncoupled studies using a vortex methods are [46], [65], [48], and [11]. In particular, Sebastian and Lackner use the Wake Induced Dynamics Simulator (WInDS) code, a free-wake vortex code based on lifting line theory, which they developed [46]. The same code is used by Farrugia et al. [14]. Wen et al. [65] also use a lifting line free-wake vortex method, while Shen et al. [48] adopt a lifting surface method. Finally, the study by Dong et al. [11] uses the lifting line approximation of the wind turbine, together with a modified representation of the wake: the near wake is modelled as vortex filaments, while the far wake is modelled as vortex rings to reduce the computational cost. Most models use free-wake vortex methods since a precise wake model is needed to capture the wake distortion phenomenon that occurs in FOWTs [11].

Numerous studies have been conducted with CFD. Vaal et al. [62] use an actuator disc model where the force is calculated from airfoil data to model a wind turbine in surge motion. The results are compared with those obtained with BEM codes using various dynamic inflow models. The same methodology has been used by Micallef and Sant [36]. Interestingly, not many examples of CFD actuator line models of FOWTs can be found in literature. The majority of the studies use a full CFD, where the actual geometry of the blades is meshed. Examples of such complex CFD studies are the works by Tran and Kim [59] [57] , Kyle et al. [28], Chen et al. [7], Leble and Barakos [30]. In some studies, only

Table 2.1: Reference studies on the aerodynamics of FOWTs considered in this literature review, together with the method they use.

Reference	Method
Sebastian and Lackner [45]	BEM (coupled simulations with FAST)
Sebastian and Lackner [45]	FVW
Vaal et al. [62]	CFD actuator disc, compared to BEM
Kyle et al. [28]	CFD
Mancini et al. [35]	Experiments, compared to various numerical codes
Sivalingam et al. [35]	Experiments, compared to various numerical codes
Micallef and Sant [36]	CFD actuator disc, compared to BEM (FAST)
Tran and Kim [57]	CFD
Chen et al. [7]	CFD
Sivalingam et al. [50]	FVW
Shen et al. [48]	FVW
Lee and Lee [31]	FVW
Farrugia et al. [14]	FVW
Wen et al. [65]	FVW
Dong et al. [11]	FVW
Leble and Barakos [30]	CFD
Tran and Kim [59]	CFD

the rotor is modelled [59] [7], others also model the nacelle [30], some also include the tower [57] [28]. All these simulations make use of complex techniques to model the movements of the moving turbine. Figure 2.8 shows an example of mesh and computational domain for the CFD simulation of a FOWT rotor. In these studies, the need of using airfoil data that may be inaccurate, particularly for stalled conditions, is eliminated. The boundary layers and the wall-created turbulence are also modelled. As a reference of the computational costs, simulations run by Kyle et al. were run in parallel with 576 cores on the Cirrus supercomputer of the Edinburgh Parallel Computing Centre and took between 9 and 12 days to complete [28].

Another way of studying the aerodynamics of FOWTs is by conducting experiments on scaled models in a controlled environment. This methodology presents two main drawbacks, besides the obvious need for an appropriate facility: first, it is not possible to respect all the similarity criteria while scaling a wind turbine. Second, it is difficult to correctly filter the measured data to examine relevant phenomena. Nevertheless, this approach has been used in some studies, whose results provide a valuable benchmark against numerical results. An example is the UNAFLOW project (UNsteady Aerodynamics of FLOating turbines), a collaboration between the Energy research Centre of the Netherlands (ECN), DTU Wind Energy, University of Stuttgart and Politecnico di Milano. As described in the paper by Mancini et al. [35], the experiments were conducted on a 1:75 scaled model of DTU 10 MW Reference wind turbine, with a sinusoidal surge motion imposed to a slider, upon which the wind turbine was mounted. The results were then compared with those obtained with a BEM code, a free-wake vortex code, a CFD actuator line model and a full CFD model. A similar methodology was also adopted by Sivalingam et al. [50].

2.4.2. Choice of case studies

In uncoupled studies, the platform motions are imposed. Thus, the choice of relevant case studies becomes an important part of the research process. First, the choice of the active degrees of freedom for the platform motions has to be made. Next, the mathematical representation of the motion has to be decided. Usually, the motion is represented as a sinusoidal function, so relevant values for the amplitude and frequency have to be chosen.

As mentioned in chapter 1, the platform moves with six degrees of freedom (DoFs): three transitional (surge, sway, heave) and three rotational (pitch, roll and yaw). Surge and pitch involve a motion of the turbine directly in the direction of the free-stream wind speed and of its wake and therefore, intuitively, it is expected that they will have a greater influence on the aerodynamic performance than the other degrees of freedom. Sebastian and Lackner [45] individuated with coupled FAST simulations the DOFs

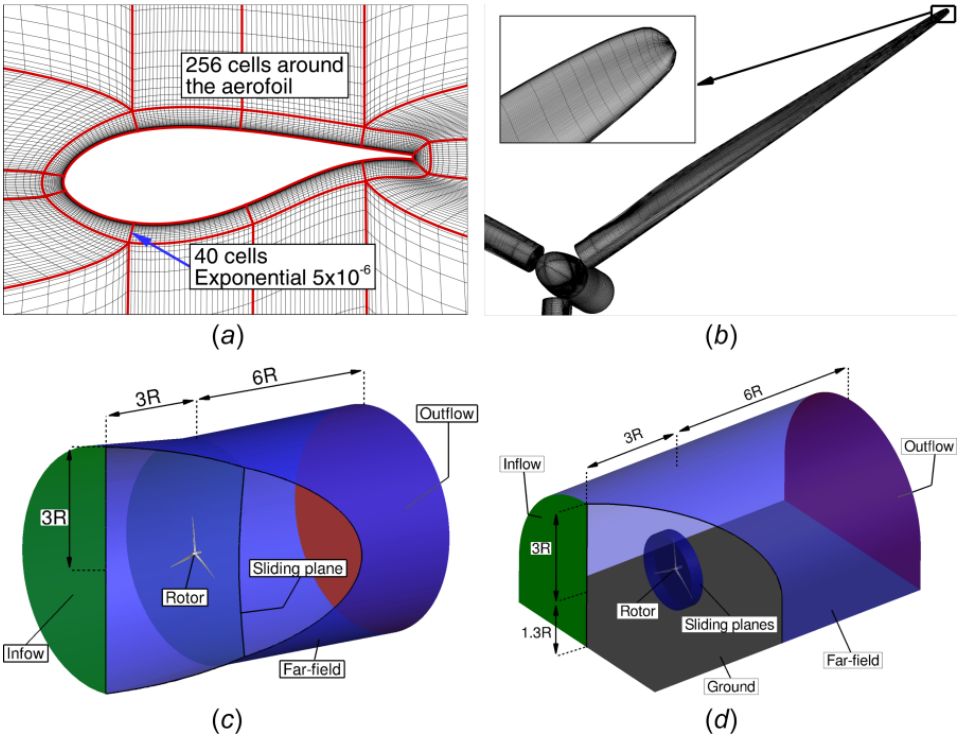

Figure 2.8: Example of mesh and domain for CFD simulations of a FOWT. (a): Mesh at an airfoil section, (b): Detail of the mesh near the blade surface, (c) and (d): computational domains used. From [30].

that may cause unsteady effects: these are pitch for the barge platform, surge and pitch for the TLP, pitch and yaw for the spar-buoy. A later study from the same authors [46], conducted with a free-wake vortex code, highlighted that yaw motion has a low impact on the rotor thrust, while pitch motion has a significant effect on thrust response and wake stability. Tran and Kim also concluded that yaw motion has a minor effect on the thrust and power coefficients [59]. In simulations conducted by Dong et al. [11], no significant oscillations of thrust and power coefficients occur when modes other than pitch and surge are investigated. The authors note that heave and sway motions change the relative tangential wind velocity at the airfoils, but the effect is small since the tangential speed that originates from the blade rotation is much bigger than the variation caused by platform motions. Pitch and surge motions, therefore, are the most relevant degrees of freedom while studying the aerodynamics of FOWTs, and in fact most studies focus on one, or both, of these modes [7] [14] [65] [35] [50] [58].

The chosen DoFs have then to be included in the simulations. To do so, each mode is usually represented as a sinusoidal signal, having an amplitude A, a frequency ω and a phase Φ. A is expressed in meters for transitional motions and in degrees for rotational motion, while ω is in $rads^{-1}$. Equation 2.10 describes the motion displacement as a function of time t, while equation 2.11 describes the motion velocity.

$$x = A \cdot sin(2\omega t + \Phi) \tag{2.10}$$

$$V = \frac{dx}{dt} = \omega \cdot A \cdot cos(\omega t + \Phi) \tag{2.11}$$

The phase Φ is usually put equal to 0 and kept constant. Figure 2.9 shows the sinusoidal displacement and velocity as a function of t/T, where T is the motion period. This representation of the platform movements is an approximation of the motion signals obtained with coupled simulations, which can be considered a summation of sinusoids with different amplitudes and frequencies. Among studies that perform uncoupled simulations, only Sebastian and Lackner represent the motions as a summation of sinusoids. The authors first perform a series of FAST simulations to obtain platform responses to various wind and wave conditions. Next, sinusoids of the form given in equation 2.12 are fitted to the platform motion responses:

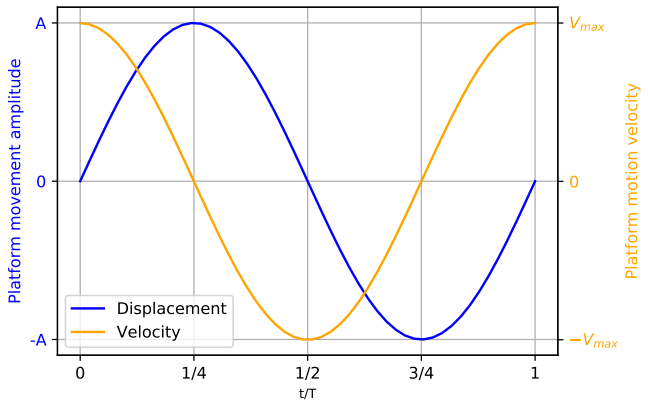

Figure 2.9: Representation of FOWT sinusoidal displacement and velocity.

$$x = x_0 + A_1 \cdot sin(\omega_1 t + \Phi_1) + A_2 \cdot sin(\omega_2 t + \Phi_2) \tag{2.12}$$

This formula is justified by the observation, made by the authors in an earlier study [45], that the majority of the signal energy is in two frequencies, corresponding to the sea state and the rotation frequency of the wind turbine.

Performing coupled simulations with lower-fidelity methods and then using the results as inputs for higher fidelity simulations is one of the possible methods to choose significant and reasonably realistic case studies [45] [36]. Numerous authors do not perform these simulations directly, but cite other studies to justify their choices. Vaal et al. [62] refer to a study by Wayman [64] to select their case studies. The same amplitudes and frequencies are simulated also in [57], [50], [48], while Lee and Lee [31] and Kyle et al. [28] refer to another study by Wayman et al. [63] to select their case studies.

So far, three characteristics of the case studies selected have been mentioned: motion amplitude, motion frequency and free-stream wind speed. However, the tip speed ratio is also important. Therefore, some studies examine the influence it has on the aerodynamic performance of a FOWT. In particular, Micallef and Sant consider a turbine in surge motion with fixed amplitude, frequency and free-stream wind speed at three different tip speed ratios. Other authors examine the FOWTs in rated, below-rated and above-rated conditions, and in doing so examine different tip speed ratios [46] [50] [14].

Many combinations of motion frequency and amplitude can be found in literature. Most of the studies employ a NREL 5 MW reference wind turbine, but there are also studies that employ scaled models, and therefore also scaled frequencies and amplitudes. To compare amplitudes and frequencies chosen at different conditions, the reduced frequency ω_{red} and reduced amplitude A_{red} are introduced:

$$\omega_{red} = \frac{\omega D}{U_\infty} \tag{2.13}$$

$$A_{red} = \frac{A}{D} \tag{2.14}$$

These quantities can be combined to form $V_{max,red}$, the maximum motion velocity relative to free-stream wind speed:

$$V_{max,red} = \frac{A \cdot \omega}{U_\infty} = A_{red} \cdot \omega_{red} \tag{2.15}$$

The graph in figure 2.10 shows the reduced amplitudes and frequencies of the case studies found in literature for surge motion. V_{max} isolines are also shown. It can be seen that the vast majority of studies consider cases with $V_{max} < 0.25$. The maximum value of V_{max} is slightly above 1. This data has also been presented in [15].

2.4.3. Main results presented in literature

The platform motions cause relative motion of the rotor in relation to the wind. As mentioned in section 2.4.2, axial motions (i.e surge and pitch) have a more significant effect on the aerodynamics of the wind

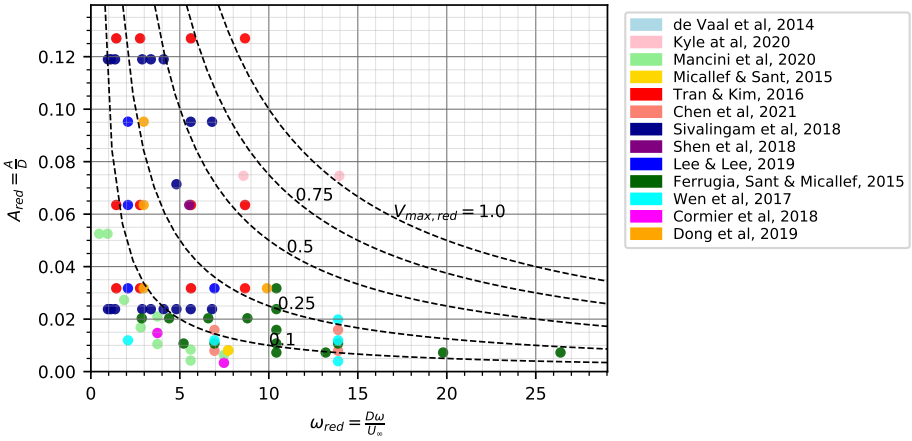

Figure 2.10: Reduced surge amplitudes and reduced surge frequencies of case studies found in literature, with $V_{max,red}$ isolines.

turbine, since they modify the axial velocity at the rotor disc. For simplicity, the following discussion refers to a rotor in surge motion.

For a rotor in surge motion, the axial velocity at the rotor V_a becomes [62]:

$$V_a = U_\infty - V_s - U_{in} \tag{2.16}$$

Here, V_s is the surge velocity and U_{in} is the induced velocity. As the surge velocity oscillates, the velocity at the rotor also oscillates, and so do the loads. To understand this, we can look at figure 2.9, which shows the sinusoids representing the motion displacement and velocity, and consider a quasi-steady case. Between $0T$ and $1/4T$ the rotor is surging downwind, V_s is positive and applying equation 2.16 we see that the velocity seen by the rotor is lower than the free-stream wind speed. Between $1/4T$ and $3/4T$, the rotor is surging upwind and the velocity seen by the rotor is higher than the free-stream wind speed. These oscillations of the velocity at the rotor cause oscillations of the bound circulation. It is therefore expected that the thrust and power of the floating wind turbine will oscillate with the same frequency of the surge motion. Furthermore, it is expected that the amplitude of the thrust and power coefficient oscillations will be related to the amplitudes of the surge velocity variations, which means they will be related to V_{max}. These oscillations are critical because they increase the fatigue load of the wind turbine and diminish the quality of the power produced. Figure 2.11 shows an example of thrust oscillations during surge motion, from the work of Cormier et al. [9]. In quasi-steady situations, the loading has a phase difference of -90°with the platform motion [9]. At high motion frequencies, it is expected that dynamic inflow phenomena will occur and manifest as a small additional phase shift [9].

Most of the studies on the aerodynamics of floating wind turbines study separately the effect that motion frequencies and amplitudes have on the load response. Tran and Kim [57] and Lee and Lee [31] observe that the amplitude of the response increases as the frequency of surge motion increases. An explanation of this is that V_{max} is proportional to the motion frequency. The work of Mancini et al. [35] compares the amplitude of thrust coefficient variations predicted with different low-fidelity models, high-fidelity models and experiments with the ones predicted by quasi-steady theory. The authors conclude that all the codes closely agree with quasi-steady theory. However, the case selected all have $V_{max,red} < 0.1$, as shown in figure 2.10, and only rated conditions are considered. Vaal et al. [62] observe that, as the frequency of surge oscillations increases, BEM codes with different dynamic inflow models and a CFD actuator disc model yield different predictions of the induction. However, they also note that this has a limited effect on the integrated rotor load, so the thrust is well predicted by all the codes. Micallef and Sant use a similar methodology, but choose three case studies with $V_{max,red} = 0.062$ and three tip speed ratios: below-rated, rated and above-rated. In this situation, the wake-induced velocity is the most significant contribution that leads to loads oscillations. The results obtained with the CFD actuator disc model show that the peak-to-peak load variations increase as the tip speed ratio increases. Furthermore, at rated and above-rated tip speed ratios load predictions do not agree with those obtained with the two BEM models implemented in FAST. The effect of the tip-speed ratio is thus explained: a higher tip speed ratio results in a streamtube of higher vortex strength. This

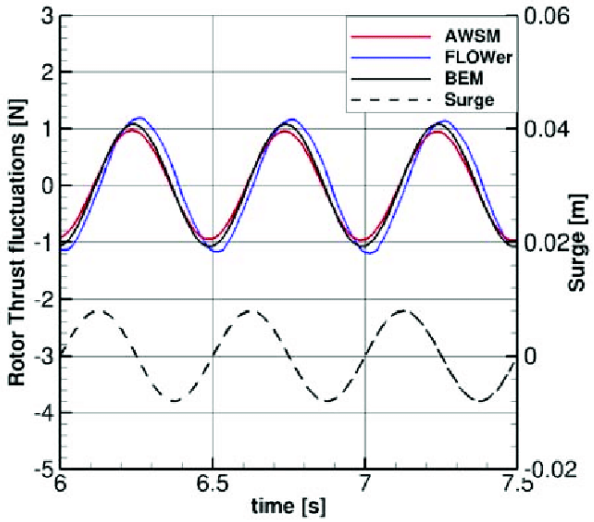

Figure 2.11: Example of thrust oscillations and displacement of a turbine in surge motion. Taken from [9].

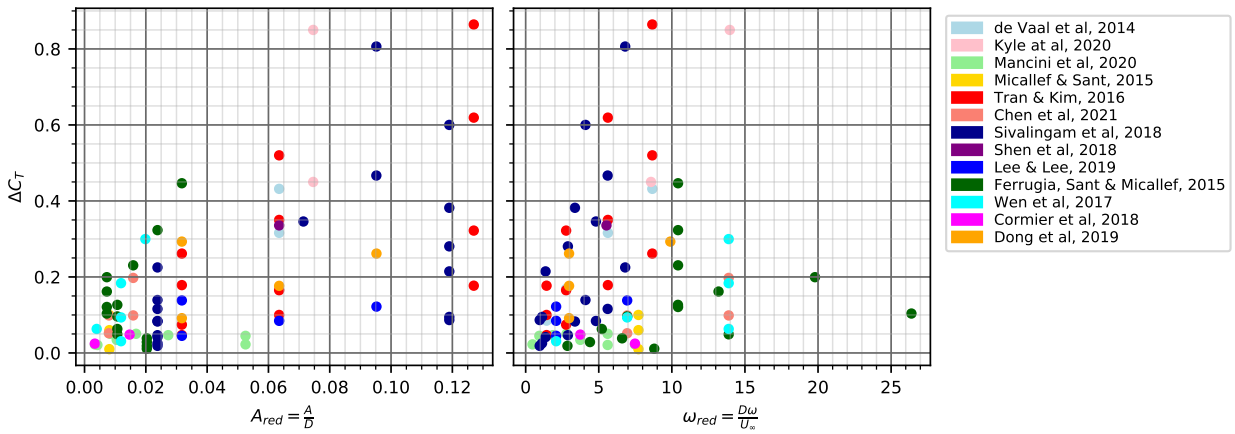

Figure 2.12: Amplitude of thrust coefficient response to surge motion, as a function of the reduced amplitude (left plot) and reduced frequency (right plot).

increases the amplitude of oscillation of the induced velocities in all directions. However, in BEM radial flows are not considered, and therefore the peak-to-peak variations are underestimated. This study shows that in some cases the wake unsteady aerodynamic effects influence the overall performance of the rotor.

Many other studies examine the thrust coefficient oscillations. To give a clear picture of the state-of-the-art, figure 2.12 shows the amplitude of these oscillations ΔC_T as a function of reduced amplitude and reduced frequencies of the surge motion.

The reduced amplitudes considered range from 0.00336 to 0.127, while the reduced frequencies range from 0.467 to 26.4, with only two cases exceeding $k = 15$. Figure 2.13 shows the amplitude of thrust coefficient variations as a function of $V_{max,red}$. It is interesting to see that all studies are in accordance in predicting a linear increase of ΔC_t with $V_{max,red}$. The data of the study by Farrugia et al. [14] and Sivalingam et al. [50] looks more disperse, but this is because in these studies three different tip speed ratios are examined. Figure 2.14 shows ΔC_t as a function of the simulation mean thrust coefficient. It can be seen that in three cases the amplitude of the thrust coefficient oscillations exceeds the mean thrust coefficient value, indicating that during the cycle the thrust coefficient reaches negative values.

So far, only the results concerning the amplitude of load variations have been considered. However,

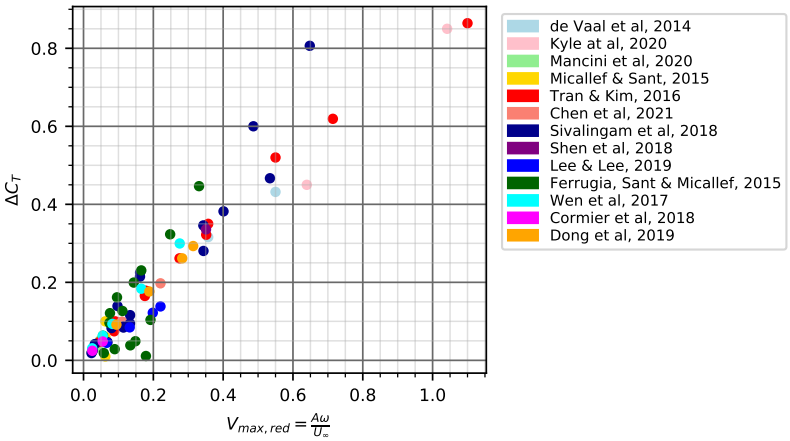

Figure 2.13: Amplitude of thrust coefficient response to surge motion as a function of reduced maximum motion velocity.

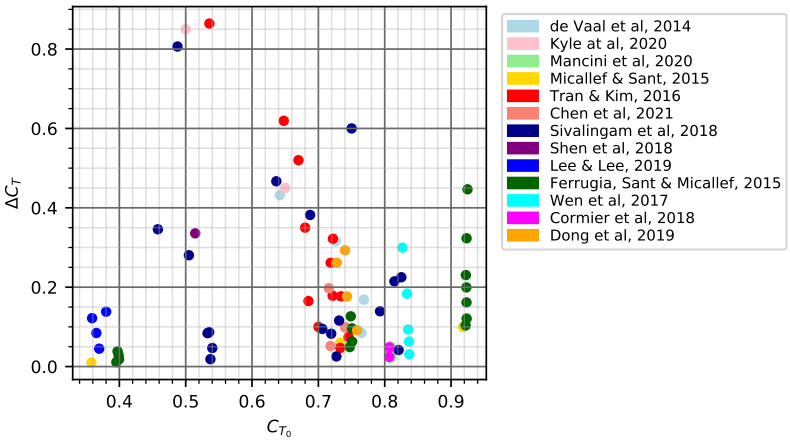

Figure 2.14: Amplitude of thrust coefficient response to surge motion as a function of mean thrust coefficient.

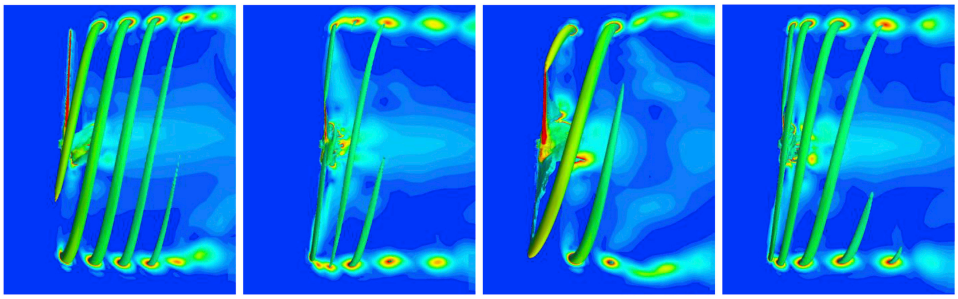

(a) Rotor blade model alone (T_0 = 0T, 1/8T, 4/8T, and 8/8T))

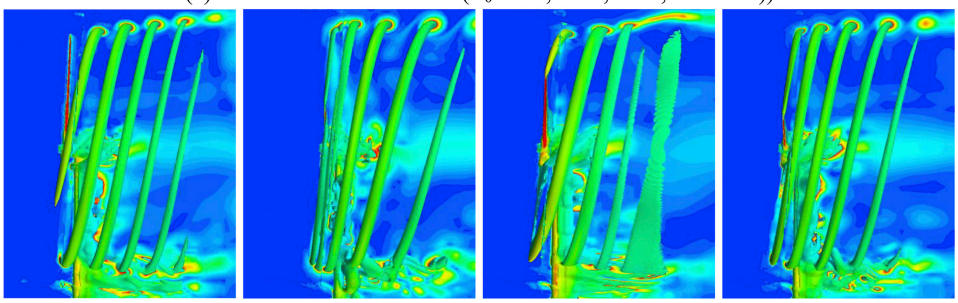

(b) Full wind turbine model (T_0 = 0T, 1/8T, 4/8T, and 8/8T))

Figure 2.15: Example of iso-vorticity contours of a FOWT in surge motion, obtained with CFD simulations of the rotor alone (a) and of the full turbine including the tower (b). From [57].

the mean thrust and power also vary under pitch and surge motions. Shen et al. [48] have found an increase of the average power output of 3.31% and a decrease in average rotor thrust of 5.21% at rated wind speed and tip speed ratio and $V_{max,red} = 0.351$. In certain conditions, therefore, there is a gain in power produced due to the platform motion. Wen et al. [65] explain this by saying that due to the platform motions there is more power in the system.

The platform motions are expected to also influence the wake dynamics. In fact, they cause an oscillation in time of the bound circulation of the blades, resulting in a pattern of accelerated and decelerated vortices with different strengths visible downstream. This aspect is evident in [57], [46] and [9], among others. Figure 2.15 shows the iso-vorticity contours obtained by Tran and Kim [57] for a turbine in surge motion. The variation of distances between neighboring vortex tubes is clearly visible. Moreover, the authors highlight the presence of complex interactions between the tower wake and the tip vortices, visible from the comparison between simulations of the rotor alone and of the full turbine. Lee and Lee [31] observe that the interaction between vortices with different strengths makes the wake highly unstable, so the helicoidal shape of the wake breaks down earlier than for a bottom-founded turbine. Furthermore they show that, although pitch and surge result in the most unstable deformation of the wake, the other platform motions result in a deformed wake structure as well.

3

Methodology

In this chapter, the numerical models used during the project are described. Section 3.1 is about the actuator disc model, while section 3.2 is about the actuator line model. The setup and validation processes of both CFD models are reported. Additionally, the dynamic inflow model is briefly presented in section 3.3.

3.1. CFD Actuator disc model

For the first part of this work, the floating wind turbine was approximated with a CFD actuator disc model. The model was built in OpenFOAM, a free and open-source CFD software. OpenFOAM consists of C++ libraries, used to create applications to set up, solve and post-process a vast range of continuum mechanics problems with the finite volumes method. The creation of the mesh, setting up of boundary conditions and definition of the simulation settings are done through the inputs inserted by the user in the form of text dictionaries. Additionally, it is possible to modify the source code to develop new applications for specific uses.

In this section, the procedure used to build and validate this model is described. First, in section 3.1.1 the modifications made to the OpenFOAM code are explained. The simulations setup is then described in section 3.1.2, while the validation process is reported in section 3.1.3.

3.1.1. Modifications to the OpenFOAM code

CFD actuator disc models have been introduced in section 2.2.1. In CFD simulations, source terms are introduced in the Navier-Stokes equations in correspondence of the cells of the actuator disc. In OpenFOAM, the user can manipulate the equations via finite volume options, in short *fvOptions*. In particular, the class *actuationDiskSource* allows the introduction of source terms in the momentum equation. Four inputs are necessary: a fixed set of cells corresponding to the actuator disc, the thrust coefficient of the disc, and a set of monitor cells. The sets of cells can be created with another dictionary (*topoSetDict*), while the other inputs are specified in the *fvOptions* dictionary. The thrust force F_T is calculated with the formula:

$$F_T = \frac{1}{2}\rho A_d |\mathbf{u_d} \cdot \mathbf{n}|^2 C_T^* \tag{3.1}$$

with

$$C_T^* = C_T \left(\frac{|\mathbf{u_m}|}{|\mathbf{u_d}|} \right)^2 \tag{3.2}$$

Here, A_d is the disc area, ρ is the reference density of the air, $\mathbf{u_m}$ is the spatial average of the velocity in the cells of the monitored region and $\mathbf{u_d}$ is the spatial average of the velocity in the actuator disc cells. Four main modifications are made to the *ActuationDiskSource* class for this research:

1. When taking the velocity from a set of monitoring cells, there is the risk of considering a region where the velocity is already disturbed by the actuator disc. Instead, a fixed value of the undisturbed velocity U_∞ is given as an input. This velocity corresponds to the velocity at the inlet.

2. The thrust force is calculated as:

$$F_T = \frac{1}{2}\rho A_d U_\infty^2 C_T \tag{3.3}$$

Thus, C_T^* is eliminated and C_T is directly used to calculate the thrust.

3. For the actuator disc in surge motion, it is necessary to select different cells at different time steps. The surge motion is assumed to be sinusoidal, with the position of the actuator disc along the free-stream direction x calculated as:

$$x = x_0 + Asin(2\pi ft) \tag{3.4}$$

where x_0 is the initial position of the disc, A is the amplitude of the surge motion, f is the frequency of the motion in s^{-1}. Thus, x_0, A, f and the diameter of the disc are given as inputs and at each time step, x is calculated and a new set of cells is selected accordingly.

4. For the unsteady cases, the thrust coefficient also oscillates in time. The oscillations are prescribed according to the formula:

$$C_T = C_{T0} - \Delta C_T cos(2\pi ft + \Phi) \tag{3.5}$$

where C_{T0} is the baseline thrust coefficient, ΔC_T is the amplitude of the thrust oscillations, f is the frequency of the thrust oscillations and Φ is an additional phase difference between the surge motion and the thrust oscillations. When Φ is equal to zero, the thrust has a -90°shift with the surge motion. Instead of C_T, the inputs of the model are C_{T_0}, ΔC_T and Φ and f, which is generally equal to the motion frequency.

With these modifications, a new class of OpenFOAM objects called *movingActuatorDisc* is created. The source code of this class is given in appendix C. First, this class is used to simulate a steady actuator disc and validate the model against momentum theory. This is done by setting the motion amplitude A, the frequency ω, the amplitude of the thrust oscillations ΔC_T and the phase difference Φ equal to zero.

3.1.2. Simulations set-up

Setting up the CFD simulations requires the creation of a domain with a mesh, the imposition of appropriate boundary conditions and the choice of a turbulence model.

In the beginning, a 2D slice of the actuator disc was modelled, but during the validation phase it was clear that a 3D model would guarantee better results. Nevertheless, the hypothesis of axisymmetric flow is still applied to reduce the computational cost. Consequently, only one quarter of the domain is built to represent the full 3D domain with suitable symmetry boundary conditions. One quarter of an actuator disc of diameter D is located in the domain. Figure 3.1 shows a schematic representation of the computational domain, which is a parallelepiped. The dimensions of the domain are referred to as X_{up}, X_{down}, Y_{inlet} and Z_{inlet}.
The boundary conditions imposed are:

- Velocity boundary conditions at the inlet
- Pressure boundary conditions at the outlet
- Symmetry boundary conditions on side 1 and at the bottom
- Slip-wall boundary conditions on side 2 and at the top of the domain

The simulations are run with RANS $k-\epsilon$ turbulence model, widely used for external aerodynamics simulations. The values of k, ϵ and ν_t at the inlet have to be chosen. They depend on a chosen level of turbulence intensity. It is expected that this value will only have a marginal effect on the induction, while it will affect the development of the wake. Following the recommendations presented in [55], an ambient turbulence intensity of 0.1% is selected and the corresponding parameters are calculated with the formulas given in [38].

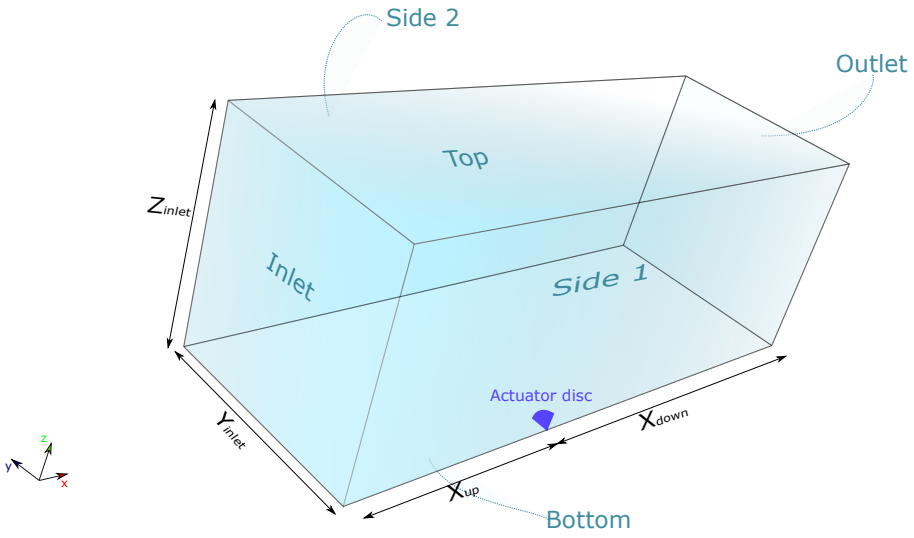

Figure 3.1: Schematic representation of the simulation domain.

3.1.3. Validation process

To validate the model, numerous simulations are carried out to verify the influence of mesh refinement, domain size, ambient turbulence intensity and Reynolds number on the induction at the disc.

The induction is calculated with equation 2.1 for each cell i that composes the axis of the disc. Then, the average induction is calculated as:

$$a_{avg} = \frac{\sum_{i=1}^{i=N} a_i \cdot \pi(r_{i+1}^2 - r_i^2)}{\pi D^2/4} \tag{3.6}$$

The axial velocity U_x cannot be directly extracted at the disc as the solution presents a discontinuity in the proximity of the disc. In that area, however, the solution is very linear so the velocity at the disc is found with an interpolation. Figure 3.2 shows an example of the velocity in the proximity of the actuator disc and of the interpolated velocity.

The result is compared with the result predicted with axial momentum theory a_{th}, where the thrust coefficient and the axial induction coefficient are related through equation 2.5. The relative percentage error is calculated as:

$$error = \frac{a_{th} - a_{avg}}{a_{th}} \cdot 100 \tag{3.7}$$

A reference domain is created, with the following parameters:

- $X_{up} = 6D$
- $X_{down} = 10D$
- $Y_{inlet} = 6D$
- $Z_{inlet} = 6D$

The domain is divided into three zones:

1. A background zone having squared mesh cells with sides of length $l_{background} = 0.14D$.
2. A first refinement zone in the area that extends 1D upstream, 2D downstream and 1D in y and z direction.
3. A second refinement zone that extends $0.25D$ upstream and downstream and 0.6D in y and z direction. The length of this refined zone in x direction is indicated as X_{ref} and the length of the mesh cells sides is l_{ref}.

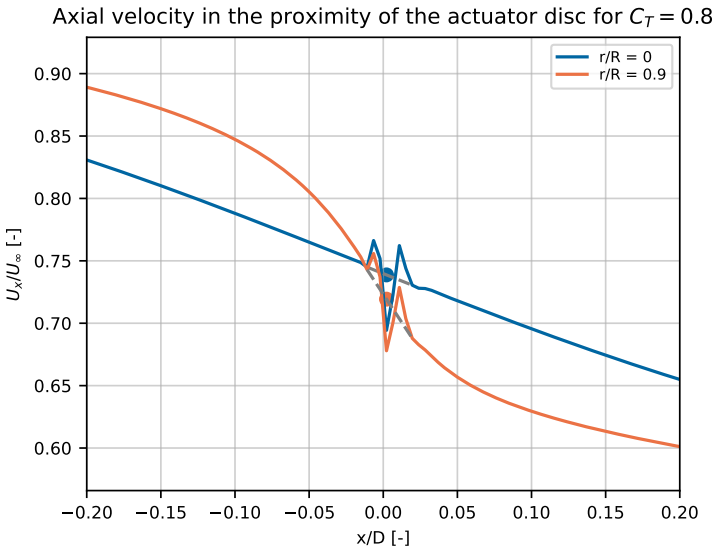

Figure 3.2: Axial velocity and interpolated velocity at $r/R = 0$ and $r/R = 0.9$.

Table 3.1: Cases used for the mesh independence study of the actuator disc model.

Case	$l_{ref}/D[-]$	Refinement level in zone 3	a_{avg} for $C_T = 0.8$	Relative error in a_{avg}
1	0.0700000	1	0.234	15.3%
2	0.0350000	2	0.248	10.2%
3	0.0175000	3	0.260	6.07%
4	0.0087500	4	0.268	3.15%
5	0.0043750	5	0.272	1.66%
6	0.0021875	6	0.274	0.757%

In the refined zones, the OpenFOAM utility *snappyHexMesh* is used to refine the mesh: each cell is split into a number of cells that depends on the specified refinement level. The refinement level in zone 2 is set to 1, hence the length of the cell sides is $0.07D$. For the mesh independence study, five different refinement levels in zone 3 are considered. For each, the induction is calculated at $C_T = 0.8$. The cases are summarized in table 3.1 and the results are presented in figure 3.3. From these results, it is evident that the solution converges towards the theoretical induction value when the refinement level is increased. A refinement level of 5 is chosen, with $l_{ref} = 0.04375$, as it provides an acceptable accuracy at a much lower computational cost than the refinement level of 6.

The chosen mesh was used to test the independence of the solution with respect to the domain size. From the reference domain, simulations were conducted with different values of X_{up}, X_{down}, Z_{inlet} and Y_{inlet}. The cases are summarized in table 3.2 and the results are shown in figure 3.4. In every case, the results converge as the domain size is increased, as expected. These results show that it is not possible to reduce the domain size without influencing the induction. An increase in X_{down} would lead to a decrease of the induction. However, this decrease is in the order of $e-6$ and can be neglected. When the value of Y_{inlet} or Z_{inlet} is doubled, the induction increases by 0.25%. The value of X_{up} has a stronger influence, as the induction increases by 0.36% when X_{up} is increased to $9.2D$. Overall, the only modification made to the reference domain after this analysis was the increase of X_{up} to $9.2D$, in an effort to compromise between the accuracy of the solution and the computational cost required.

Along with the simulations with different domain sizes, different values of the turbulence intensity and of the Reynolds numbers are tested. The results are shown in figure 3.5. As expected, the chosen value of turbulence intensity does not have a significant effect on the induction. The influence of the Reynolds number is also limited, particularly for Reynolds numbers higher than 10^6. For this reason, the simulations are carried out at a Reynolds number of $5e+6$.

It is important to obtain a solution that does not depend on the size of the refinement zone, and in

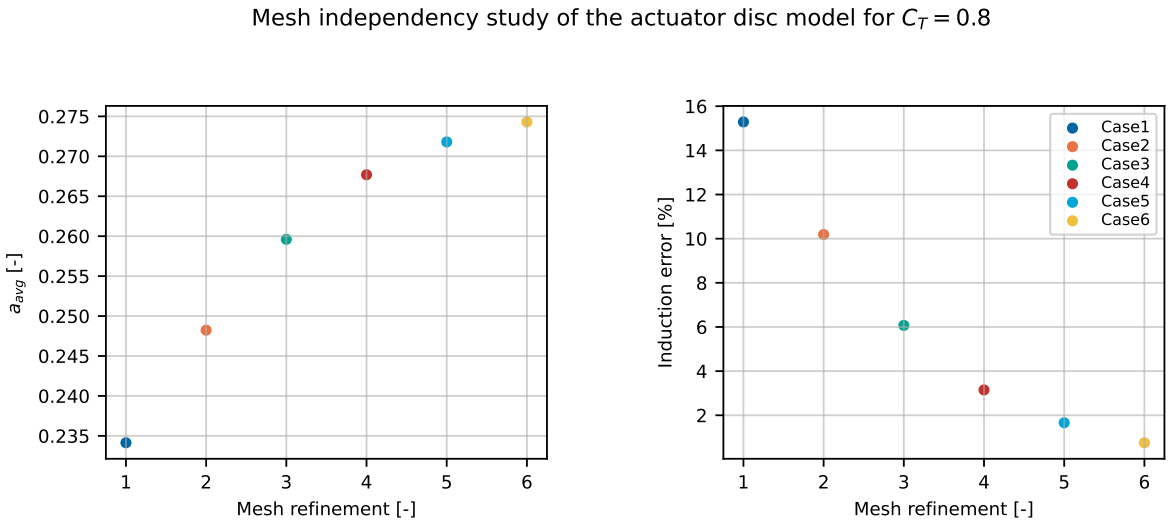

Figure 3.3: Disc average induction and percentage relative induction error for various mesh refinement levels in zone 3 of the actuator disc model.

Table 3.2: Cases used for the size domain independence study of the actuator disc model.

Case	X_{up}/D [-]	X_{down}/D [-]	Y_{inlet}/D [-]	Z_{inlet}/D [-]	a_{avg} for $C_T = 0.8$	Relative error in a_{avg}
7	2.8	10	6	6	0.2628	4.93%
8	9.2	10	6	6	0.2728	1.30%
9	12.4	10	6	6	0.2730	1.23%
10	6	6.8	6	6	0.2718	1.65%
11	6	13.2	6	6	0.2718	1.66%
12	6	16.4	6	6	0.2718	1.66%
13	6	10	3	6	0.2689	2.73%
14	6	10	12	6	0.2725	1.41%
15	6	10	24	6	0.2726	1.37%
16	6	10	6	3	0.2682	2.95%
17	6	10	6	12	0.2725	1.41%
18	6	10	6	24	0.2726	1.37%

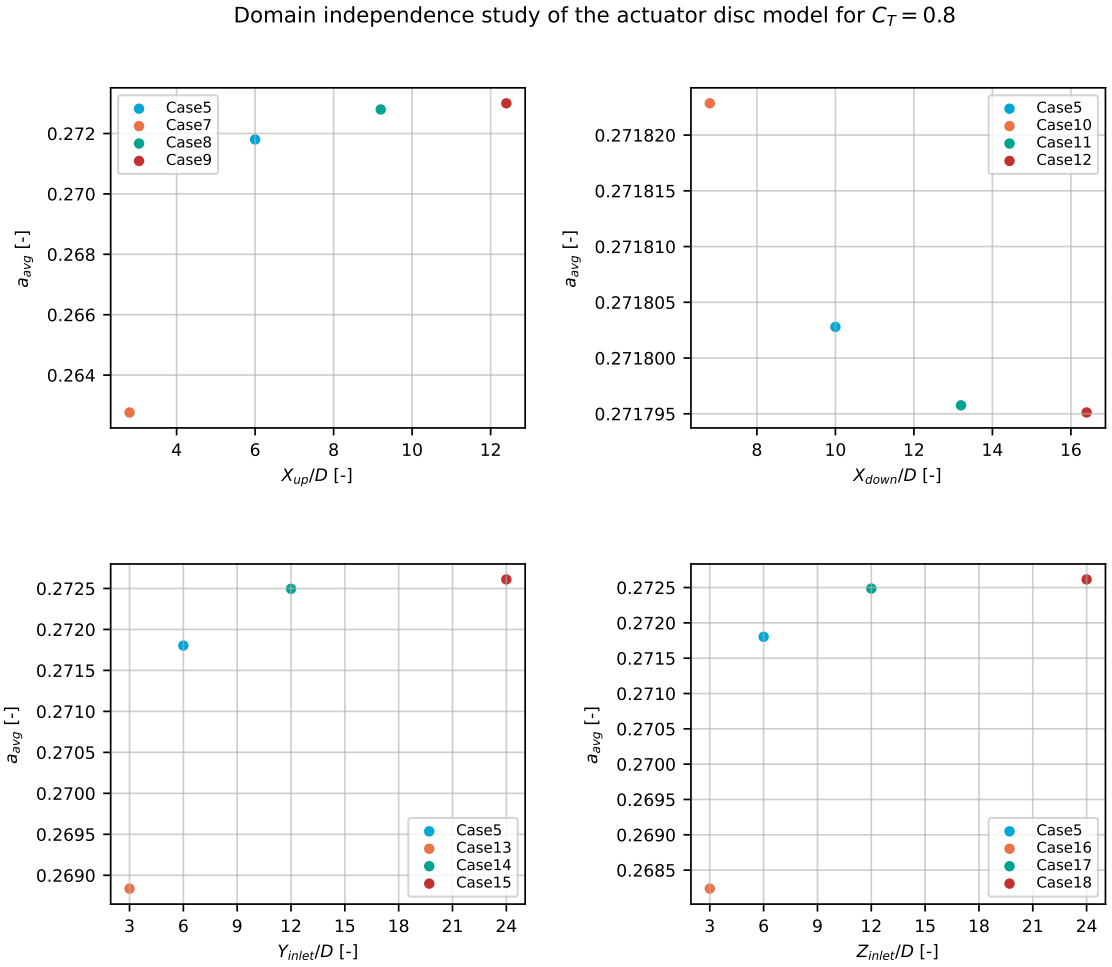

Figure 3.4: Percentage relative error in the average induction obtained with the actuator disc model as a function of X_{up}, X_{down}, Y_{inlet}, Z_{inlet}.

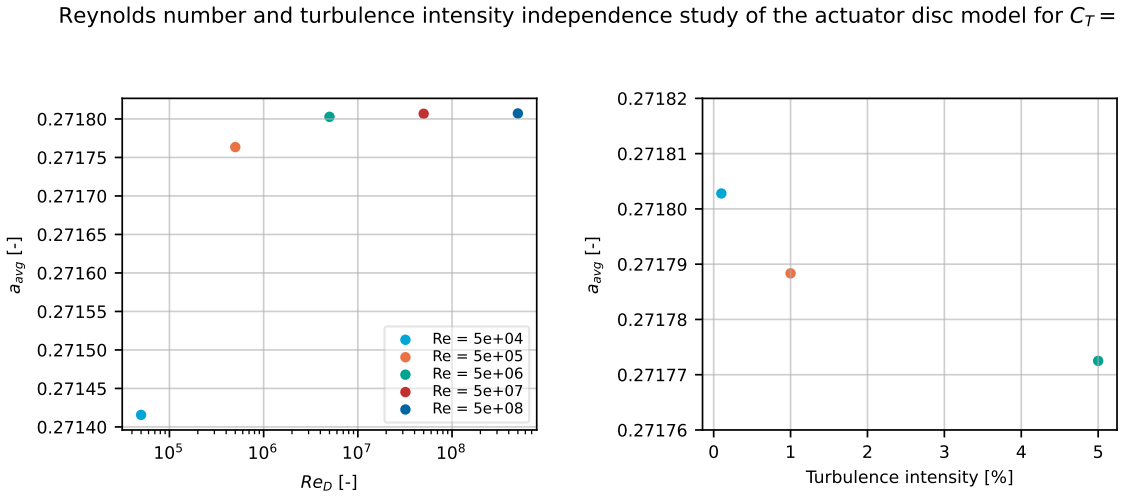

Figure 3.5: Average induction at the actuator disc for various values of Reynolds number and turbulence intensity.

Table 3.3: Cases used for the study of the dependence of the solution to the size of the refinement zone of the actuator disc model.

Case	X_{ref}	a_{avg} for $C_T = 0.8$
19	0.5	0.2713
20	1	0.2712
21	1.5	0.2709

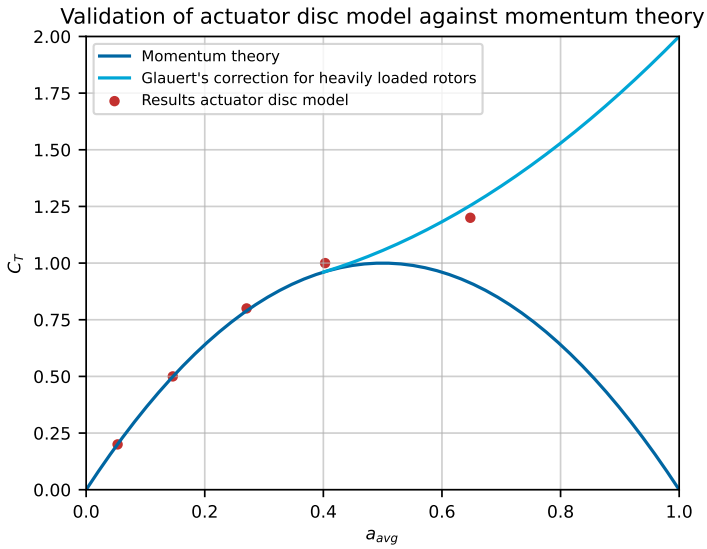

Figure 3.6: Induction factor obtained with the actuator disc model for various thrust coefficients, compared to the theoretical induction factor.

particular the zone with refinement level 5 that surrounds the actuator disc. This is critical to ensure the validity of the simulations with the surging actuator, as the movement effectively changes the dimensions of the refinement zone upstream and downstream of the disc. Three simulations are set up, with different values of X_{ref}. The cases and results are summarized in table 3.3. On the basis of these results, $X_{ref} = 0.25D$ is considered insufficient and in the final mesh it is increased to $1.2D$.

The final mesh has a refinement level of 5, $Y_{inlet} = Z_{inlet} = 6D$, $X_{up} = 9.2D$, $X_{down} = 10D$ and $X_{ref} = 1.2D$. To increase the quality of the mesh, refinement zones with refinement levels 2, 3 and 4 are added. This ensures a smooth transition between the zone with a refinement level of 1 and the zone with a refinement level of 5.

The final mesh was used to finalize the validation phase: the induction was calculated for various values of C_T and compared to the theoretical values predicted with momentum theory for $C_T < 1$ and with Glauert's experimental correction for $C_T > 1$. The results are shown in figure 3.6. They are in great agreement with theory and Glauert's correction. The agreement is excellent at low thrust coefficients and worsens when the thrust coefficient increases, particularly at $C_T = 1.2$. However, it is still good, considering the challenging high load and the fact that Glauert's correction is only one of the possible fits to sparse experimental data [42].

After the analysis of the disc average induction, the radial distribution of the induction was analyzed. The results for $C_T = 0.8$ are shown in figure 3.7. The trend is qualitatively similar to the one presented in numerous studies on non-linear actuator discs, for example in [52], [34] and [27]. The induction at the centre of the disc is lower than the disc average and it reaches the average value at around $0.8R$. A similar trend is observed for all values of C_T.

Since the average induction is in good agreement with momentum theory and the induction radial distribution presents the expected trend, this model is considered validated and suitable for the simulations of the surging actuator disc.

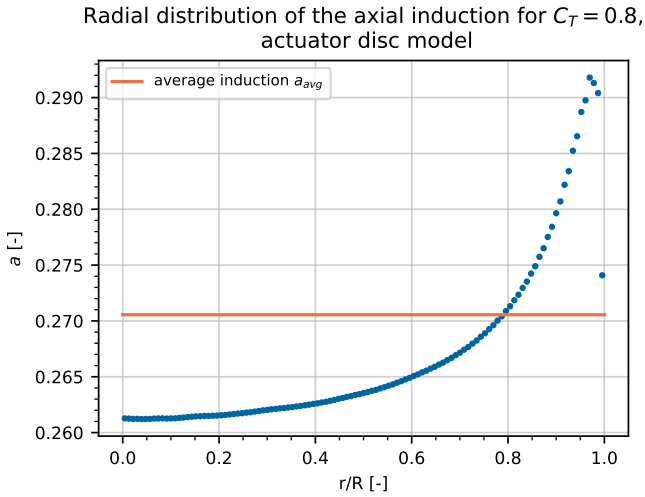

Figure 3.7: Radial distribution of the axial induction for $C_t = 0.8$. Each dot represents a cell over the disc axis.

3.2. Actuator line model

For the second part of this work, a CFD actuator line model was implemented. In this model, a certain total thrust can be imposed and only axial forces are exerted on the flow. This means that the only difference with the actuator disc model is the finite number of blades, of which the effect can be studied. The model was built by modifying *turbinesFoam* [**turbinesFoam**], an extension library for OpenFOAM.

In this section, the setup and validation process of this model are described. First, in section 3.2.1 the modifications made to *turbinesFoam* are reported. The simulations setup is described in section 3.2.2. Finally, section 3.2.3 is about the validation process of the model.

3.2.1. Modifications to the *turbinesFoam* code

TurbinesFoam uses finite volume options to introduce source terms in the Navier-Stokes equations, similarly to the *actuationDiskSource* class but implementing an actuator line model. In its original version, the lift and drag forces are calculated with airfoil data. For this work, this part was modified to obtain an actuator line model with prescribed thrust. Each blade forms an actuator line composed of multiple elements. For each element of the actuator line, with outer radius r_2 and inner radius r_1, in a rotor with a number N_B of blades, the elementary axial force is calculated as:

$$f_T(r') = \frac{C_T}{N_B}\frac{1}{2}\rho U_\infty^2 2\pi r'(r_2 - r_1) \tag{3.8}$$

with:

$$r' = \frac{r_2 + r_1}{2} \tag{3.9}$$

This results in a load that increases linearly along the blades.

Other modifications were made to allow the surge motion of the turbine. The position and thrust coefficient oscillate according to formulas 3.4 and 3.5, respectively.

3.2.2. Simulations set-up

The represented rotor has three blades, the hub and the tower are not modelled.

The computational domain is a parallelepiped. Contrary to the actuator disc model, in this case the hypothesis of axisymmetric flow was not applied and the full rotor was modelled instead of modelling only one quarter of it. The domain of the actuator line simulations was created from the domain of the actuator disc simulations, mirrored around the xy and xz planes. The imposed boundary conditions are velocity boundary conditions at the inlet, pressure boundary conditions at the outlet and slip-wall boundary conditions on the other sides of the domain. The turbulence model, turbulence intensity and Reynolds numbers were maintained equal to those of the actuator disc simulations.

Around the rotor there are multiple zones of refinement, created using *snappyHexMesh*. Those include an area of length X_{ref} around the disc with the maximum refinement level, surrounded by areas of decreasing refinement levels that allow a gradual transition to the baseline mesh. The number of elements of each of the actuator lines that represent the blades is taken as equal to the number of mesh cells that compose it.

3.2.3. Validation process

The dependence of the induction to the refinement level of the cells around the disc, size of the cells in the background mesh ($l_{background}$) and length of the inner zone of refinement (X_{ref}) was analyzed.

The induction was thus calculated: first, a representative value for each annulus in which the rotor is divided by the actuator line elements is found. These azimuthally-averaged induction factors are then used in equation 3.6 to obtain the rotor average induction factor.

All the simulations used a tip speed ratio of 7. The initial mesh had the following characteristics:

- $Refinement\ level = 4.$
- $l_{background} = 0.14D.$
- $X_{ref} = 0.28D$

In figure 3.9, the plots of the induction factor for different values of refinement level, $l_{background}$ and X_{ref} and a thrust coefficient of 0.8 are shown. The refinement level is found to have a strong effect on the results, as the induction factor increases when the cell size in the refined area diminishes. However, the cell size of the initial mesh was maintained as increasing the refinement level resulted in an unsustainable computational cost. As for the value of $l_{background}$, it was maintained since larger cells resulted in a lower induction factor, while diminishing their size did not have a noticeable effect on the result. Lastly, the analysis showed that the length X_{ref} was insufficient, and it was thus quadrupled. This was the only change made between the initial and the final mesh.

In figure 3.8 the radial distribution of the azimuthally-average induction factor is shown. It can be seen that it is lower than the average until around $0.4R$, then it goes slightly above the average, peaking at around $0.9R$, then steeply diminishes. This distribution is different from that of the actuator disc, shown in figure 3.7, reflecting the fact that the load is uniformly distributed for the actuator disc while it grows linearly with the radius for the actuator line.

In figure 3.10, the induction factors obtained for various values of C_T with the final mesh are shown and compared with momentum theory with Glauert's correction. With respect to the results obtained with the actuator disc model, the induction is generally lower and the difference with the theoretical value is greater, especially at high thrust coefficients. However, the agreement is still fairly good, especially considering that momentum theory was formulated for an actuator disc and that the finite number of blades influences the results.

3.3. Dynamic inflow model

The results of the CFD simulations are compared with results from a dynamic inflow model. The model was developed by Carlos Ferreira specifically for floating wind turbines. A complete description of the code and of the results obtained with it for a surging disc are presented in [15]. In this model two reference values of induction are defined: the streamtube induction velocity u_{str} and the induction velocity at the actuator u_{act}.

A hypothesis of this model is that the momentum analysis of the actuator disc in surge motion has to be carried out in an inertial reference frame. Consequently, the reference velocity is defined as:

$$U_{\infty_{ref}} = U_{\infty} \tag{3.10}$$

Next, a streamtube wake-convection reference velocity at the actuator U_{str} is defined and used to calculate a quasi-steady solution of the induction velocity u_{qs}, through equation 3.11:

$$u_{qs} = \frac{C_T U_{\infty}^2}{4} \frac{1}{U_{str}} \tag{3.11}$$

When the streamtube is heavily loaded, Glauert correction is applied to determine u_{qs}. The following step in the algorithm is the calculations of two time scales τ_{act_1} and τ_{act_2}, one for the convection of

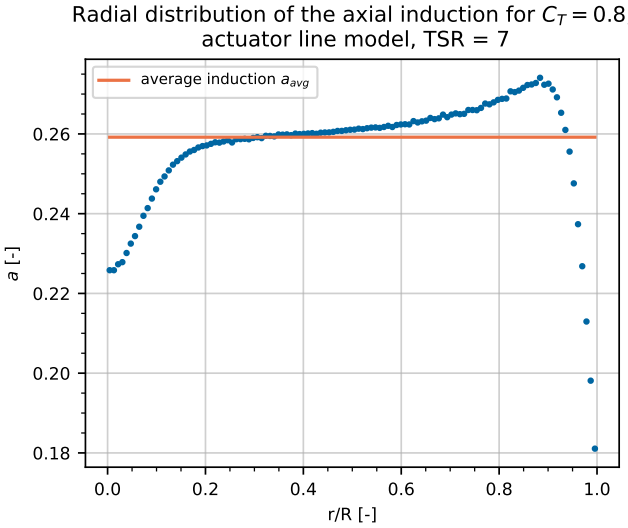

Figure 3.8: Radial distribution of the azimuthally-averaged axial induction for $C_T = 0.8$. Each dot represents an annulus in which the rotor has been divided.

the old vorticity and one for the convection of the new vorticity. Finally, the new values of streamtube induction velocity u_{str} and of the induction velocity at the actuator are calculated using a low pass filter:

$$u_{act_{(t+\Delta t)}} = u_{act_{(t)}} e^{-\frac{\Delta t}{\tau_{act_1}}} + u_{qs}\left(1 - e^{-\frac{\Delta t}{\tau_{act_2}}}\right) \tag{3.12}$$

$$u_{str(t+\Delta t)} = u_{str_{(t)}} e^{-\frac{\Delta t}{\tau_{str}}} + u_{qs}\left(1 - e^{-\frac{\Delta t}{\tau_{str}}}\right) \tag{3.13}$$

The induction at the actuator can then be represented in dimensionless form through the induction factor a, calculated as:

$$a = \frac{u_{act}}{U_\infty} \tag{3.14}$$

This dynamic inflow model was used in [15] to derive the induction field of a surging disc in different conditions of reduced frequency and reduced amplitude of the motion. The results agreed well with those obtained with a semi-free wake vortex ring model.

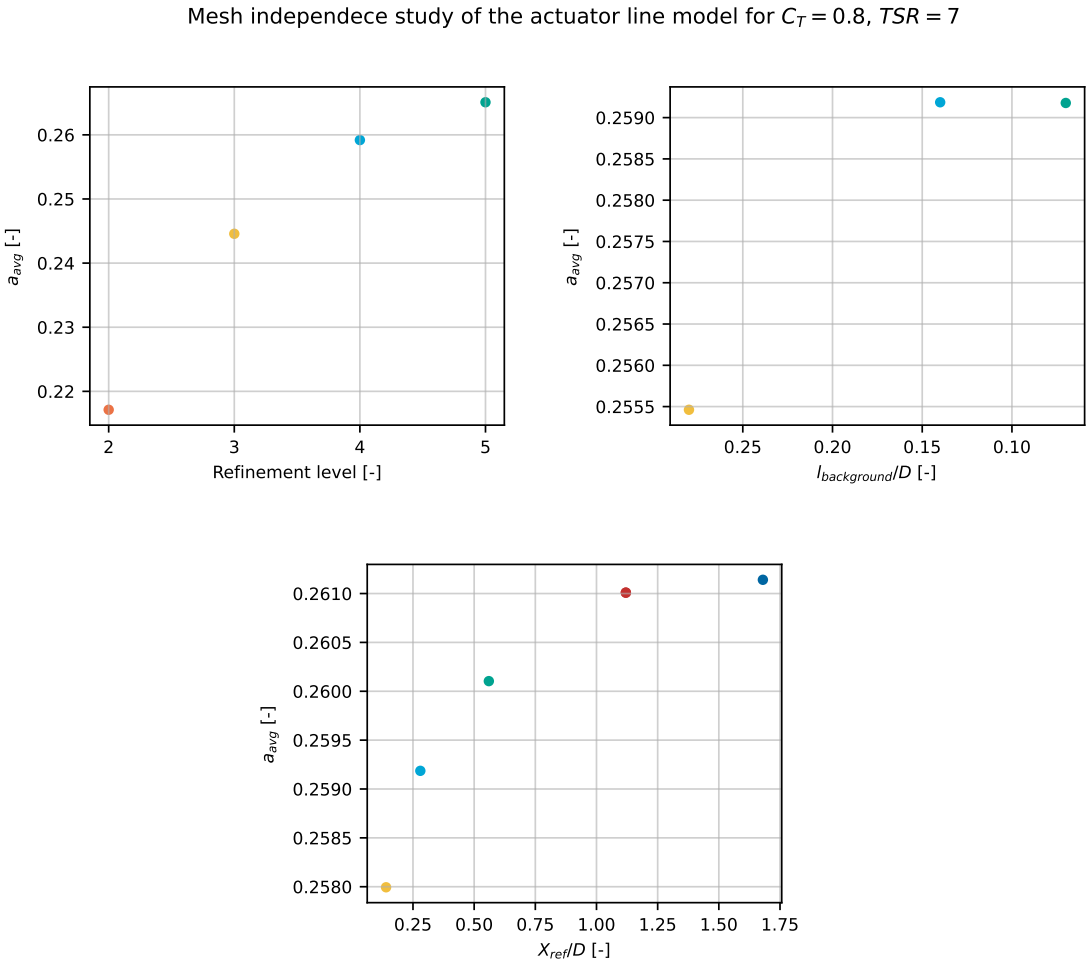

Figure 3.9: Disc average induction factor for various values of refinement level, $l_{background}$ and x_{ref}.

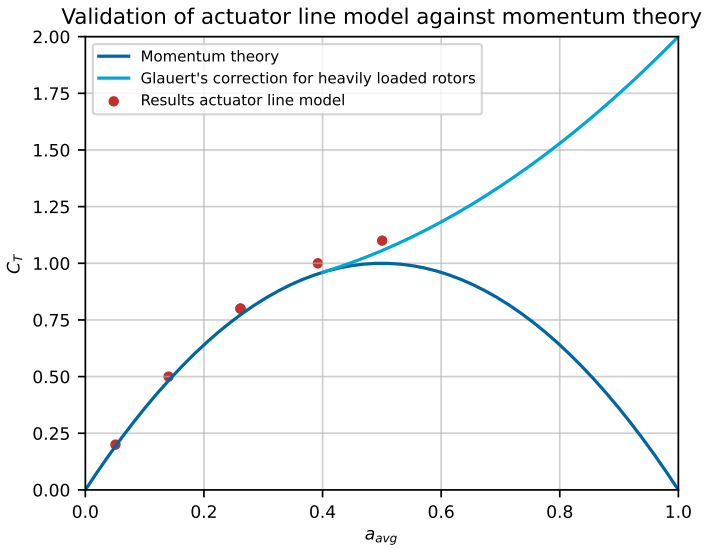

Figure 3.10: Induction factor obtained with the actuator line model for various thrust coefficients, compared to the theoretical induction factor.

4

Results of the actuator disc simulations

In this chapter, the results obtained with the actuator disc model described in section 3.1 are commented. First, in section 4.1 the case studies selected for this project are introduced. Next, in section 4.2 the contours of the velocity, vorticity and pressure fields are shown and used to characterize the streamtube wake states. The induction field of the unsteady simulations is analyzed in section 4.3 and a comparison with the results acquired with the dynamic inflow model introduced in section 3.3 is made. Finally, in section 4.4 the contours of the velocity, vorticity and pressure fields of some unsteady cases are presented.

4.1. Case studies

The CFD actuator disc model described in section 3.1 was used first to carry out steady simulations and then unsteady simulations with varying thrust and surge motion of the disc. The steady simulations are characterized by different thrust coefficients.

The unsteady actuator disc simulations were carried out starting from these steady state solutions. The case studies are characterized by either a varying value of the thrust coefficient, a varying position of the actuator disc or both. The oscillations of the thrust coefficient are prescribed according to the formula:

$$C_T = C_{T0} - \Delta C_T cos\left(\frac{\omega_{red} U_\infty}{D} t\right) \tag{4.1}$$

The surge motion is prescribed with the formula:

$$x = x_0 + A_{red} D sin\left(\frac{\omega_{red} U_\infty}{D} t\right) \tag{4.2}$$

with the initial position of the disc x_0 set to 0. It was verified that by the time of the last simulated period convergence had been reached, meaning that the period-average value of the induction factor, its phase and amplitude did not vary significantly from one period to another. The oscillations of the induction factor were then analyzed.

The first eighteen simulations run were used to assess the influence of the changes in position of the disc and thrust coefficient oscillations on the induction. To do so, cases with the still actuator disc and a varying thrust were simulated, followed by cases with the moving actuator disc and a constant thrust and finally by cases with both the surge motion and the varying thrust. Next, cases with a negative ΔC_T were selected, despite being unlikely to occur in real wind turbines, as this allowed to study the behavior of the dynamic inflow model in extreme situations. Finally, simulations with $\Delta C_T > C_{T0}$ were run, to analyze whether propeller state, turbulent wake state or vortex ring state are entered in these situations. Each combination of ΔC_T and C_{T0} was used for cases with reduced frequencies of 1, 5 and 10 corrsponding to maximum velocities of motion of 0.1, 0.5 and 1, respectively, to represent the whole range encountered during the literature review and shown in figures 2.10 and 2.13. The values of C_{T0}, ΔC_T, A_{red}, ω_{red} and $V_{max,red}$ of all simulations are summarized in table 4.1. Among these cases, case 24 reproduces a case of Kyle et al. [28].

Table 4.1: C_{T0}, ΔCT, A_{red} , ω_{red} and $V_{max,red}$ of the unsteady actuator disc simulations.

Case Number	C_{t0}	ΔC_t	A_{red}	ω_{red}	$V_{max,red}$
0	0.8	0.5	0	1	0.1
1	0.8	0.5	0	5	0.5
2	0.8	0.5	0	10	1
3	0.5	0.3	0	1	0.1
4	0.5	0.3	0	5	0.5
5	0.5	0.3	0	10	1
6	0.8	0	0.1	1	0.1
7	0.8	0	0.1	5	0.5
8	0.8	0	0.1	10	1
9	0.5	0	0.1	1	0.1
10	0.5	0	0.1	5	0.5
11	0.5	0	0.1	10	1
12	0.8	0.5	0.1	1	0.1
13	0.8	0.5	0.1	5	0.5
14	0.8	0.5	0.1	10	1
15	0.5	0.3	0.1	1	0.1
16	0.5	0.3	0.1	5	0.5
17	0.5	0.3	0.1	10	1
18	0.8	-0.5	0.1	1	0.1
19	0.8	-0.5	0.1	5	0.5
20	0.8	-0.5	0.1	10	1
21	0.5	1	0.1	1	0.1
22	0.5	1	0.1	5	0.5
23	0.5	1	0.1	10	1
24	0.5	0.85	0.074603	14	1.04442

4.2. Velocity, vorticity and pressure fields of steady cases

Besides being used to validate the actuator disc model with respect to momentum theory, the steady simulations were used to investigate the ability of the model to simulate the wake states in which momentum theory breaks down. In particular, both simulations at high values and negative values of C_T were carried out. The axial velocity, radial velocity, vorticity and pressure fields are analyzed respectively in section 4.2.1, 4.2.2, 4.2.3 and 4.2.4. From the results, it is concluded that the model correctly captures the characteristics of the flow field at windmill state, turbulent wake state and propeller state.

4.2.1. Axial velocity field

Figure 4.1 shows the contour plots of the axial velocity around the actuator disc for $C_T = 0.8$, $C_T = 1$, $C_T = 1.1$ and $C_T = 1.2$. As expected, downstream of the disc a wake where the velocity is lower than the free-stream wind speed is formed. After the disc, the flow keeps slowing down as the wake expands. The velocity reaches a minimum and then the wake recovery starts, driven by turbulent mixing. As the C_T increases, the expansion of the wake is more pronounced and the velocity in the wake reaches lower values. At the same time, the wake recovery process is faster, due to the increased turbulent mixing. In all cases, the wake has not fully recovered yet $10D$ downstream of the disc. In the contour plots for $C_T = 1.1$ and $C_T = 1.2$, an area with negative induced velocity is visible. That area is the recirculation zone which characterizes the turbulent wake state. With respect to the case with $C_T = 1.2$, for $C_T = 1.1$ the recirculation zone is smaller and located farther downstream, while it is absent for $C_T = 1$ and $C_T = 0.8$, for which the streamtube is in windmill state.

The ability of the model to simulate situations with negative thrust coefficients was also tested. The contour plots of the axial velocity field for $C_T = -2$ and $C_T = -4$ are presented in figure 4.2. Here, the streamtube is in propeller state. After the disc, the flow accelerates and the streamtube contracts. The velocity reaches higher values for $C_T = -4$.

4.2.2. Radial velocity field

Figure 4.3 shows the contour plots of the radial component of the velocity for the cases with positive thrust. Around the disc, the radial velocity is positive, with the highest values around the disc edge. At higher thrust coefficients, the expansion of the wake is more pronounced and thus the radial velocity reaches higher values. Furthermore, at thrust coefficients higher than 1 an area with negative radial velocity is visible some diameters after the disc: this reflects the curve of the streamlines around the area with the inverted flow. When the streamtube is in propeller state the radial velocity around the disc is negative, as the wake contracts downstream of the disc. This is shown in figure 4.4. Also in this case, the magnitude of the radial velocity is at its maximum at the edge of the disc.

4.2.3. Vorticity field

The contour plots of the vorticity in y direction for the cases with positive thrust, shown in figure 4.5, highlight other characteristics of these load cases. The vorticity is generated at the edge of the disc, where there is a change in the force field. The generated vorticity is positive and its strength increases with increasing C_T. This vorticity is then convected downstream with the local flow velocity. It is also subjected to viscous diffusion and mixing, so it expands and its strength decreases with the downstream distance. It should be noted that in an actuator disc model the vorticity diffuses faster than it would in the case of a rotor with a finite number of blades. In that case, distinct vortex cores would form and the distance among them would depend on the surge motion velocity, rotation motion velocity and number of blades. Furthermore, the fact that vorticity is created only at the edges of the disc is due to the uniform load distribution. In real wind turbines, there are spanwise variations in the force distribution and thus vorticity is created along the whole span, although the strongest vorticity will be at the root and at the tip.

Figure 4.6 show the vorticity contour for the cases with negative thrust. Here, the vorticity in the y direction is negative, in contrast to what was observed for the positive thrust coefficients.

4.2.4. Pressure field

The contour plots of the pressure field for the cases with a positive thrust coefficient are shown in figure 4.7. In all four cases, the pressure is higher than the atmospheric pressure immediately upstream of the disc and lower downstream of the disc. This reflects the fact that the thrust force exerted on the rotor

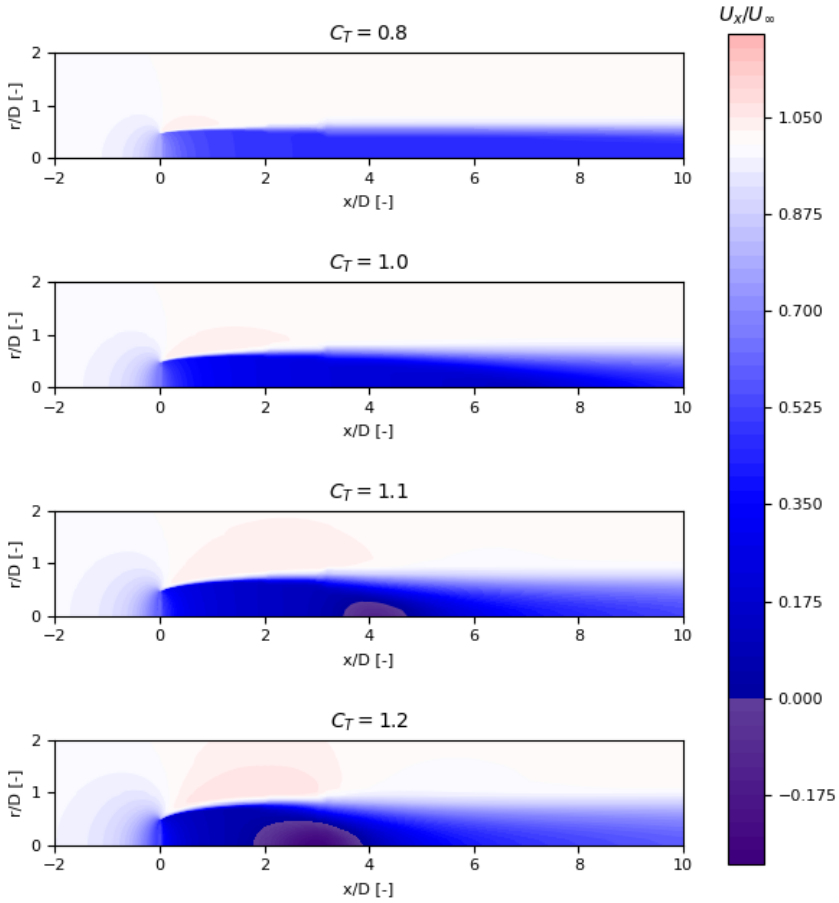

Figure 4.1: Contour plots of the axial velocity around the actuator disc for $C_T = 0.8, C_T = 1.0, C_T = 1.1, C_T = 1.2$.

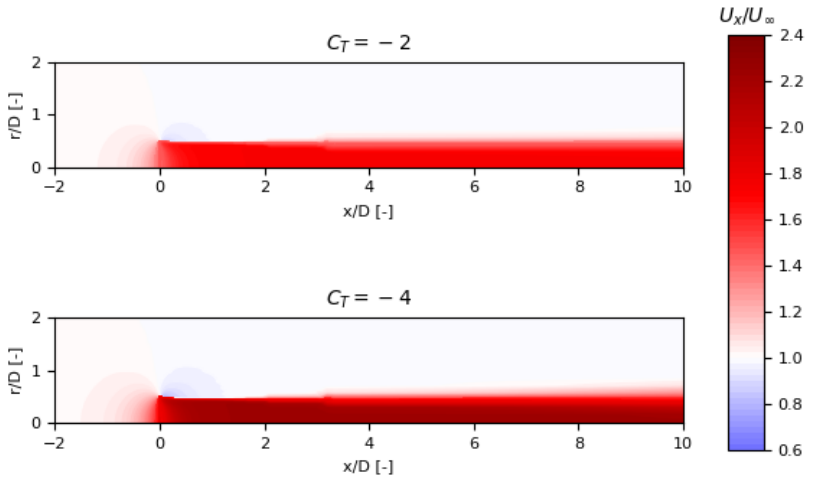

Figure 4.2: Contour plots of the axial velocity around the actuator disc for $C_T = -2$ and $C_T = -4$.

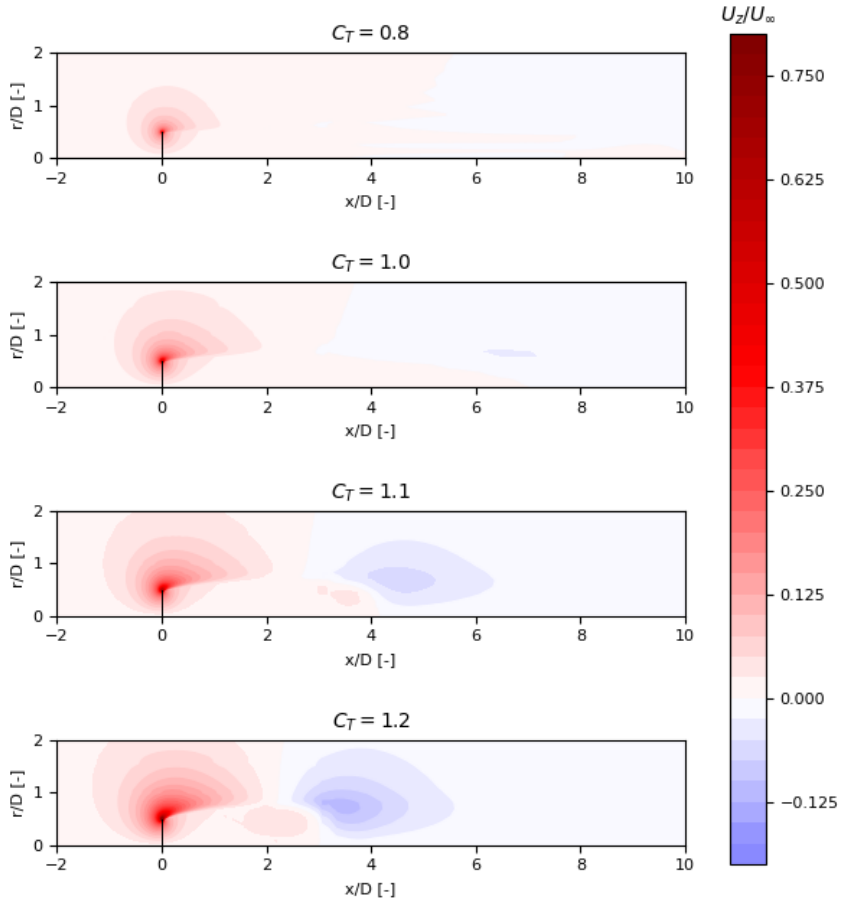

Figure 4.3: Contour plots of the radial velocity around the actuator disc for $C_T = 0.8, C_T = 1.0, C_T = 1.1, C_T = 1.2$.

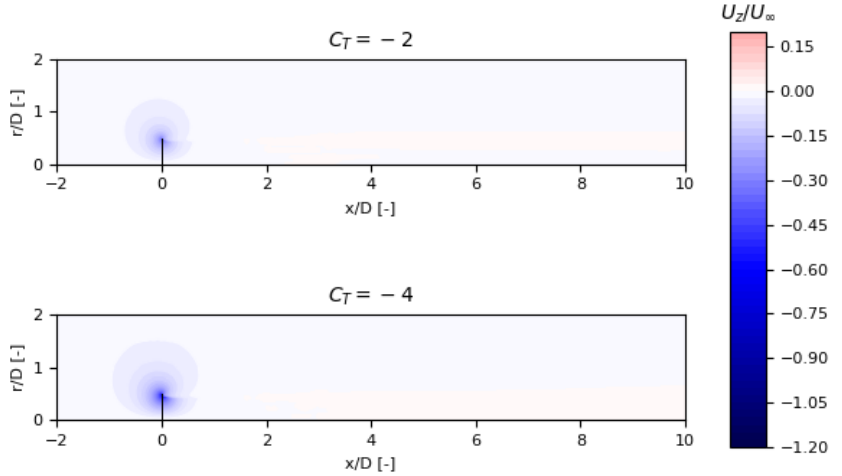

Figure 4.4: Contour plots of the radial velocity around the actuator disc for $C_T = -2$ and $C_T = -4$.

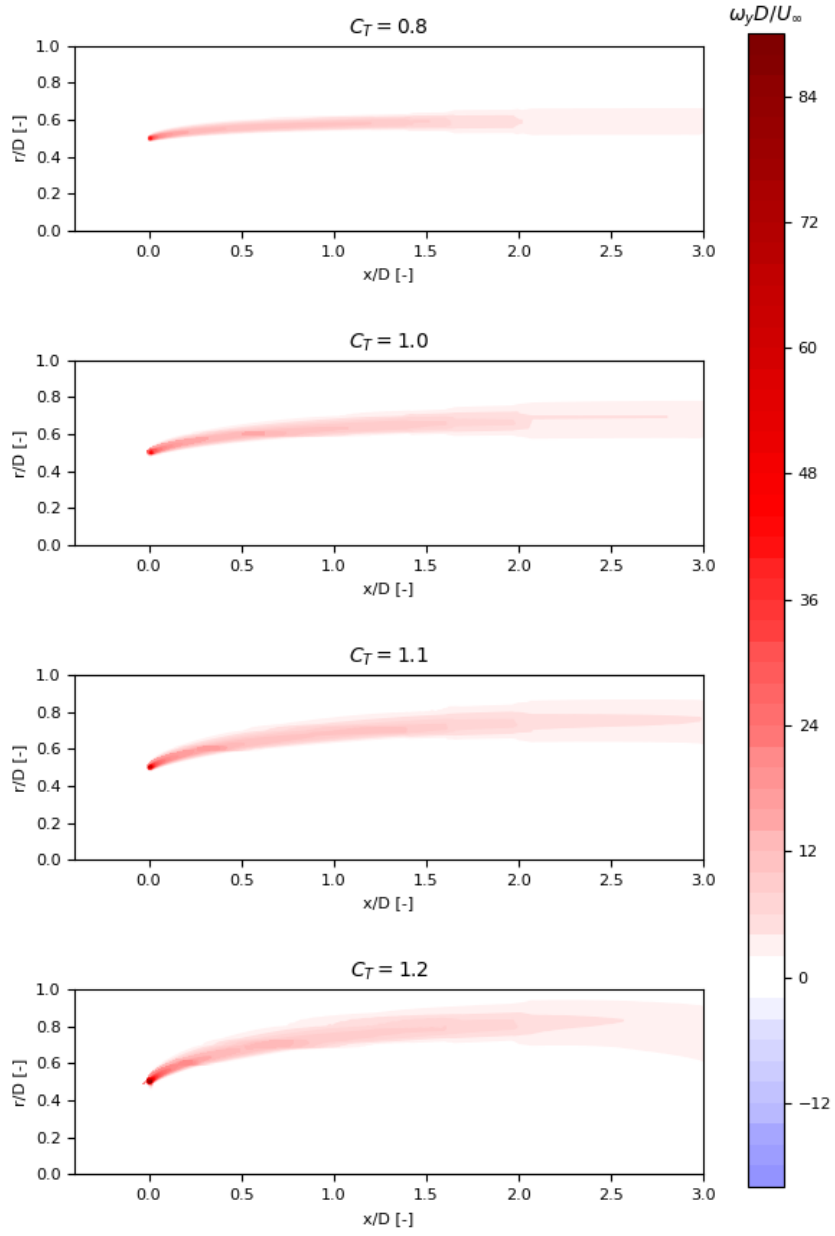

Figure 4.5: Contour plots of the vorticity around the actuator disc for $C_T = 0.8, C_T = 1.0, C_T = 1.1, C_T = 1.2$.

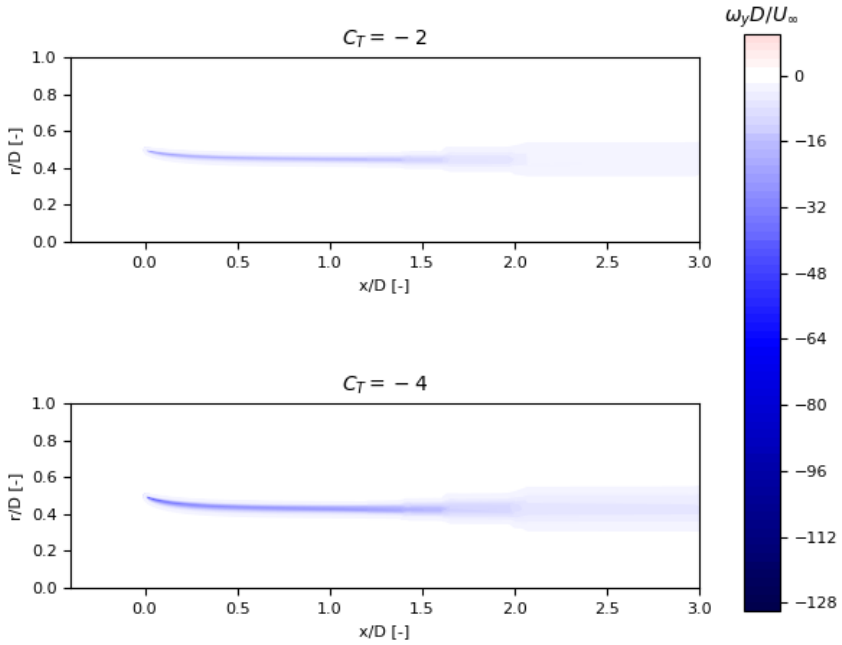

Figure 4.6: Contour plots of the vorticity around the actuator disc for $C_T = -2$ and $C_T = -4$.

is in the downstream direction. After the disc, the pressure gradually reaches again the atmospheric value. This happens faster at lower thrust coefficients. A characteristic of the case with $C_T = 1.2$ is that there is a zone in the far wake where the pressure is higher than the atmospheric pressure.

When the actuator disc is behaving like a propeller, the thrust force on the rotor is directed in the upstream direction and the flow is accelerated. Therefore, the pressure is lower than the atmospheric pressure upstream of the disc and higher downstream, as shown in figure 4.8.

4.3. Induction field of unsteady cases and comparison with the dynamic inflow model

The disc average induction is calculated using formula 3.6. The average induction and the induction at the center of the disc obtained with the actuator disc simulations are compared with the results from the dynamic inflow model introduced in section 3.3. The results for cases with reduced frequency of 1 or 5 and $C_{T0} = 0.5$ are shown in figure 4.9. The cases with $A = 0$ show that the amplitude of the induction oscillations diminishes with increasing reduced frequency, as the flow does not have time to adapt to the fast oscillations of the thrust coefficient. For the same reason, there is a phase lag between the induction and the thrust coefficient that increases when the reduced frequency increases. The cases with $\Delta C_T = 0$ show the effect of the change in position of the disc on the induction field. When the disc moves downwind, it enters its wake and the induction is higher, while when it moves upwind the induction is lower. As the reduced frequency increases, the amplitude of the frequency variations increases. This happens because the actuator disc moves faster than its wake and the wake-rotor interactions are enhanced. Furthermore, the difference between the disc average induction and the induction at the disc center becomes larger. This is particularly noticeable around the induction maximum. When the oscillations of the thrust and the surge motion are combined, as would happen in a real turbine, the two effects are out of phase and partly cancel each other out. This is particularly evident for the reduced frequency of 5. For the reduced frequency of 1, in fact, the variations of ΔC_T cause a strong response, while the effect of the motion at lower frequencies is less strong. Therefore, the oscillation of the induction is similar to the one for the case of the still disc, with a slightly smaller amplitude. For all the cases, it can be noted that the predictions of the dynamic inflow model are in good agreement with the predictions of the CFD actuator disc model.

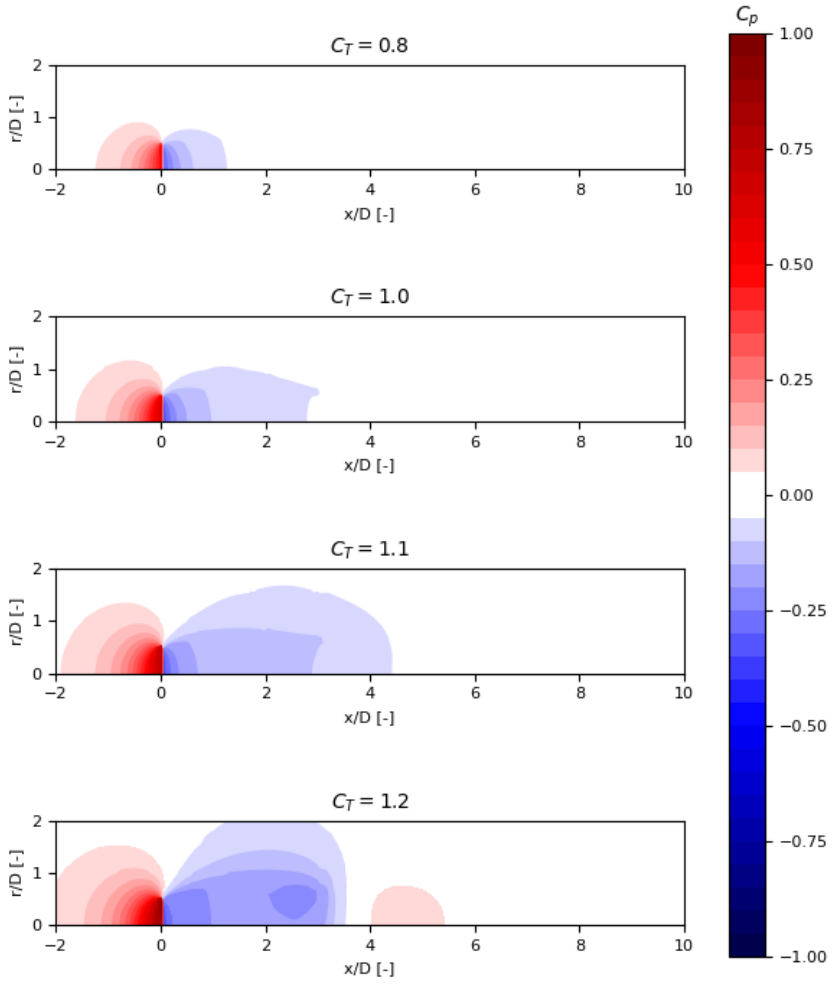

Figure 4.7: Contour plots of the pressure field around the actuator disc for $C_T = 0.8, C_T = 1.0, C_T = 1.1, C_T = 1.2$.

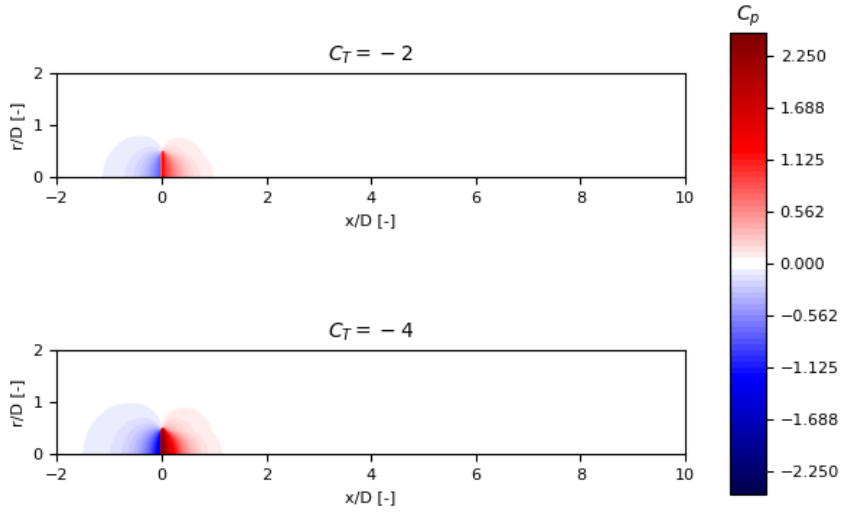

Figure 4.8: Contour plots of the pressure field around the actuator disc for $C_T = -2$ and $C_T = -4$.

Figure 4.10 shows analogous results for $C_{T0} = 0.8$. These cases are more challenging for the CFD actuator disc model, which also for steady heavily loaded conditions predicts a slightly lower induction factor than the one predicted with momentum theory. Analogously, the average induction is slightly lower than the one predicted with the dynamic inflow model for cases with this higher baseline thrust coefficient. For the cases with $\omega_{red} = 5$, the difference between the models is of 0.02. For the cases with $k = 1$ and $\Delta C_T = 0.5$, there is good agreement between the two simulations when the induction is low, but the maximum value of the induction predicted with the dynamic inflow model is higher than the one predicted with CFD. These cases are challenging for the dynamic inflow model because Glauert correction has to be applied. For the cases with the higher reduced frequency, the phase and amplitude of the induction at the disc center are in good agreement with the ones calculated with the dynamic inflow model. In the case with $A = 0.1$, $\Delta C_T = 0.5$ and $\omega_{red} = 5$, the effect of the movement and that of the thrust variation once again cancel out, while for $\omega_{red} = 1$ the induction reaches once again high values and Glauert's correction has to be used within the dynamic inflow model. For real wind turbines, however, it is expected that ΔC_T will be proportional to the maximum velocity of the surge motion, as deduced during the literature review by looking at figure 2.13. Therefore, it is expected that for a ΔC_T of $0.5\ V_{max,red}$ will be close to 0.5 as in the case with $\omega_{red} = 5$, resulting in minimal induction oscillations.

In figure 4.11 the results for two cases with $\Delta C_T = -0.5$ are shown. These cases are not likely to occur in real wind turbines, but they are interesting because they present a situation where the induction oscillations caused by the motion and thrust variations are in phase. Thus, the amplitude of the induction variations is greater and there is an added challenge for the dynamic inflow model. In particular, in the case with $\omega_{red} = 1$ the induction becomes close to 0.5, corresponding in theory to turbulent wake state.

Cases with $\omega_{red} = 10$ were also simulated. Figure 4.12 shows the results for the still actuator disc with varying thrust, for the surging disc with constant thrust and the surging disc with oscillating thrust (respectively, cases 2, 8 and 14 from table 4.1). These cases confirm the observations already made. The effect of the oscillating thrust is mitigated since the oscillations are very fast, while the effect of the movement is more evident. Comparing the three cases with surging disc and constant thrust (cases 6 and 7 in figure 4.10) and case 8, it can be noted that as the frequency of the motion increases the phase of the induction shifts. It looks like the shift happens towards the phase of the position of motion, but it is actually towards a 90°phase shift with the velocity. In fact, the influence of the near wake is maximum when the disc is at the two extremes of its movement and its velocity is equal to zero. The density of the near wake increases when the disc moves downwind and decreases when the disc moves upwind, causing the oscillations of the induction. The maximum and minimum of the induction do not correspond to the points of the cycle with a null disc velocity because of the influence of the far wake. The maximum of the disc average induction is much higher for case 8 with $\omega_{red} = 10$ than for

case 7 with $\omega_{red} = 5$, while there is less difference for the minimum. When the oscillations of thrust and surge motion are combined, the effect of the movement in this case prevails.

To better investigate the wake states that occur in extreme situations, four cases with $\Delta C_T > C_{T0}$ were run. The analysis of the resulting flow field is reported in section 4.4, but from the plots of the induction factor over time from the CFD simulations and dynamic inflow model shown in figure 4.13 some conclusions can already be drawn. For the lowest reduced frequency, $\omega_{red} = 1$, the induction factor is negative for $0 < t/T < 0.2$ and $t/T > 0.975$, indicatively. It is therefore expected that propeller state will occur during the cycle. The disc average induction factor reaches a value of about 0.4 at approximately $t/T = 0.6$, so the rotor is heavily loaded for a portion of the cycle. For $\omega_{red} = 5$, the maximum induction factor is around 0.2. The induction factor at the disc center does not reach negative values, but the disc average is very close to zero so a portion of the disc could enter propeller state. For $\omega_{red} = 10$, the minimum of the disc average induction factor is above zero (around 0.08) and the maximum is around 0.16. Once again, it should be noted that for $\Delta C_T = 1$ the expected $V_{max,red}$ is around 1 as in the last case, so the extreme situations of the two previous cases are unlikely to occur in real wind turbines. Finally, the last case shown in figure 4.13 corresponds to a case of Kyle et al. [28]. Since the thrust reaches negative values, the authors conclude that propeller state occurs. However, the reduced frequency of this case is around 14, so the induction factor stays well above 0 at all points in the cycle since the amplitude of its variations is very small.

Overall, the results of the CFD simulations are in good agreement with those of the dynamic inflow model. The agreement is excellent for cases with a baseline thrust coefficient of 0.5, while in cases with $C_{T0} = 0.8$ the average inductions predicted by the actuator disc model are lower than those obtained with the dynamic inflow model. In many cases, and more evidently at high frequencies, the agreement between the results improves significantly if instead of the disc average induction the induction at the center of the disc is considered for the CFD simulations.

4.4. Velocity, vorticity and pressure fields of unsteady cases

In this section, the contour plots of the velocity, vorticity and pressure fields of a selection of the unsteady cases listed in table 4.1 are presented. For each case, four contour plots are shown, each referring to a particular time instant during the period: $t/T = 0$, $t/T = 0.25$, $t/T = 0.5$ and $t/T = 0.75$. In this way, the behavior of the flow during the entire period is investigated. Particular attention is given to the identification of the streamtube wake states.

The three subsections of this part refer to three typologies of unsteady cases. First, in section 4.4.1 the results of simulations with still disc and oscillating thrust are presented. Next, in section 4.4.2 the cases with surging disc and constant thrust are analyzed. Finally, in section 4.4.3 the simulations examined have both the surging disc and the oscillating thrust.

4.4.1. Simulations with still disc and oscillating thrust

In figures 4.14, 4.15, 4.16 and 4.17 the contour plots of axial velocity, radial velocity, vorticity and pressure fields for the case with still disc and oscillating thrust with $C_{T0} = 0.8$, $\Delta C_T = 0.5$ and $\omega_{red} = 1.0$, referred to as case 0 in table 4.1, are shown. At $t/T = 0$ the thrust is at its minimum, then at $t/T = 0.25$ it has grown to 0.8. At $t/T = 0.5$, it has reached the maximum value of 1.3, then it decreases and at $t/T = 0.75$ it is once again 0.8.

The axial velocity contour plots show that in this case, since the reduced frequency is low, the flow has time to adapt to the thrust oscillations, resulting in a heavily loaded streamtube in some portions of the cycle. The phase lag between the loading and the induction results in the fact that in the second half of the cycle the velocity at the disc is lower than in the first half, and thus the wake expansion is accentuated. Although the induction at the disc is lower during the first half of the cycle, further downstream the flow has been affected by the high loading of the central part of the cycle, to the point that areas with negative velocity are visible at $t/T = 0$ and $t/T = 0.25$. It can therefore be said that in this case the streamtube oscillates between windmill and turbulent wake state. At $t/T = 0.5$, no areas with flow inversion are visible. The radial velocities also resent from the oscillations. At $t/T = 0$, the positive radial velocity at the edge of the disc is low as the thrust coefficient is low, while an area of higher positive radial velocity followed by an area with negative radial velocity is visible at the center of the wake in the area where there is the flow inversion. The alternation of areas with positive and negative radial velocity is also found at the other time steps, although with lower magnitudes, and

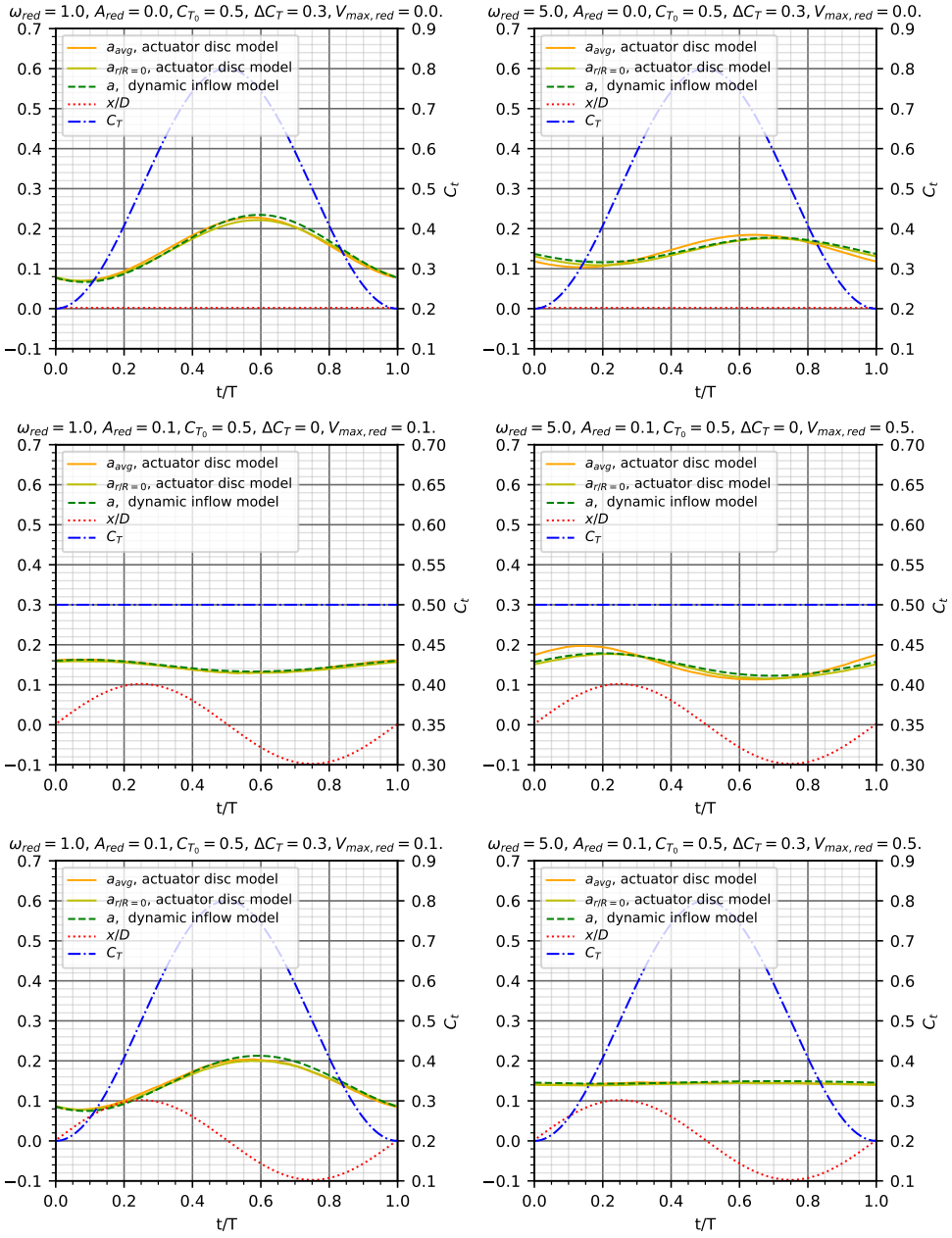

Figure 4.9: Comparison of the results of the induction obtained with actuator disc CFD simulations and dynamic inflow model for cases 3, 4, 9, 10, 15, 16.

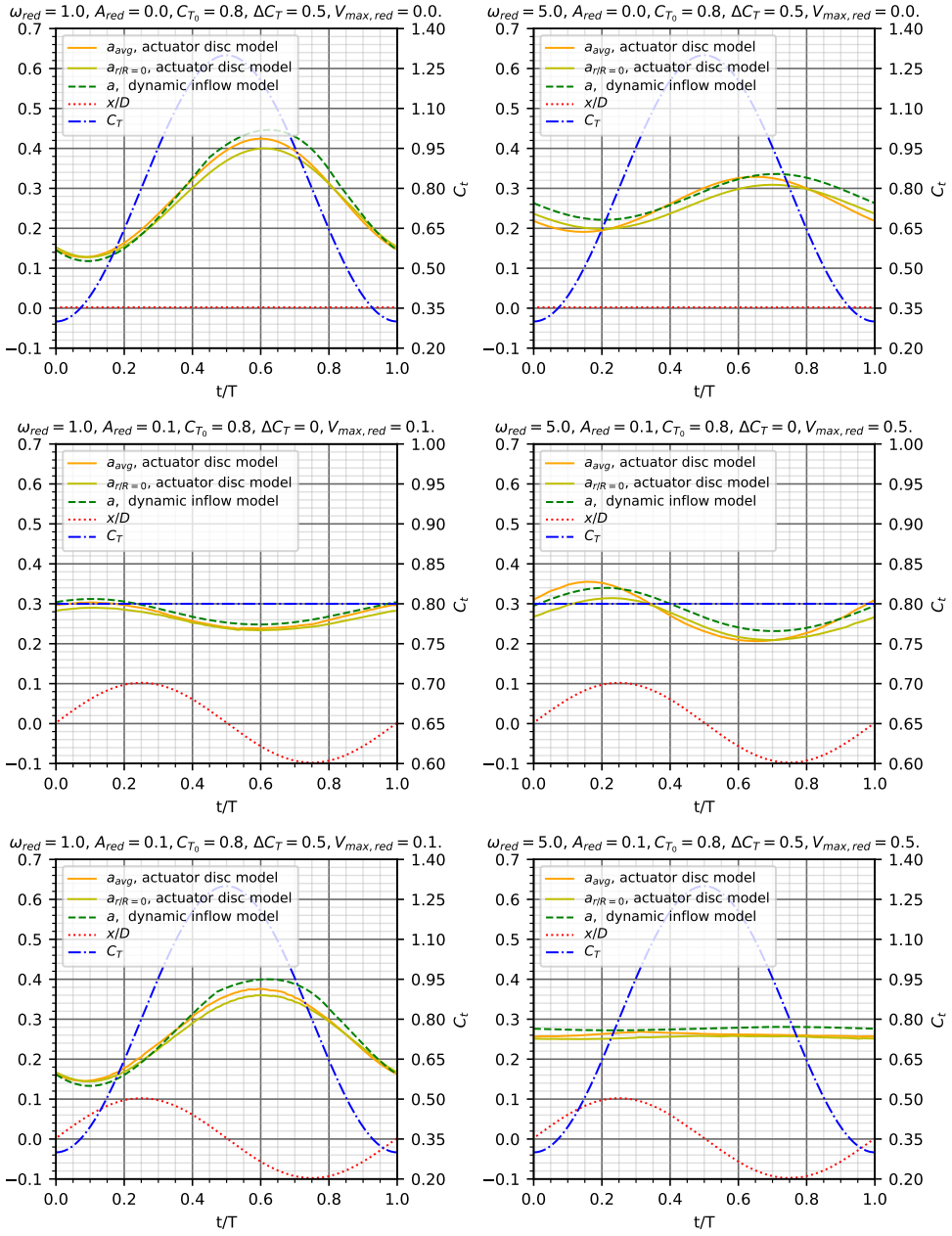

Figure 4.10: Comparison of the results of the induction obtained with actuator disc CFD simulations and dynamic inflow model for cases 0, 1, 6, 7, 12 and 13.

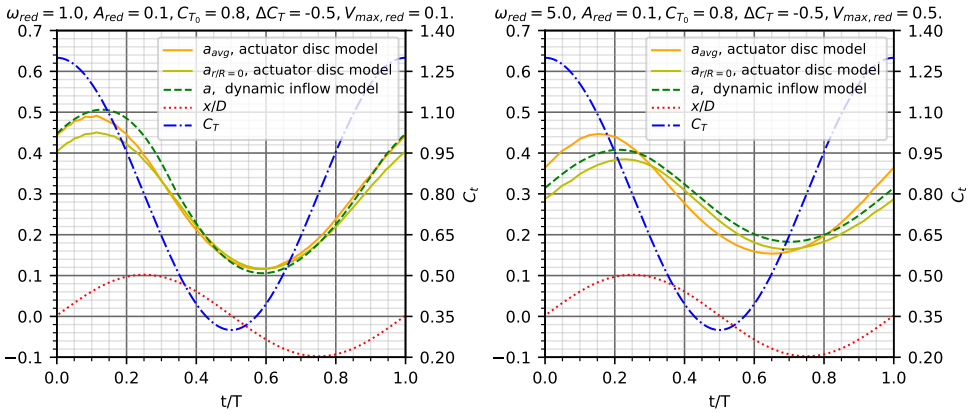

Figure 4.11: Comparison of the results of the induction obtained with actuator disc CFD simulations and dynamic inflow model for cases 18 and 19.

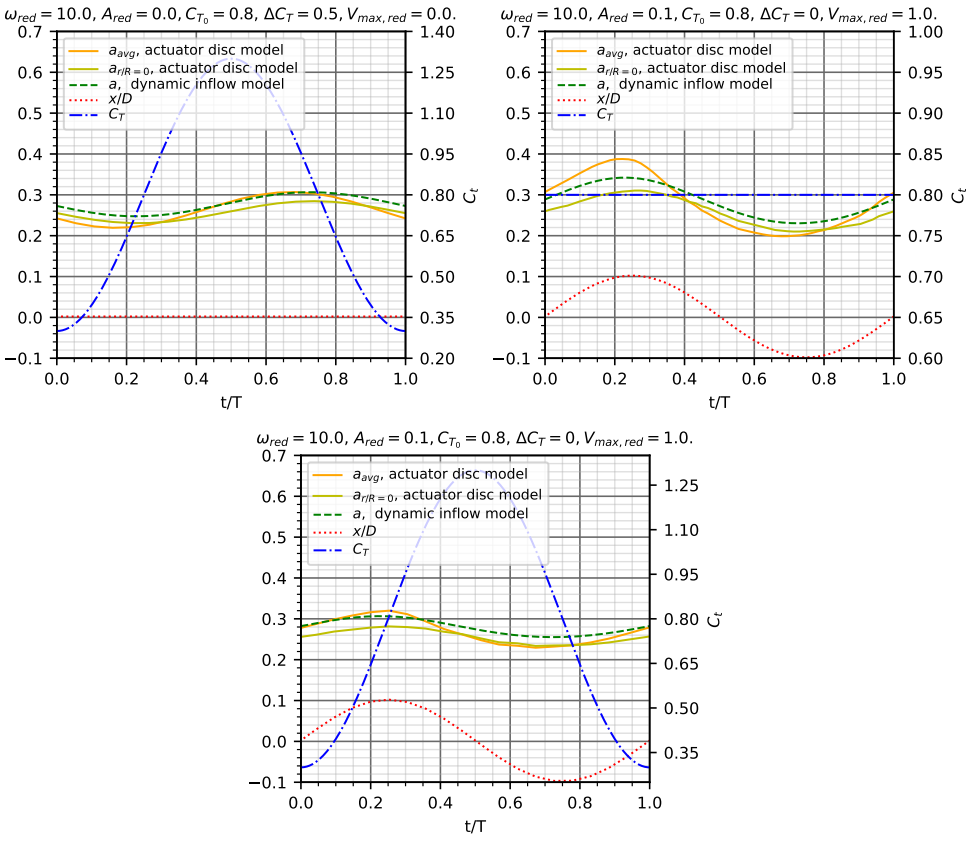

Figure 4.12: Comparison of the results of the induction obtained with actuator disc CFD simulations and dynamic inflow model for cases 2, 8 and 14.

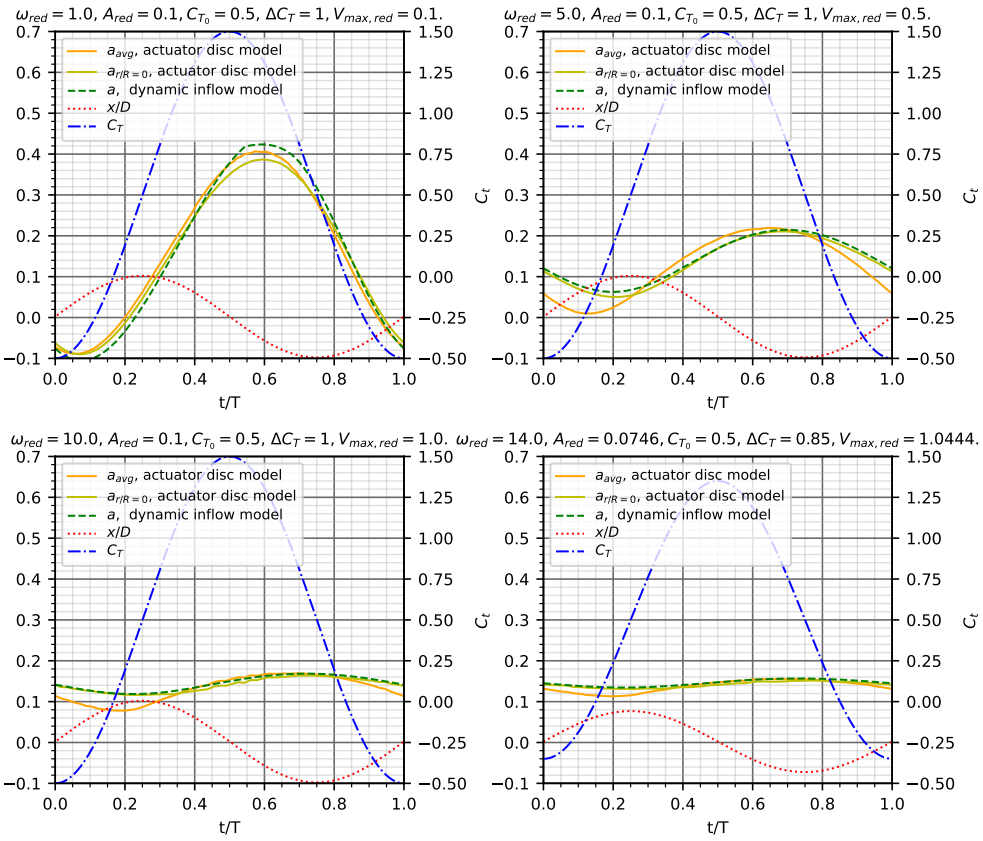

Figure 4.13: Comparison of the results of the induction obtained with actuator disc CFD simulations and dynamic inflow model for cases 21, 22, 23 and 24.

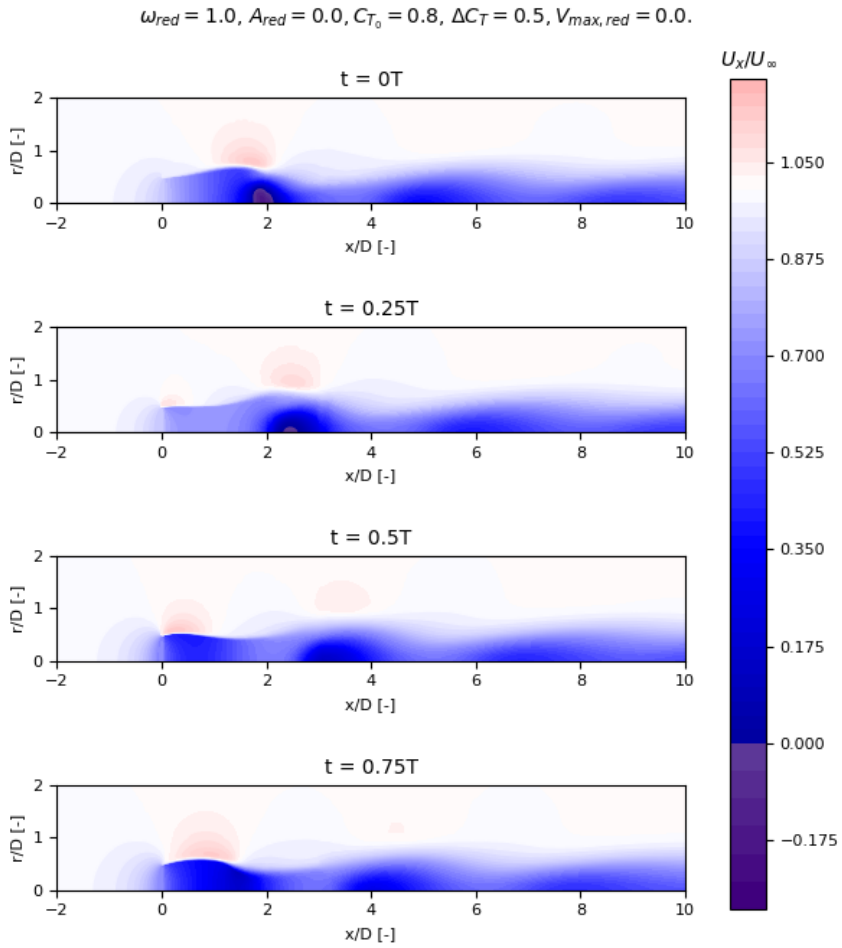

Figure 4.14: Contour plots of the axial velocity field around the actuator disc for case 0.

reflects the expansions and contractions of the wake.

As in the steady case, the vorticity is shed from the edge of the disc and it is positive in y direction. The strongest vorticity is shed during the second half of the cycle. As for the pressure contour plots in figure 4.17, areas of negative and positive pressure coefficients are visible in the wake and are particularly evident at $t/T = 0$ in correspondence of the area with the flow inversion, then there is re-equilibration of the pressure.

It is important to note that if the frequency is increased while maintaining the same baseline thrust coefficient and amplitude of the thrust coefficient oscillations, the characteristics of the flow field radically change. This is evident from the contour plots of the axial velocity field of a case with $\omega_{red} = 5$ (namely, case 1), shown in figure 4.18. Here, there are no areas with negative axial velocity in the wake and thus the streamtube remains in windmill state. Additional plots for case 1 are shown in appendix A.

4.4.2. Simulations with surging disc and constant thrust

The cases with the surging disc and constant thrust can be used to study the effect that surge motion has on the flow field. Figures 4.19, 4.20, 4.21 and 4.22 show the contour plots of the axial velocity, radial velocity, vorticity and pressure fields, respectively, for case 7 with $\omega_{red} = 5$ and $C_T = 0.8$. At $t/T = 0$ the disc is at $x = 0$ and moving downwind with the maximum positive velocity. Then, at $t/T = 0.25$ the disc is at the maximum position downstream and its velocity is null, at $t/T = 0.5$ the disc is again at $x = 0$ while it is moving upwind and finally at $t/T = 0.75$ it is at the maximum upstream position. Since $\Delta C_T = 0$, the effect of the motion is isolated from the effect of the thrust variations. As it can be seen

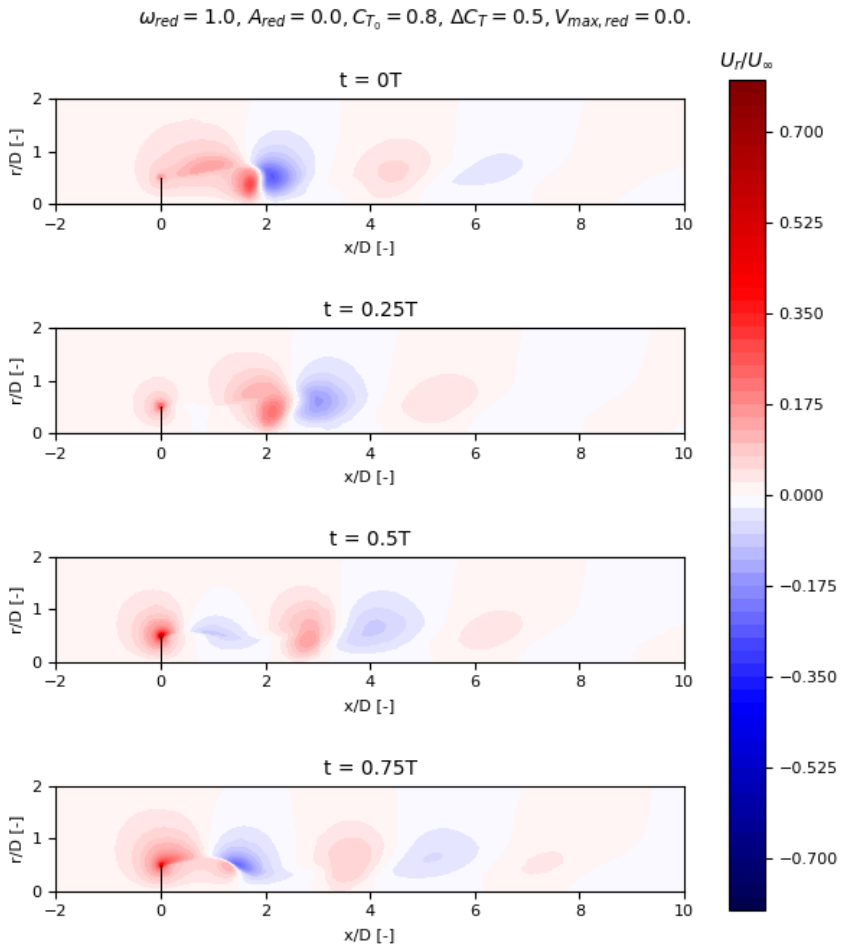

Figure 4.15: Contour plots of the radial velocity field around the actuator disc for case 0.

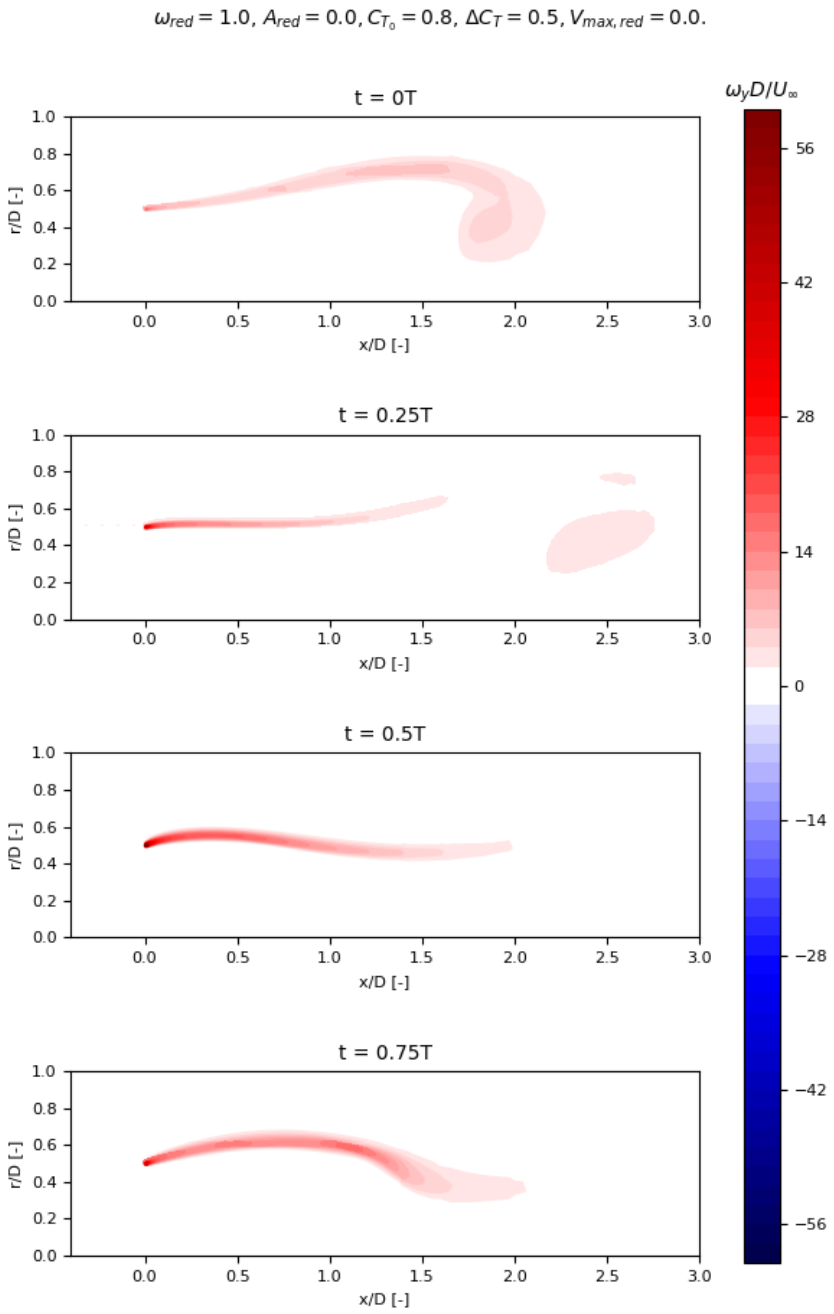

Figure 4.16: Contour plots of the vorticity field around the actuator disc for case 0.

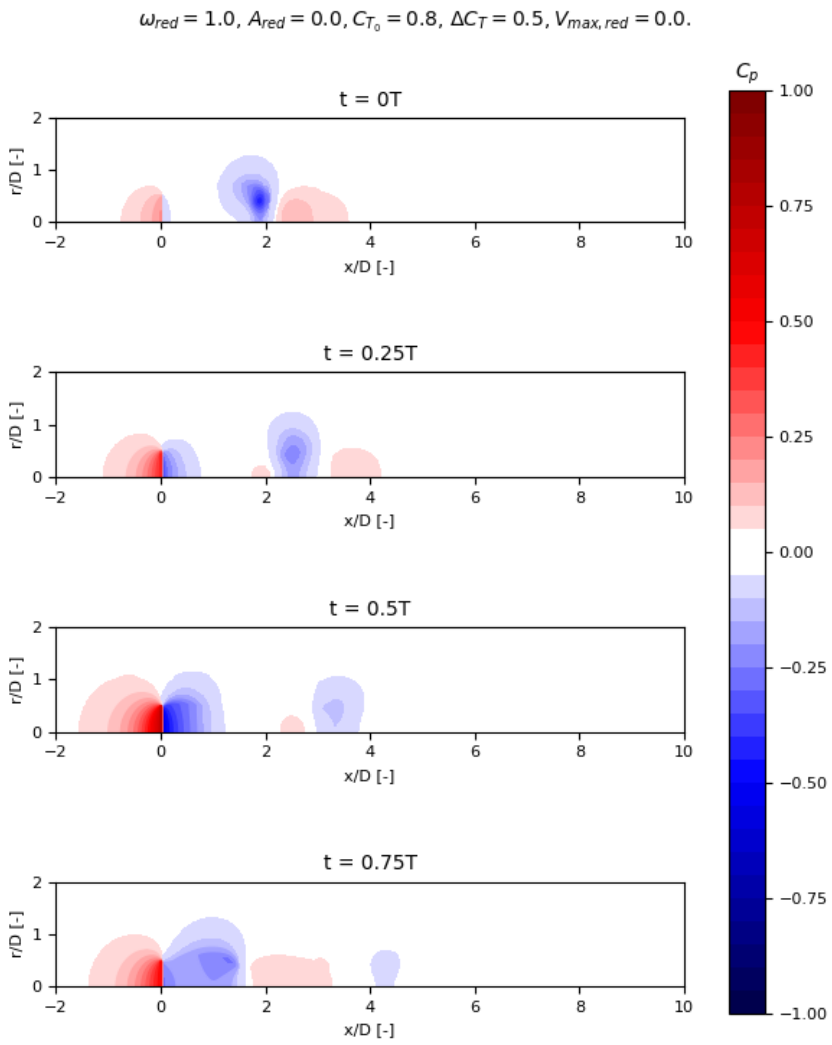

Figure 4.17: Contour plots of the pressure field around the actuator disc for case 0.

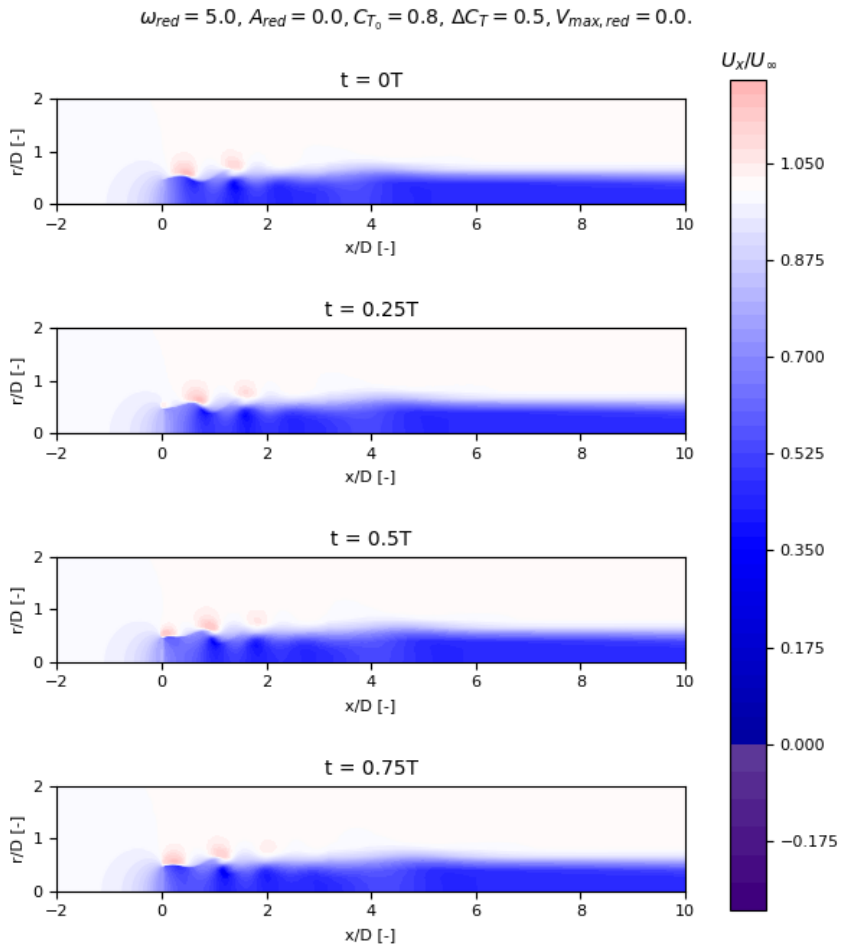

Figure 4.18: Contour plots of the axial velocity field around the actuator disc for case 1.

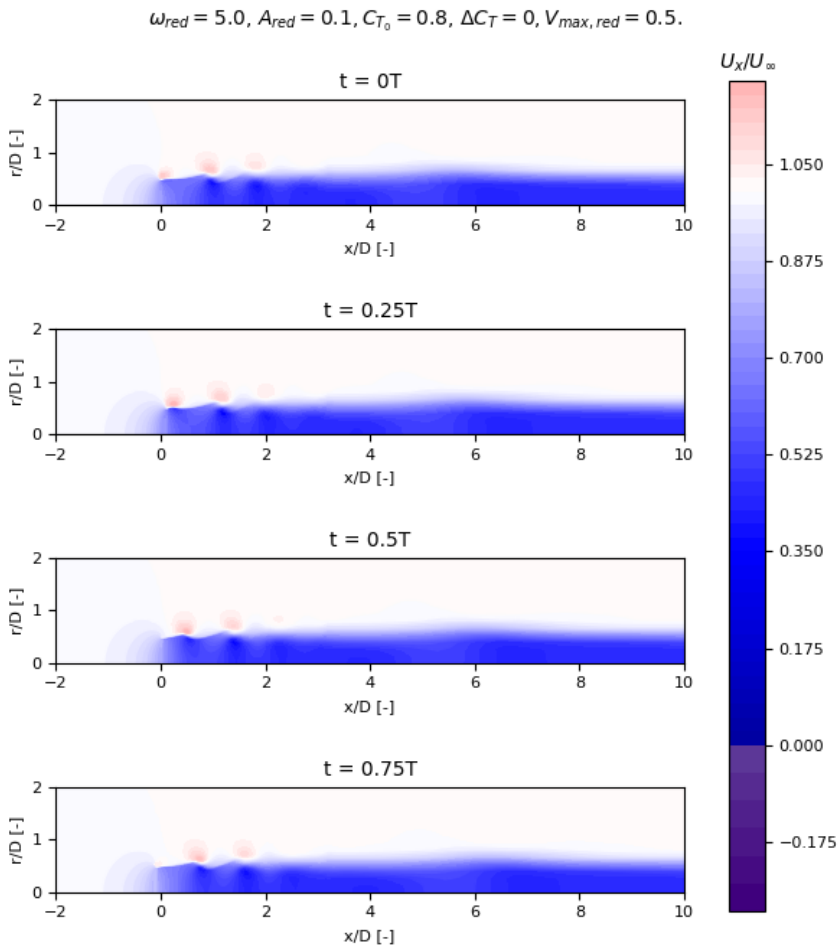

Figure 4.19: Contour plots of the axial velocity field around the actuator disc for case 7.

by looking at this case in figure 4.10, at $t/T = 0.25$ the induction factor is close to its maximum value and at $t/T = 0.75$ it is close to its minimum value.

Looking at the contour plots of the axial velocity field in figure 4.19, it can be seen that even without any thrust coefficient variations, there are zones of lower and higher axial velocity that alternate in the wake. From figure 4.20, it is evident that at the outer border of the wake there are areas with positive radial velocity and areas with negative radial velocity, indicating respectively an expanding and contracting wake. The vorticity contour plots in figure 4.21 further highlight the effect of surge motion. As in the steady case, there is a production of positive vorticity at the edge of the disc and that vorticity then diffuses downstream. As the flow velocity changes during the cycle, however, there is a roll-up of the vortices, which was not seen in the steady case. In the second half of the cycle, since the induction is lower, the velocity of the released vorticity is higher than in the first half. This means that the vorticity travels faster and can catch up with the previously released vorticity. The areas of stronger vorticity correspond to the areas of higher radial velocity.

The contour plots of the pressure field shown in figure 4.22 present the typical characteristics of the windmill state: the area with high pressure is upstream of the disc, while the area with low pressure is downstream. Unlike what happens in the steady case, however, at the border of the wake some circular areas with lower pressure than the surroundings are visible. These areas correspond to the areas where there is an accumulation of vorticity.

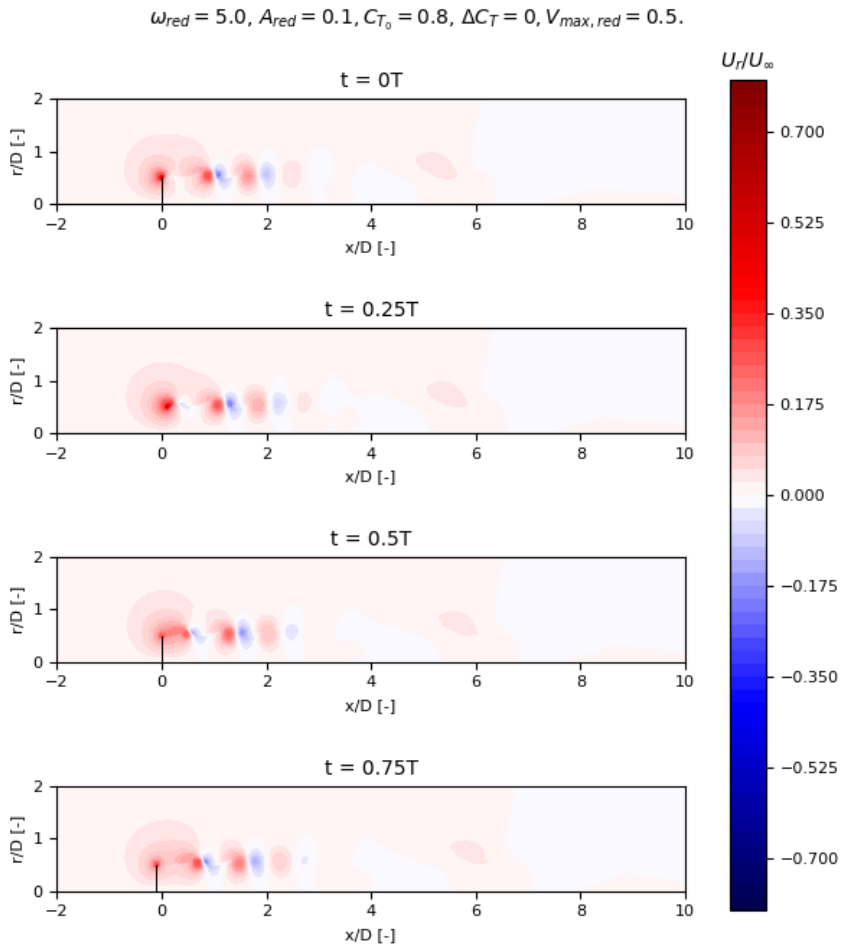

Figure 4.20: Contour plots of the radial velocity field around the actuator disc for case 7.

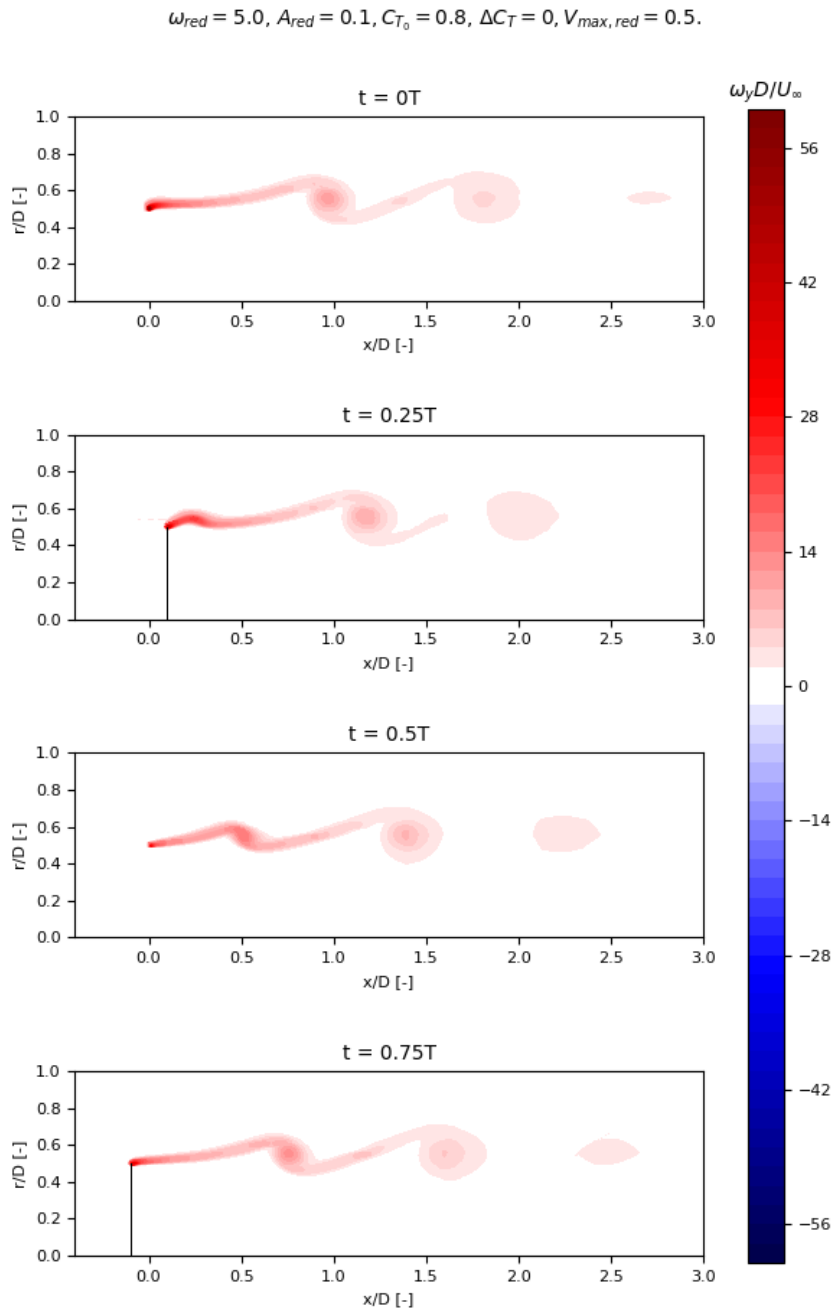

Figure 4.21: Contour plots of the vorticity field around the actuator disc for case 7.

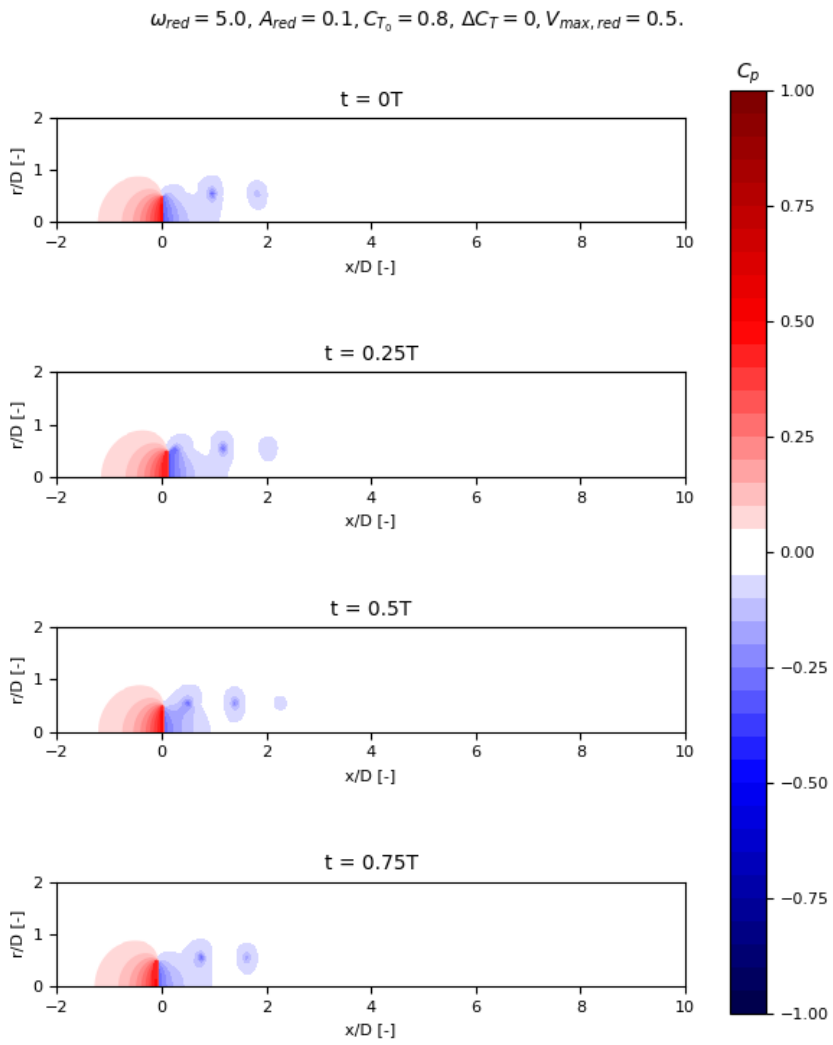

Figure 4.22: Contour plots of the pressure field around the actuator disc for case 7.

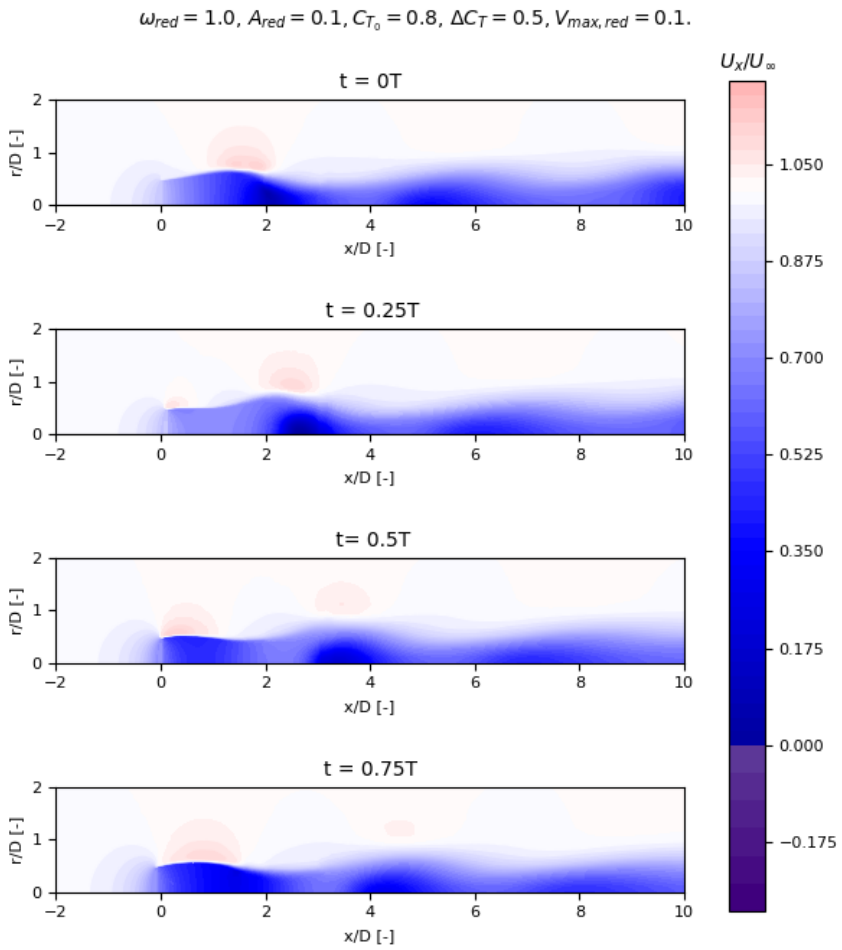

Figure 4.23: Contour plots of the axial velocity field around the actuator disc for case 12.

4.4.3. Simulations with surging disc and oscillating thrust

In this section, cases with both the oscillation on the thrust coefficient and the surge motion will be presented.

In figure 4.23 the contours of the axial velocity of case 12, with $\omega_{red} = 1$, are presented. In the wake, there are areas where the axial flow velocity is close to zero, but it always remains positive. This is the main difference with respect to case 0, which presents the same reduced frequency and thrust characteristics without the surge motion. In this case thus, the surge motion avoids the onset of turbulent wake state. When the reduced frequency is increased to 5, as in case 13 presented in figure 4.24, the flow has less time to slow down and the minimum value of U_x/U_∞ stays above 0.3, with minimal variations visible in the wake. Additional plots for these two cases are presented in appendix A.

To observe the occurrence of propeller state, it is necessary to consider cases with $\Delta C_T > C_{T0}$. Figures 4.25, 4.26, 4.27 and 4.28 show respectively the axial velocity, radial velocity, vorticity and pressure contour plots for case 21, which presents $C_{T0} = 0.5$, $\Delta C_T = 1$ and $\omega_{red} = 1$. In this extreme case, both propeller state and turbulent wake state are entered during the cycle. At $t/T = 0$, the thrust is at its maximum negative value of -0.5 and the axial velocity behind the disc is greater than U_∞, indicating propeller state. At around $1.9D$ downstream in the wake, there is also an area with negative axial velocity, as typical of turbulent wake state. At this time instant, the radial velocity at the edge of the disc is negative, indicating that the wake is contracting, while the area of the inversion is highlighted by an area of strong positive radial velocity that reaches the center of the wake, followed by an area with

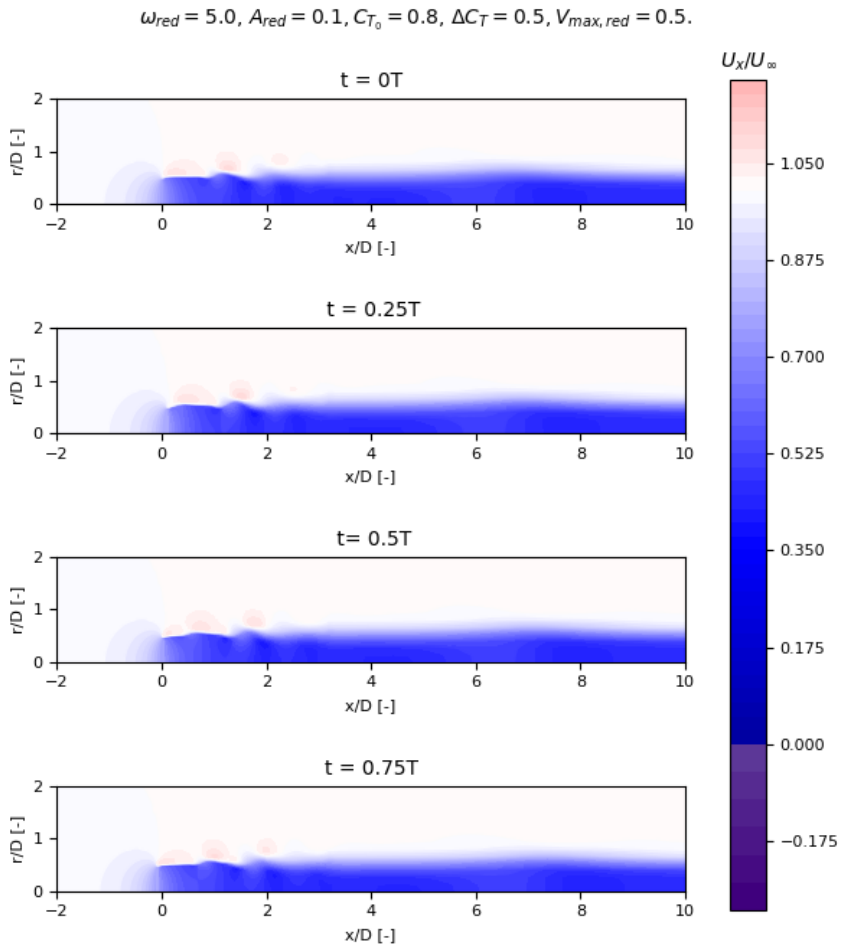

Figure 4.24: Contour plots of the axial velocity field around the actuator disc for case 13.

negative radial velocity. The vorticity and pressure contour plots at $t/T = 0$ near the disc present the typical characteristics of propeller state: the vorticity is negative and the pressure is lower upstream and higher downstream of the disc. At $t/T = 0.25$, the thrust is again positive and the disc is at its maximum downstream position. The axial velocity immediately downstream of the disc is slightly lower than the freestream wind speed, the radial velocity at the edge of the disc is positive, as is the vorticity. The pressure is higher upstream than downstream of the disc. No areas with negative velocity are present in the wake, while there is an area with $U_x/U_\infty > 1$ is located approximately between $x/D = 0.5$ and $x/D = 2$. At $t/T = 0.5$, the axial velocity immediately after the disc is lower and the area in the wake with $U_x/U_\infty > 1$ is reduced and located farther downstream than at $t/T = 0.25$. Finally, at $t/T = 0.75$ this area is no longer visible.

When the reduced frequency is increased to 5, as in case 22, turbulent wake state is not reached and the occurrence of propeller state is limited to a small portion of the cycle. The contour plots of the axial velocity are shown in figure 4.29, while the other contour plots are presented in appendix A. For case 24, the reduced frequency is 13.96 and the reduced amplitude is 0.07. These values were selected by Kyle et al. [28] on the basis of data on the dynamic behavior of the NREL 5 MW reference wind turbine reported by Wayman et al. [63]. Using a full CFD model, the authors obtained an amplitude of the thrust variations equal to 0.85, reproduced in this study to simulate a more realistic, though extreme, case. As shown in figure 4.30, the axial velocity in the wake only presents minimal variations. The vorticity field, shown in figure 4.31, shows that at $t/T = 0$ the vorticity at the edge of the disc is negative, while at the other time steps it is positive. Therefore, the wake is mostly delimited by patches of positive vorticity, interspersed with small areas of negative vorticity. The contour plots of the radial velocity and pressure field are shown in appendix A.

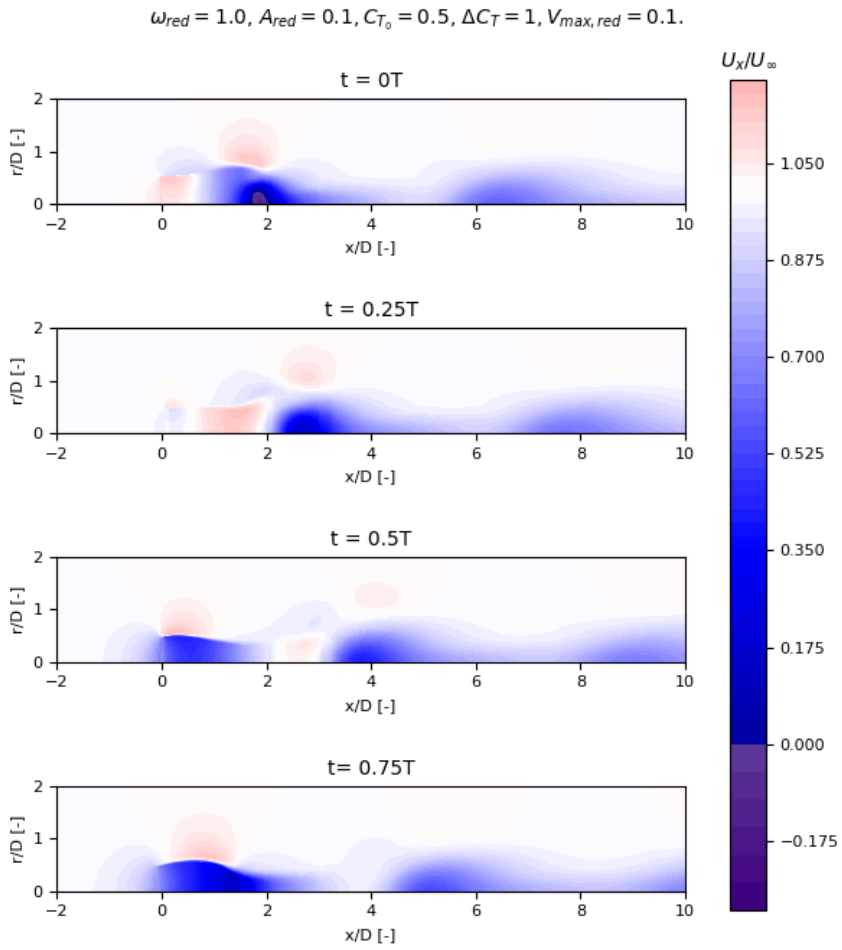

Figure 4.25: Contour plots of the axial velocity field around the actuator disc for case 21.

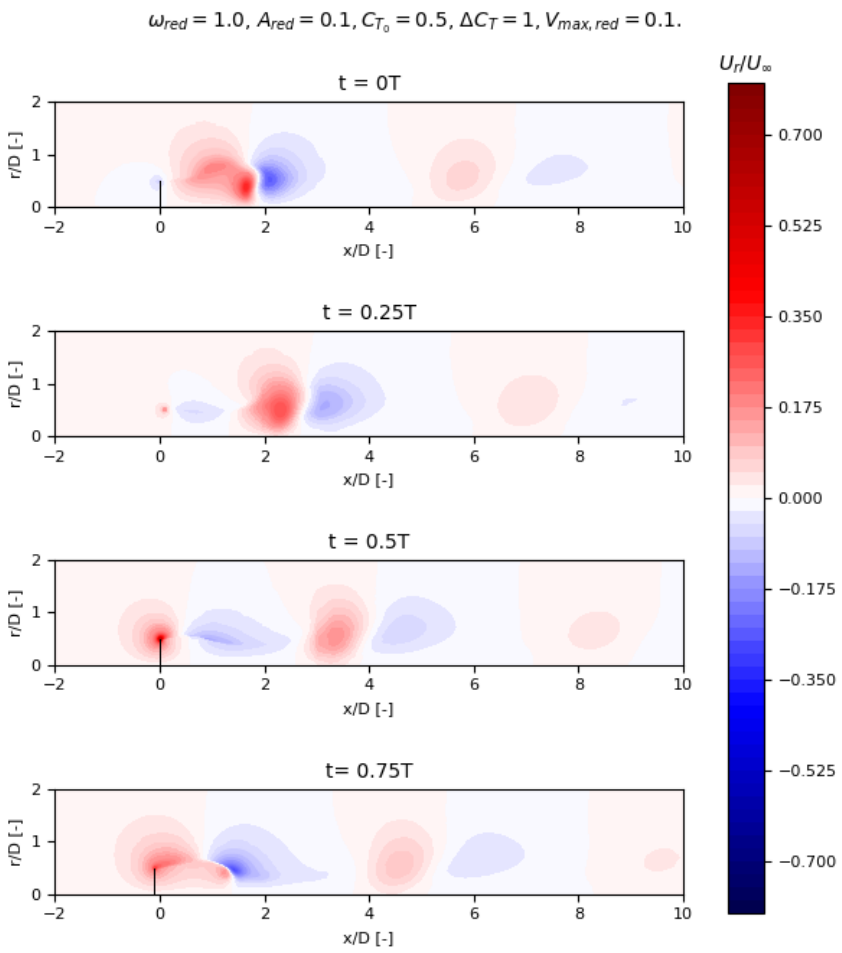

Figure 4.26: Contour plots of the radial velocity field around the actuator disc for case 21.

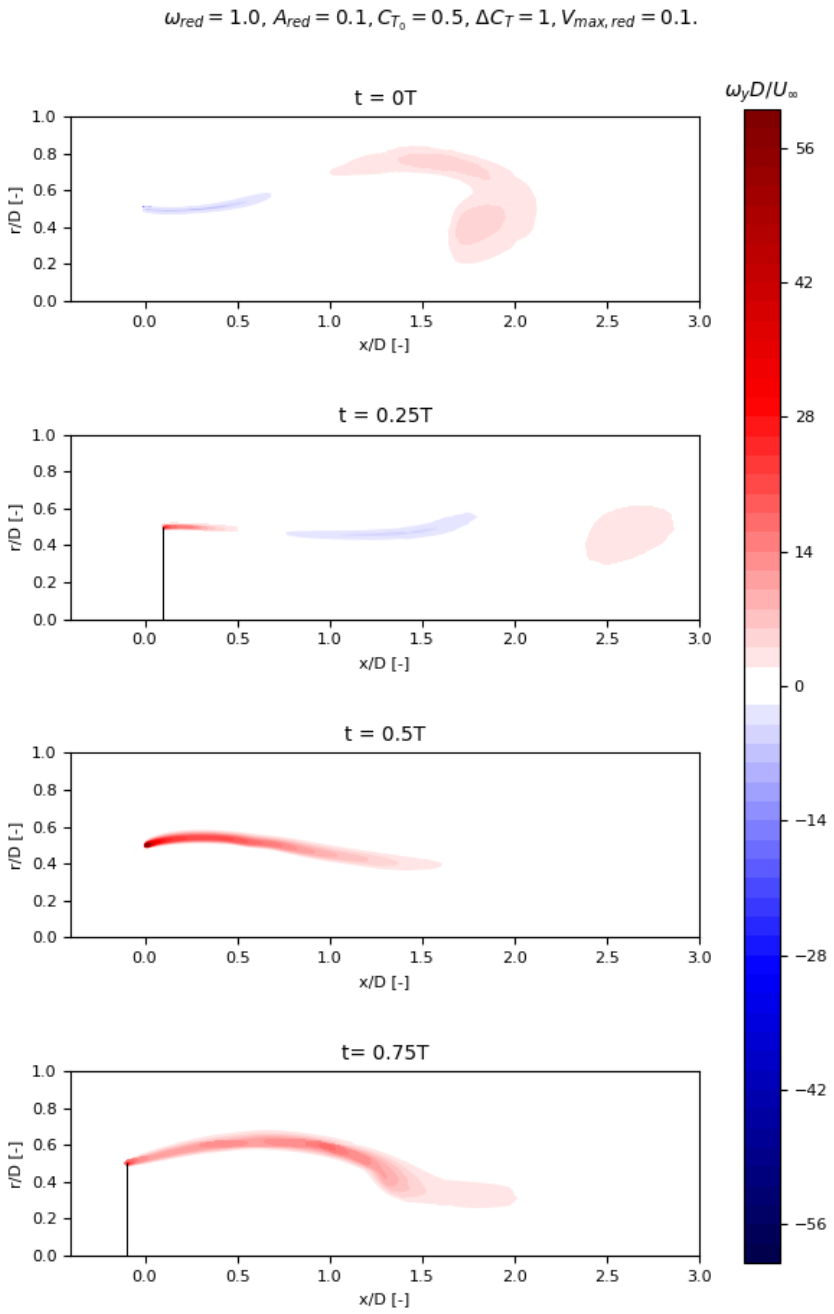

Figure 4.27: Contour plots of the vorticity field around the actuator disc for case 21.

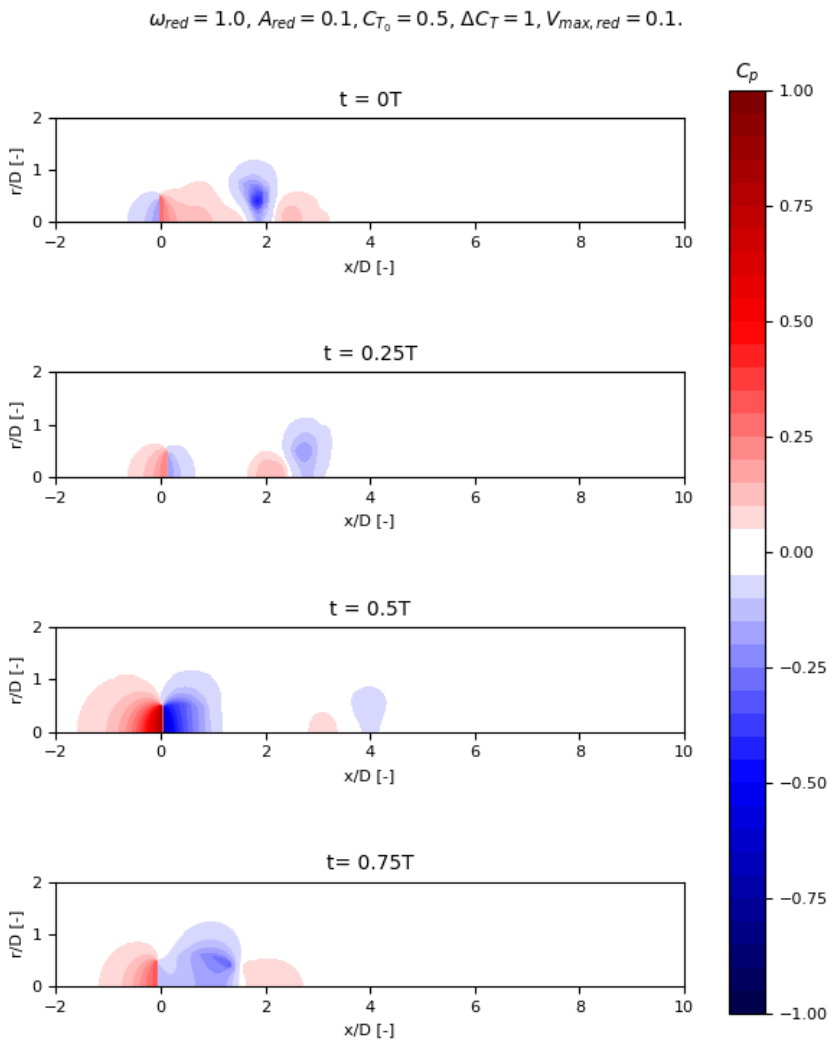

Figure 4.28: Contour plots of the pressure field around the actuator disc for case 21.

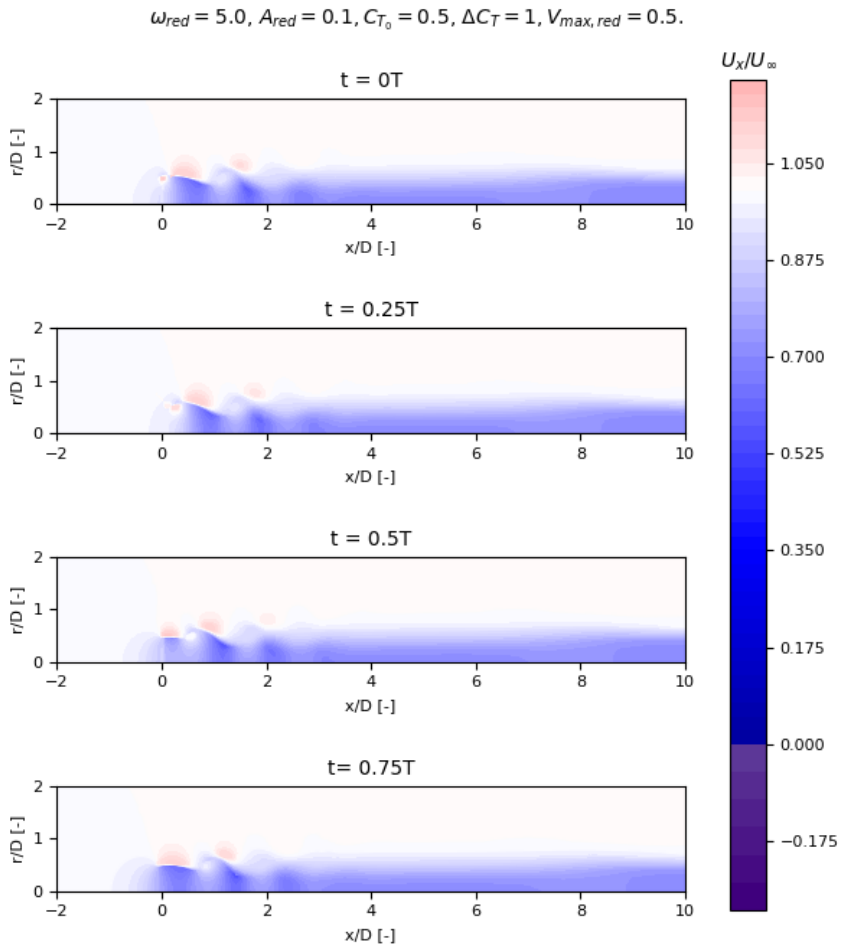

Figure 4.29: Contour plots of the axial velocity field around the actuator disc for case 22.

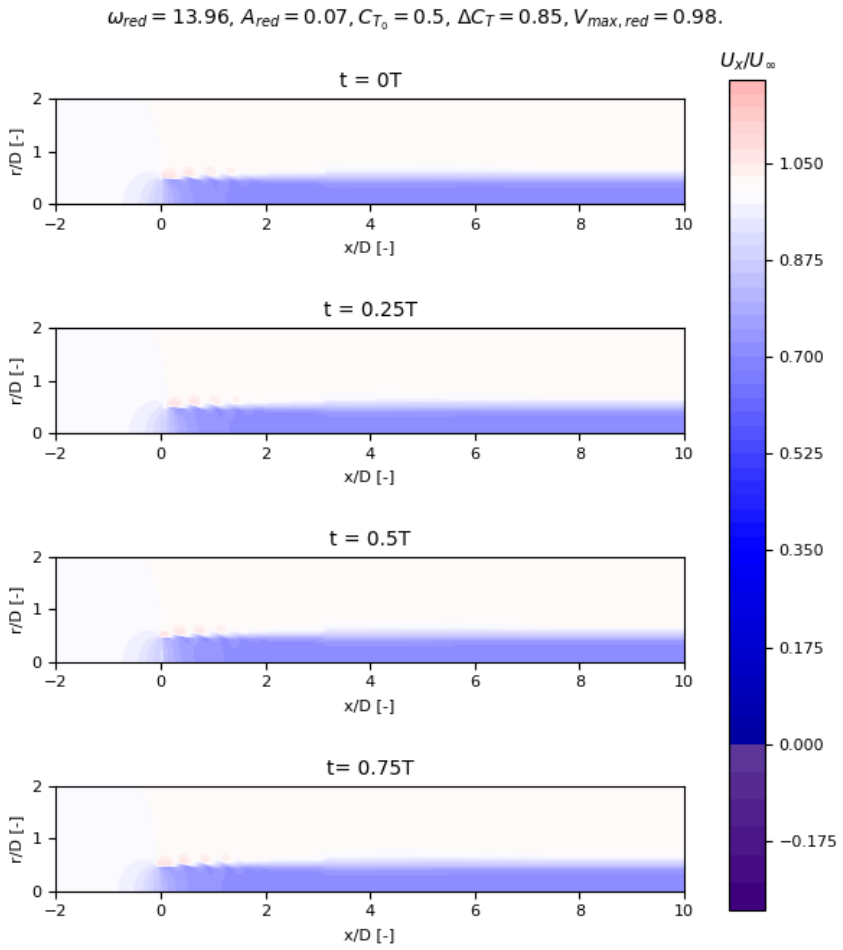

Figure 4.30: Contour plots of the axial velocity field around the actuator disc for case 24.

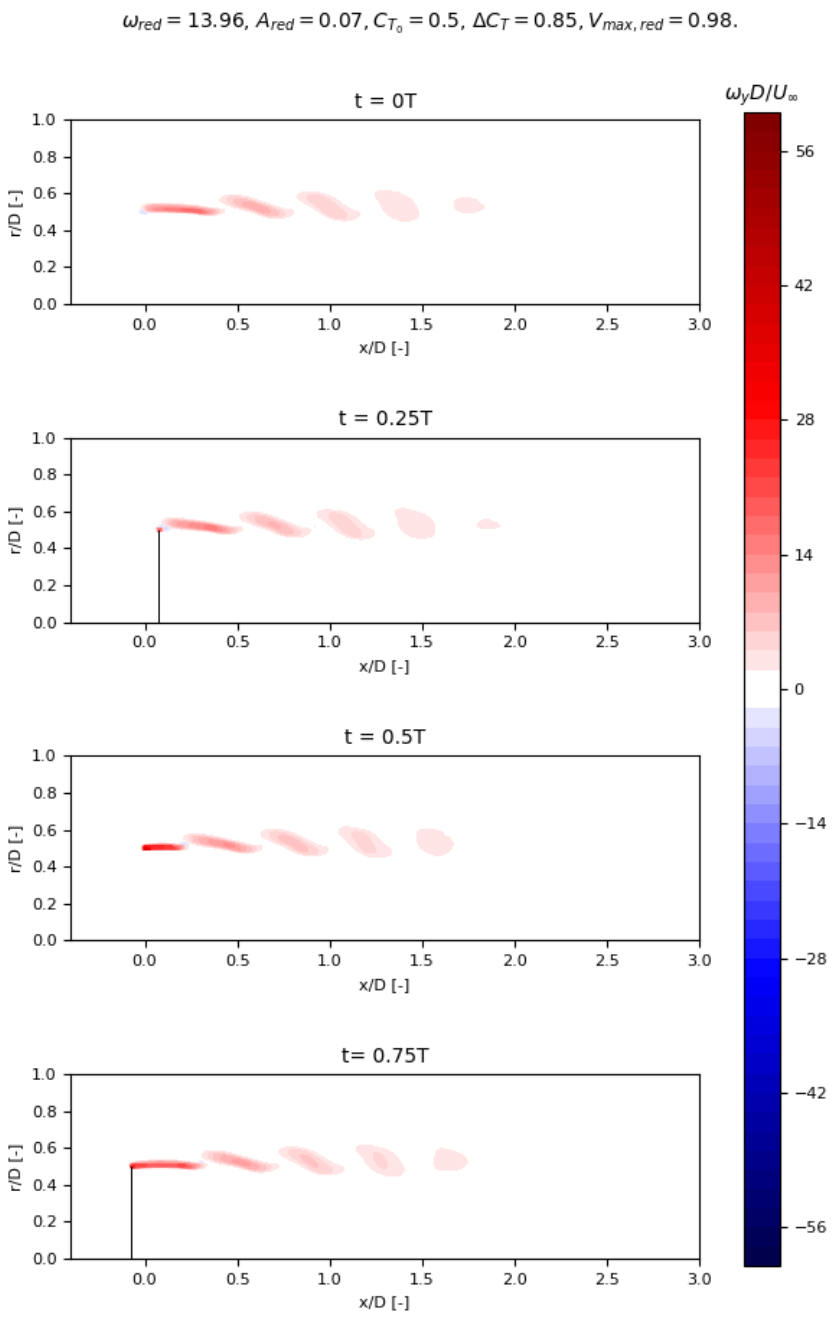

Figure 4.31: Contour plots of the vorticity field around the actuator disc for case 24.

5

Results of the actuator line simulations

In this chapter, the results obtained with the actuator line model with prescribed thrust presented in section 3.2 will be commented. The unsteady cases are characterized by their baseline thrust coefficient C_{T0}, thrust coefficient variation ΔC_T, reduced amplitude A_{red} and reduced frequency ω_{red}. The case studies were selected among the cases in table 4.1, already used for the actuator disc simulations. Due to the fact that during the validation phase the induction obtained with the actuator line model was lower than the induction obtained with the actuator disc model, which in turn was slightly lower than the induction predicted with momentum theory, it was chosen to only simulate cases with $C_{T0} = 0.5$. The tip speed ratio (TSR) was fixed and equal to 7, with the exception of case 24 that reproduces a case used by Kyle et al. [28] and has a TSR of 8.

The chapter is thus organized: first, in section 5.1, the resulting induction is analyzed and compared to the induction field obtained with the actuator disc model and dynamic inflow model. Next, in section 5.2 the velocity, vorticity and pressure fields of some cases, both steady and unsteady, are shown.

5.1. Induction field and comparison with actuator disc and dynamic inflow model

The plots shown in figure 5.1 allow to compare the disc average induction obtained with the actuator line model, actuator disc model and dynamic inflow model for cases 3, 4, 9, 19, 15 and 16 of table 4.1. These cases have $C_{T0} = 0.5$, together with reduced frequencies of 1 and 5. The first two cases have $\Delta C_T = 0.3$ and a still disc, then two cases with $\Delta C_T = 0$ and $A_{red} = 0.1$ are shown. Finally, the thrust coefficient oscillations and surge motion are combined. At this scale, there is no noticeable difference between the induction obtained with the actuator line model and that obtained with the actuator disc model. Consequently, all the considerations made in section 4.3 apply. This reflects the fact that the total thrust coefficient is the same in both cases, although the force distribution differs both radially and azimuthally. A comparison of the induction at $r/R = 0$ and $r/R = 0.9$ obtained with the two CFD models for the same cases is shown in figure 5.2. For all cases, the induction at the rotor center is always lower for the actuator line model than for the actuator disc model. This reflects the radial distribution of the forces in this model: as it can be seen from equation 3.8, the force is linearly proportional to the area of each annulus in which the disc is divided. This means that, contrary to what happened in the actuator disc model, the agreement between the induction calculated with the dynamic inflow model and the induction at the disc center will not be good. At $r/R = 0.9$, the inductions obtained with the two models are very similar. Their amplitudes are greater and their phases are shifted with respect to the inductions at the rotor center. In the cases with oscillating thrust and still disc, the phase lag between the loading and the induction is lower at $r/R = 0.9$ than at $r/R = 0$.

Figure 5.3 shows disc average inductions for the cases with $\Delta C_T > C_{T0}$. Also in these extreme cases, there is good agreement between the average inductions obtained with the two CFD models. The plots of the induction at $r/R = 0$ and $r/R = 0.9$ in figure 5.4 show that there is also good agreement between the induction factors predicted by the two models at $r/R = 0.9$, while there are evident differences for $r/R = 0$. In particular, the actuator line model predicts a lower maximum induction factor for all four cases. For cases 23 and 24, also the minimum value is lower.

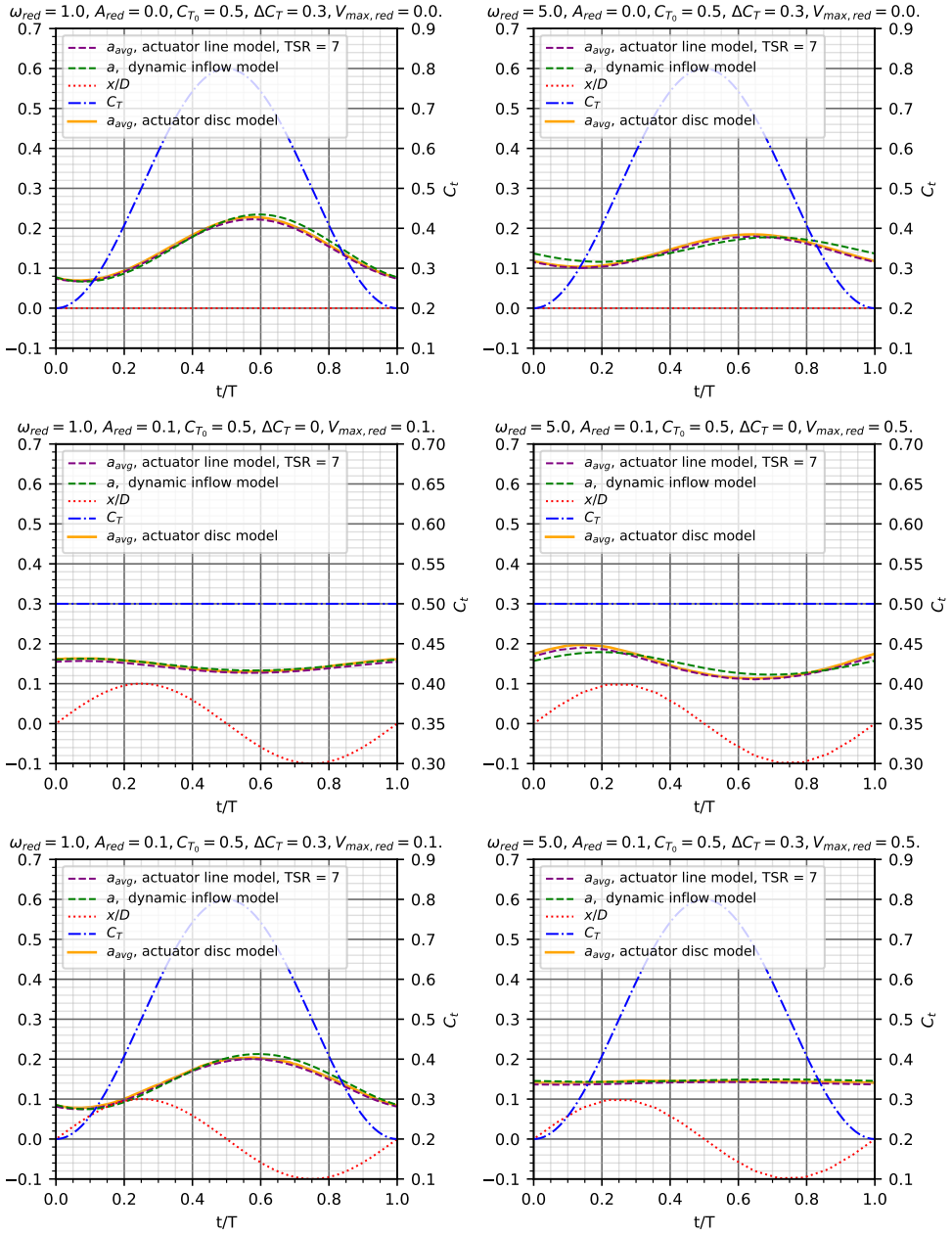

Figure 5.1: Disc average induction factors obtained with actuator line CFD model, actuator disc CFD model and dynamic inflow model for cases 3, 4, 9, 10, 15, 16.

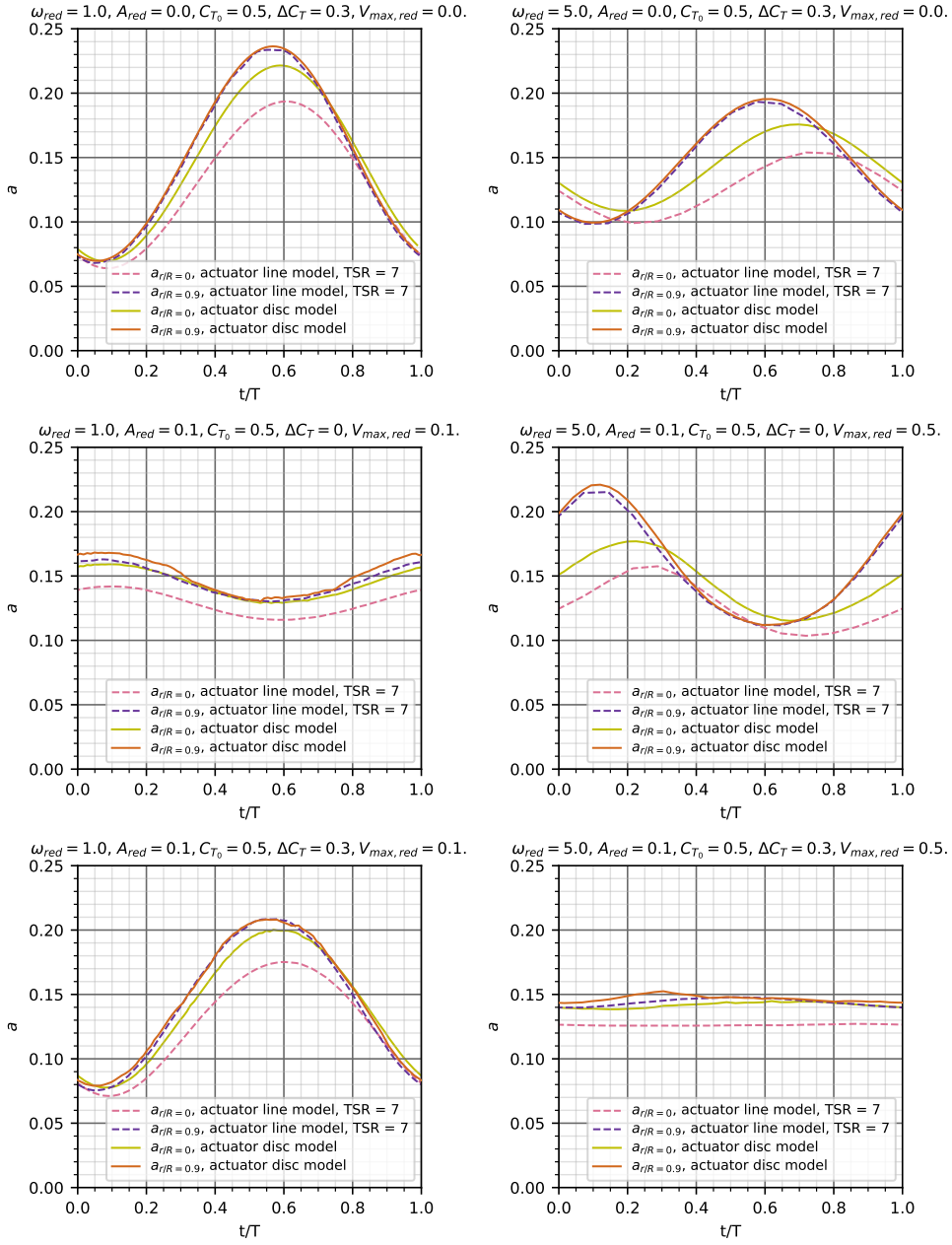

Figure 5.2: Azimuthally-averaged induction factor at different radial positions obtained with actuator line CFD simulations and actuator disc CFD simulations for cases 3, 4, 9, 10, 15, 16.

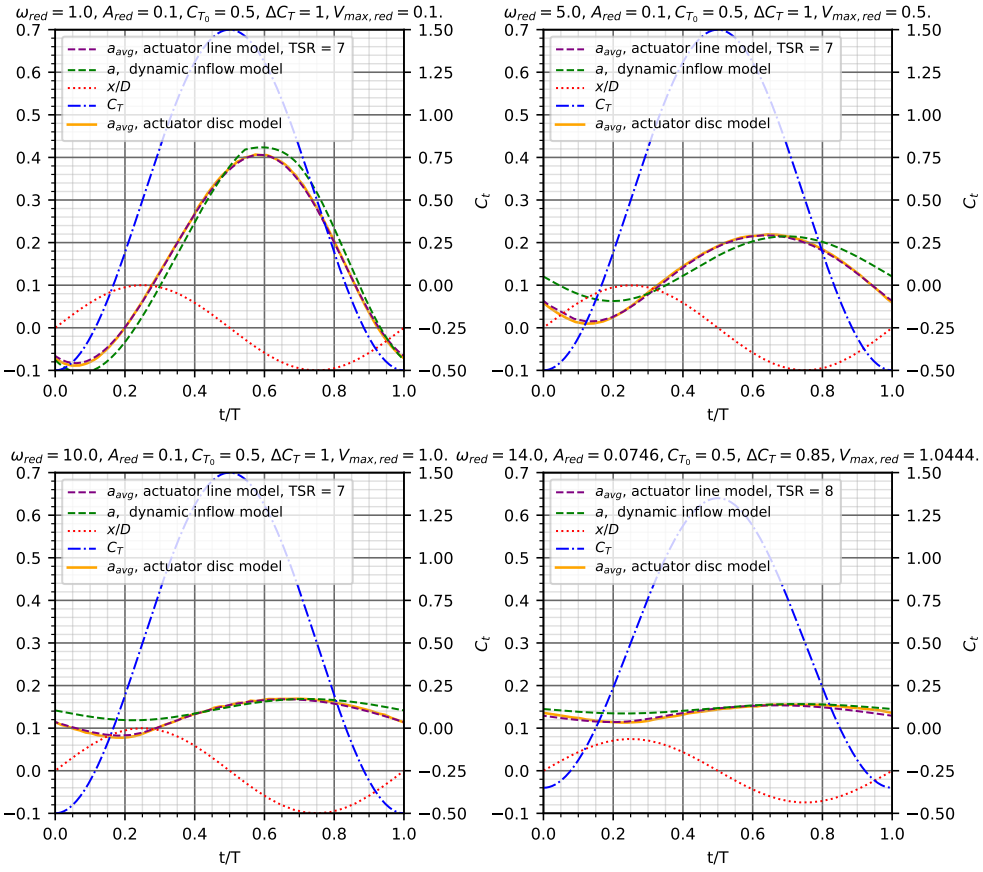

Figure 5.3: Disc average induction factors obtained with actuator line CFD model, actuator disc CFD model and dynamic inflow model for cases 21, 22, 23 and 24.

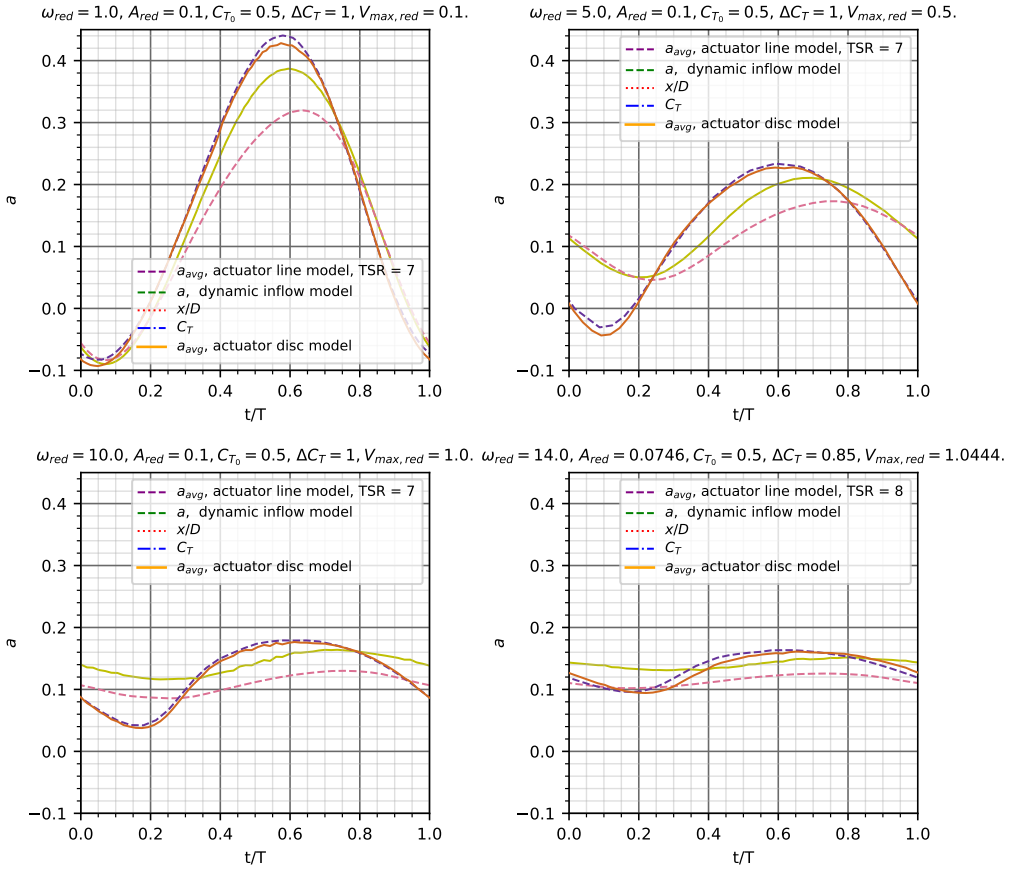

Figure 5.4: Comparison of the Azimuthally-averaged induction factor at different radial positions obtained with actuator line CFD simulations and actuator disc CFD simulations for cases 21, 22, 23 and 24.

5.2. Velocity, vorticity and pressure fields

In this section, the contour plots of the axial velocity, radial velocity, pressure and vorticity fields are shown. All the plots were obtained by cutting the domain with a plane that passes through a blade. First, in section 5.2.1 the plots for the steady cases with $C_T = 0.5$ and $C_T = 0.8$ are presented. Next, the same is done for some unsteady cases.

5.2.1. Contour plots of the steady cases

The axial velocity contour plot in figure 5.5 shows an identical behavior to the analogous plot obtained with the actuator disc simulations in figure 4.1. In fact, in both cases the minimum value of U_x/U_∞ is around 0.45 for $C_T = 0.8$ and -0.1 for $C_t = 1.1$, with a zone of negative axial velocity around $x/D = 4$. The maximum values are around 1.0 for the lower thrust coefficient and around 1.1 for the higher thrust coefficient. Furthermore, there is a symmetry in the results around the plane $r/D = 0$, although in the upper half of the plot the cutting plane passes through a blade, while in the lower half it passes between the other two blades. This is further investigated with the contour plots shown in figure 5.6, taken in the yz plane at the location of the rotor and at $x/D = 0.1, 0.2$ and 0.3. At the rotor, the locations of the blades are visible as the areas with the lowest axial velocities. Already at $x/D = 0.1$, however, this is much less evident. At $x/D = 0.3$, the azimuthal dependence of the results is negligible.

The radial velocity contour plots in figure 5.7 are also very similar to the analogous plots for the actuator disc in figure 4.3, although in this case the maximum values of the radial velocity, occurring at the edge of the disc/blade, are lower for the actuator line than for the actuator disc model.

Figure 5.8 shows the vorticity in the normal direction with respect to the cutting plane. As expected given the lower value of maximum radial velocity, also the maximum vorticity is lower than in the vorticity field obtained with the actuator disc model and shown in figure 4.5. A few discrete tip vortices are visible close to the disc, while further downstream the plots resemble those of the actuator disc simulations. It should also be noted that some vorticity is shed close to the center of the rotor.

The last contour plots, presented in figure 5.9, show the pressure field. The position of the blade, which is directed in the positive r/D direction, is highlighted by the presence of an area with $C_p > 1$. Further downstream, the plots are analogous to the plots showing the pressure fields obtained with the steady actuator disc simulations, shown in figure 4.7.

5.2.2. Contour plots of unsteady cases

In figure 5.10, the contour plots of the axial velocity field at the rotor plane (thus in yz plane) for case 21 with $\omega_{red} = 1$, $C_{T0} = 0.5$ and $\Delta C_T = 1$ are shown. The rotor plane is at $x/D = 0$ at $t/T = 0$ and $t/T = 0.5$, while it is at $x/D = 0.1$ at $t/T = 0.25$ and at $x/D = -0.1$ at $t/T = 0.75$, since the reduced amplitude of this case is 0.1. The plots show that at $t/T = 0$ the velocity in the rotor plane is greater than the free-stream velocity, hence the rotor is acting as a propeller. At the rotor plane, the velocity varies with the azimuthal angle, since farther from the blades the velocity is closer to the free-stream velocity. It is expected that at some point downstream the field will become azimuthally invariant, as shown in figure 5.6 for the steady case. At the other time steps, the position of the blades is highlighted by areas of lower axial velocity, hence the rotor is again acting as a wind turbine.

The contour plots of the axial velocity in a plane cutting a blade for case 21 in figure 5.10 show similar behavior to the analogous plot obtained with the actuator disc simulations in figure 4.25, with propeller state occurring during the first half of the cycle and an area of the wake with negative velocity visible around $2D$ downstream at $t/T = 0$. The main difference between the two results is that for those of the actuator line model the expansions and contractions of the wake at distances greater than $2D$ downstream of the disc are more evident, while the velocity at the outer borders of the wake reaches slightly higher values. This, however, may be a numerical effect caused by the numerical schemes or meshes used. In this extreme case, both propeller state and turbulent wake state are entered during the cycle, while there is no sign of vortex ring state.

Figure 5.12 shows the axial velocity field of case 24, reproduced from [28], having $\omega_{red} = 13.96$ and a tip speed ratio of 8. At this high frequency, the differences with the axial velocity field obtained from the actuator disc model and shown in figure 4.30 are more evident. In fact, areas with higher and lower velocity alternate in the wake with the rotational frequency of the blades until around $2D$ downstream. Nevertheless, it appears that the streamtube remains in windmill state at all times. Furthermore, it seems that the recovery of the wake velocity happens faster. However, no general conclusions can

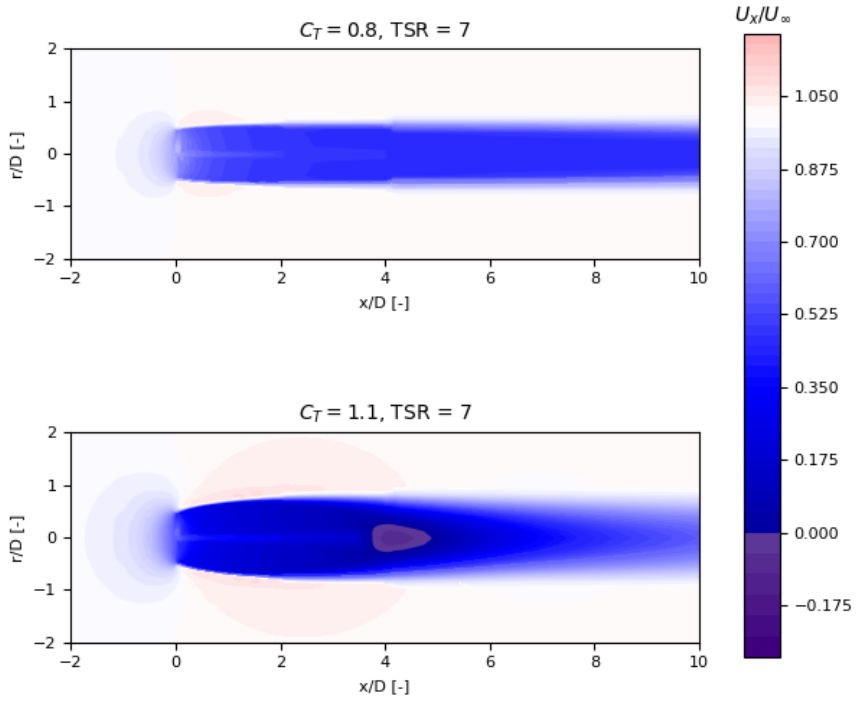

Figure 5.5: Contour plots of the axial velocity field in a plane cutting one blade for $C_T = 0.8, C_T = 1.1$.

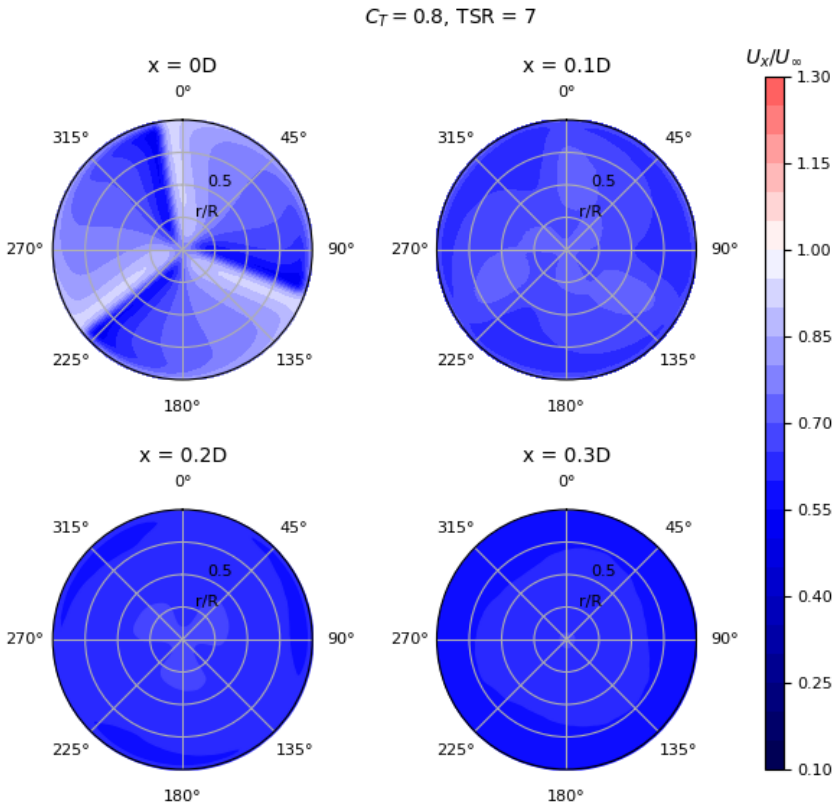

Figure 5.6: Contour plots of the axial velocity field at the actuator line and at various positions downstream.

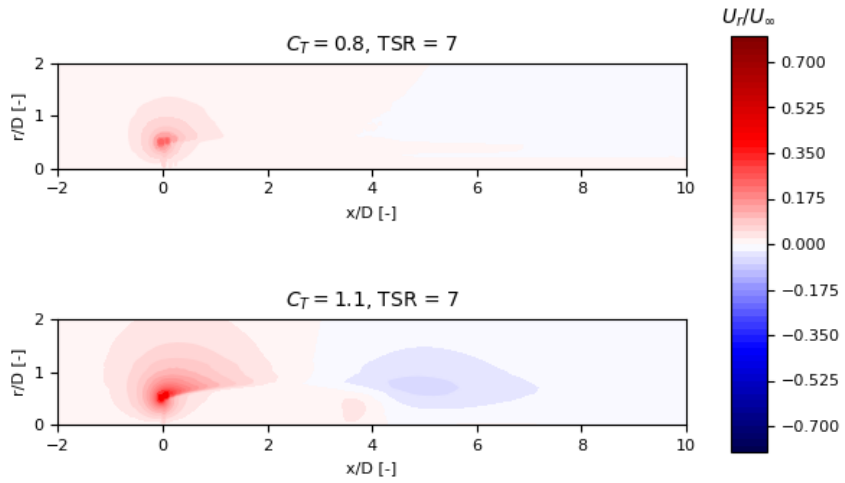

Figure 5.7: Contour plots of the radial velocity field in a plane cutting one blade for $C_T = 0.8, C_T = 1.1$.

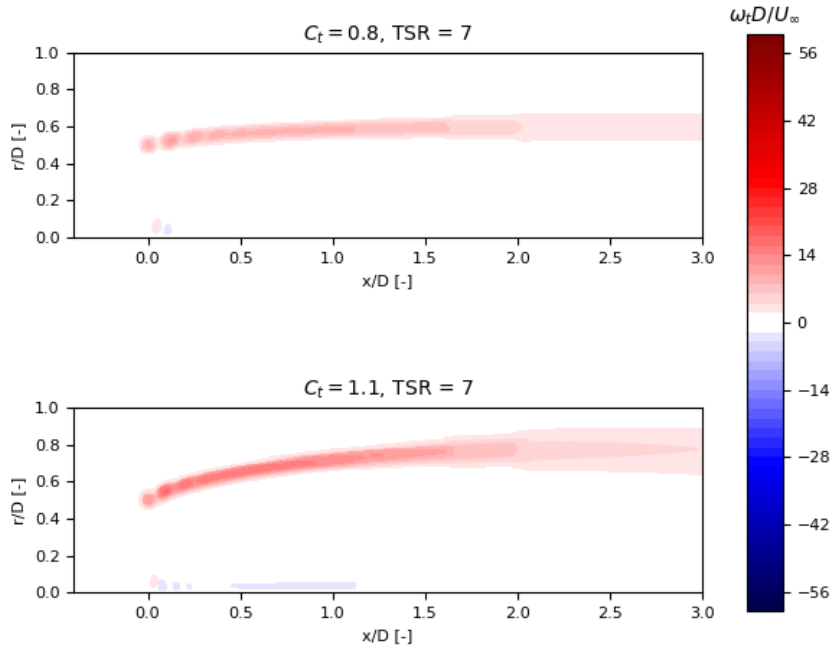

Figure 5.8: Contour plots of the vorticity field in a plane cutting one blade for $C_T = 0.8, C_T = 1.1$.

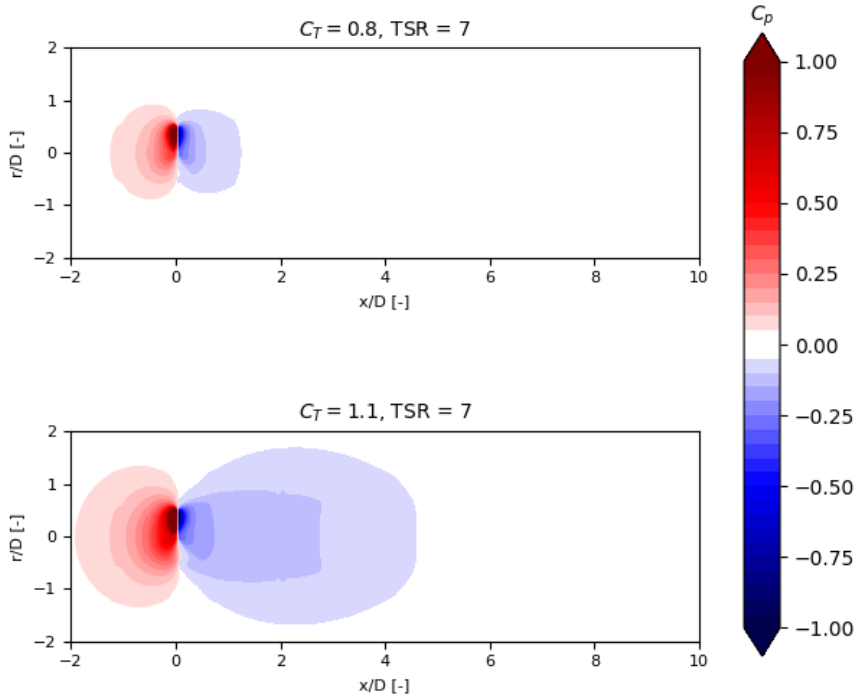

Figure 5.9: Contour plots of the pressure field in a plane cutting one blade for $C_T = 0.8, C_T = 1.1$.

be drawn from this phenomenon as neither of the models was built to accurately model the far wake. The contour plots of the tangential vorticity in figure 5.13 show some negative and positive vorticity at $r/D = 0$ and distinct positive tip vortices. Here, the phenomenon of vortex pairing caused by the different convective velocities of the vortices is evident. The other plots for these cases are shown in appendix B.

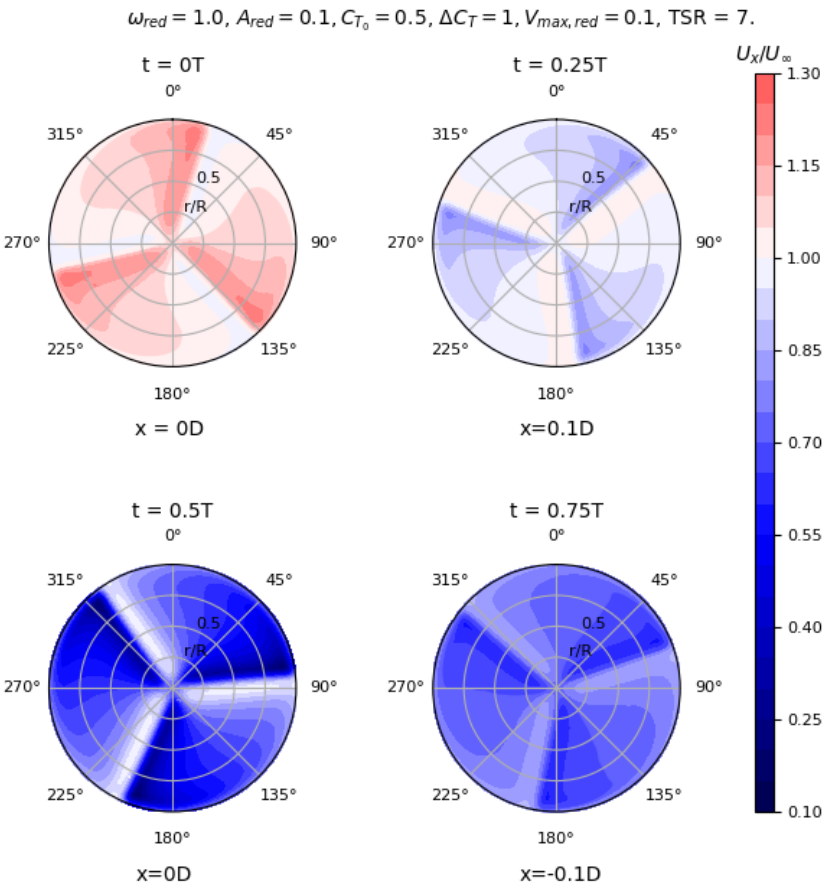

Figure 5.10: Contour plots of the axial velocity field at the actuator line position for case 21.

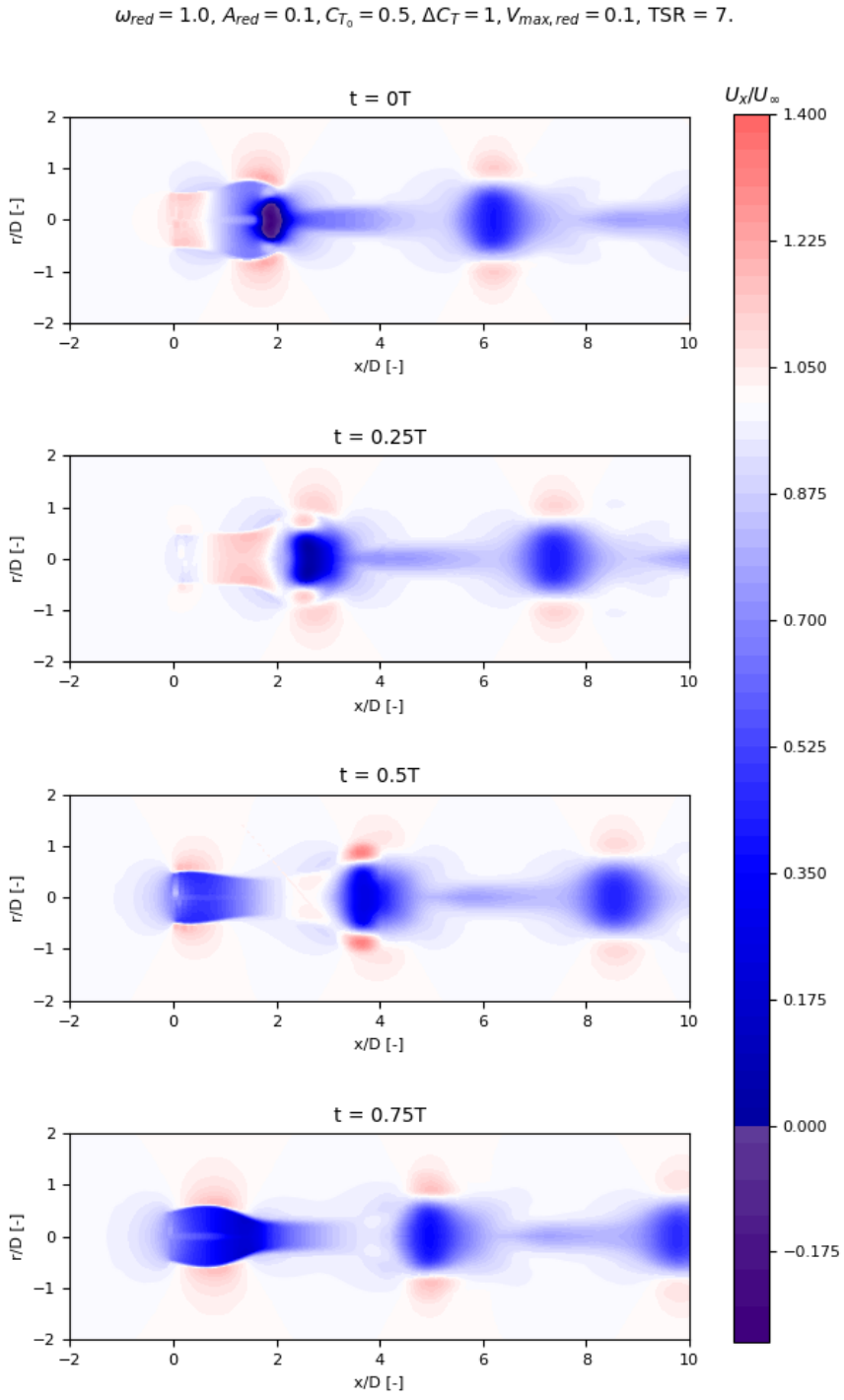

Figure 5.11: Contour plots of the axial velocity field in a plane cutting one blade for case 21.

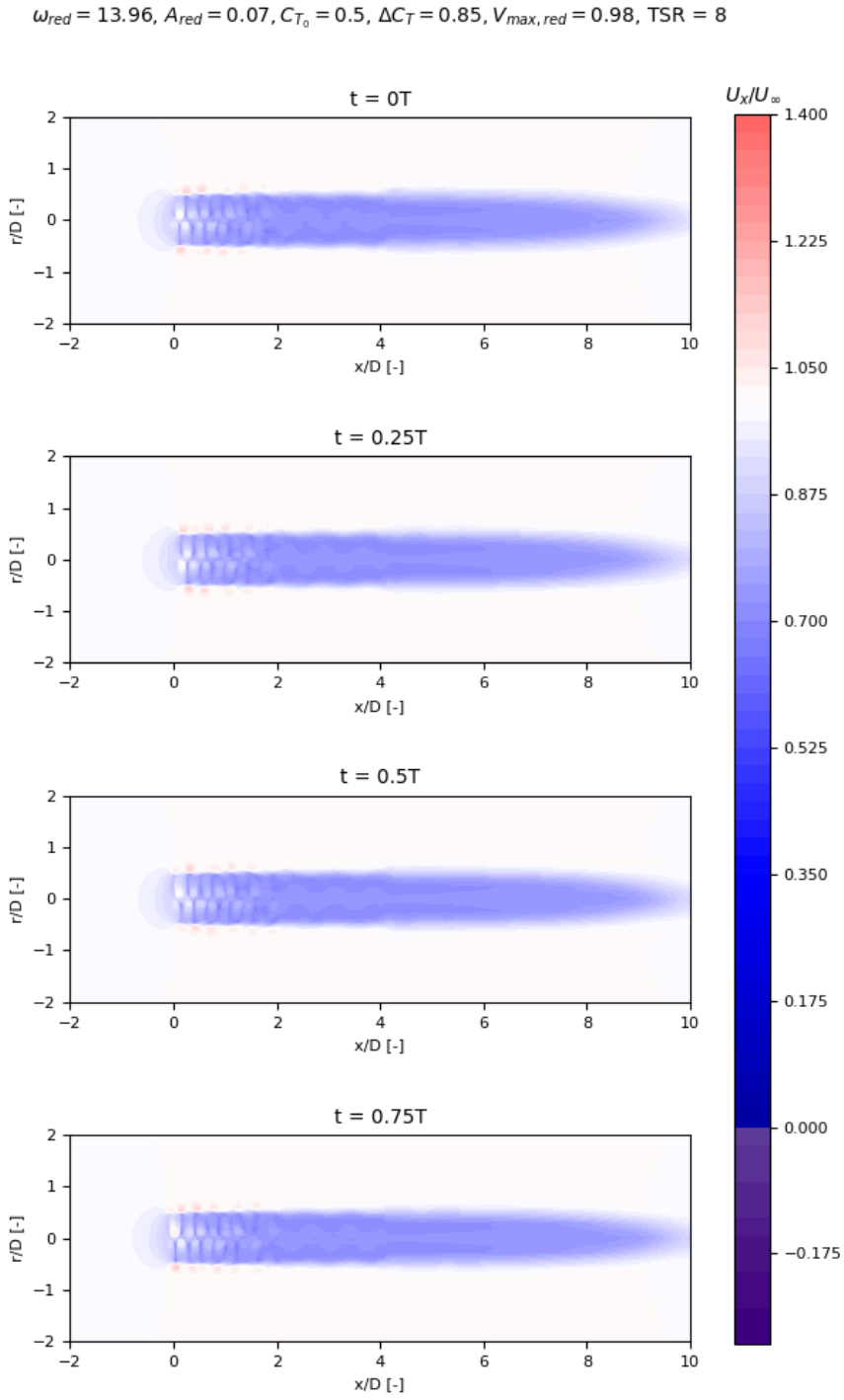

Figure 5.12: Contour plots of the axial velocity field in a plane cutting one blade for case 24.

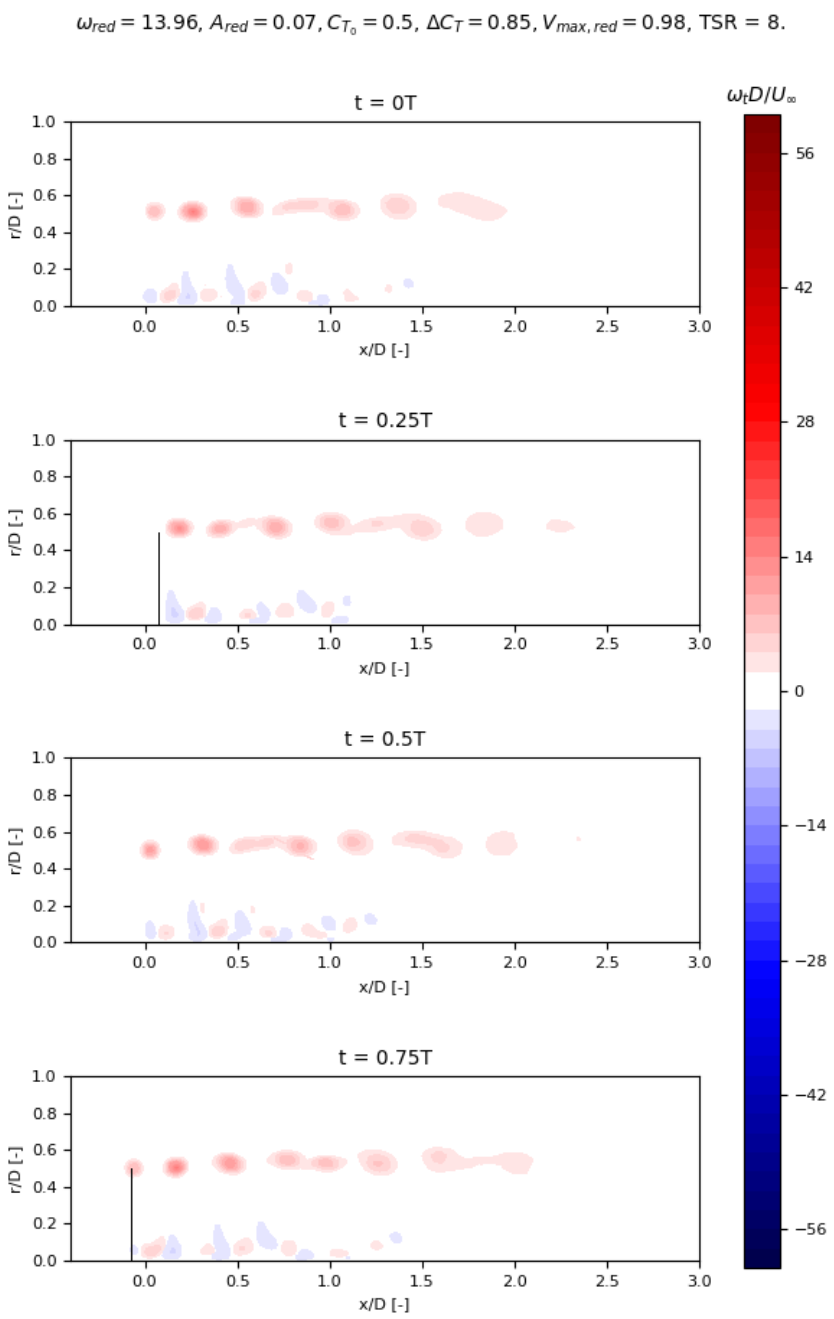

Figure 5.13: Contour plots of the tangential vorticity field in a plane cutting one blade for case 24.

6

Conclusions and recommendations

During this project, the induction field of a surging wind turbine was studied. To do so, a CFD actuator disc model and a CFD actuator line model were developed. The setup and validation processes of these models were described in chapter 3. In the same chapter, a brief description of the dynamic inflow model developed by Carlos Ferreira [15] was given. Next, the models were used to run a range of case studies. The results of the the actuator disc model and actuator line model simulations were commented respectively in chapter 4 and 5. The obtained induction factors were compared to those resulting from the dynamic inflow model and the contour plots of the velocity, vorticity and pressure fields were analyzed.

The conclusions that can be driven from this work are given in section 6.1 of this chapter. To conclude this report, some recommendations for future work in the research area of this project are given in section 6.2.

6.1. Conclusions

The first objective achieved by this project was the creation of an actuator disc model and of an actuator line model in OpenFOAM for the simulation of a surging wind turbine. Both models allow the imposition of a certain thrust coefficient and form a flexible tool for the study of the aerodynamics of floating wind turbines.

The literature review conducted for this project gave a clear picture of the amplitudes of the thrust coefficient variations ΔC_T, baseline thrust coefficients C_{T0}, reduced frequencies ω_{red}, reduced amplitudes A_{red} and reduced maximum velocities of the surge motion $V_{max,red}$ investigated in literature. Furthermore, the linear relationship between ΔC_T and $V_{max,red}$ has been highlighted in figure 2.13.

The knowledge acquired during the literature review and the developed models were used to answer the research questions presented in section 1.3:

1. *What is the impact of platform surge motion on the induction field of a horizontal-axis wind turbine?*

   The impact of surge motion on the induction field of a horizontal-axis wind turbine was analyzed with the actuator disc model for a range of case studies. At first, the effects of the trust coefficient variations and of the disc movement were separated. It was seen that the thrust coefficients variations cause oscillations in the induction factor with an amplitude that decreases and a phase shift with respect to the loading that increases when the frequency increases. The change in position of the disc causes loading oscillations with an amplitude that increases at higher frequencies and a phase that shifts towards a 90°phase shift with respect to the motion velocity. When the two oscillations are combined, they are out of phase and partially cancel each other out. This means that in cases where the amplitude of the thrust coefficient variations is proportional to the maximum velocity of the surge motion, as expected for real wind turbines, there are only minimal induction factor variations over the motion period. These results are in accordance with those presented in [15]. Overall, the values of induction factor and the contour plots of the velocity, vorticity and pressure fields show that the streamtube enters turbulent wake state only when a high thrust coefficient is reached at low frequencies, while propeller state is only entered when a

negative thrust coefficient is reached at low frequencies. In these cases, the flow has the time to adapt to the loading conditions. In real wind turbines, however, the thrust coefficient variations are related to the motion velocity and it is expected that the frequency will be high enough to maintain the streamtube in windmill state in most cases. Furthermore, no evidence of vortex ring state was found in any of the simulated cases.

2. *Can a dynamic inflow model accurately predict this induction field?*

   The comparison between the results of the actuator disc simulations and those obtained with the dynamic inflow model by Carlos Ferreira presented in [15] has shown good agreement between the disc average induction factors. The agreement is better if the induction at $r/R = 0$ is considered for the actuator disc model. This gives confidence in the possibility of using momentum methods for the aerodynamic analysis of floating wind turbines.

3. *What is the effect of the finite number of blades on this induction field?*

   The study of the effect of the finite number of blades was only initiated during the current project, using the actuator line model. The resulting disc average induction factors present excellent agreement with those obtained with the actuator disc model, as do those at $r/R = 0.9$, while the induction at the rotor center is lower. The effect of the finite number of blades is more evident in cases with higher motion frequencies than at lower motion frequencies, with areas of lower axial velocity and areas of higher axial velocities that alternate in the wake with the frequency of the rotation of the blades. Nevertheless, the conclusions drawn from the results of the actuator disc model on the wake states entered by the streamtube remain valid. It should be noted that only one tip speed ratio and one basline thrust coefficient were thoroughly tested during this study, thus these conclusions may not apply in different conditions.

6.2. Recommendations

This thesis forms the basis for more accurate research on the induction field of floating horizontal-axis wind turbines. Several approaches could be tried to expand the present work.

An improvement to the actuator disc model could be made by reducing the discrepancy between its resulting induction factor and that predicted by momentum theory with Glauert's correction at high thrust coefficients. The model could then be used to validate other dynamic inflow models. In particular, the development of a dynamic inflow model capable of predicting the induction at different radial locations would be beneficial, since currently the results of the dynamic inflow model are in better agreement with those of the CFD actuator disc model if the induction at the disc center is considered instead of the disc average induction factor. Furthermore, the model could easily be modified to account for other types of platform motions, besides surge motion. As pitch motion is expected to significantly influence the aerodynamics of FOWTs, being a motion in the axial direction that also introduces an effective wind shear across the rotor disc, it would be particularly interesting to test its effects.

The actuator line model presented in this work is an initial step in the process of simulating the floating wind turbine in a more realistic way. First, the accuracy of the model should be improved, particularly at high thrust coefficients. This could be achieved with a more accurate validation, including an analysis of the influence of domain size and number of blade elements on the solution. Next, it is advised to further test the model in conditions of different tip speed ratios and for rotors with different numbers of blades to fully understand the influence of the finite number of blades on the flow field. Different types of actuator line models may then be implemented. An actuator line model of a Joukowsky rotor, presenting a constant circulation along the blades, would allow imposing a certain thrust coefficient while also studying the effect of the tangential forces on the wake. The thrust coefficient would depend on the induction, which would make the simulations more iterative. For an example of a model of this type, see [27]. Next, the model of a full rotor in which the forces are not imposed but calculated with airfoil data could be implemented by adding the possibility of moving the platform to the *turbinesFoam* code. The oscillating values of the thrust coefficient and power coefficient would then become outputs of the simulations and the results could be compared to those obtained with BEM codes. The hub and the tower could also be modelled with *turbinesFoam*. An obstacle to this approach is the validation of such model, since it should be validated with data from full-scale experiments on FOWTs, which is scarcely available at the moment. Alternatively, data from full CFD simulations could be used.

A

Additional results of the unsteady actuator disc simulations

A.1. Case 1

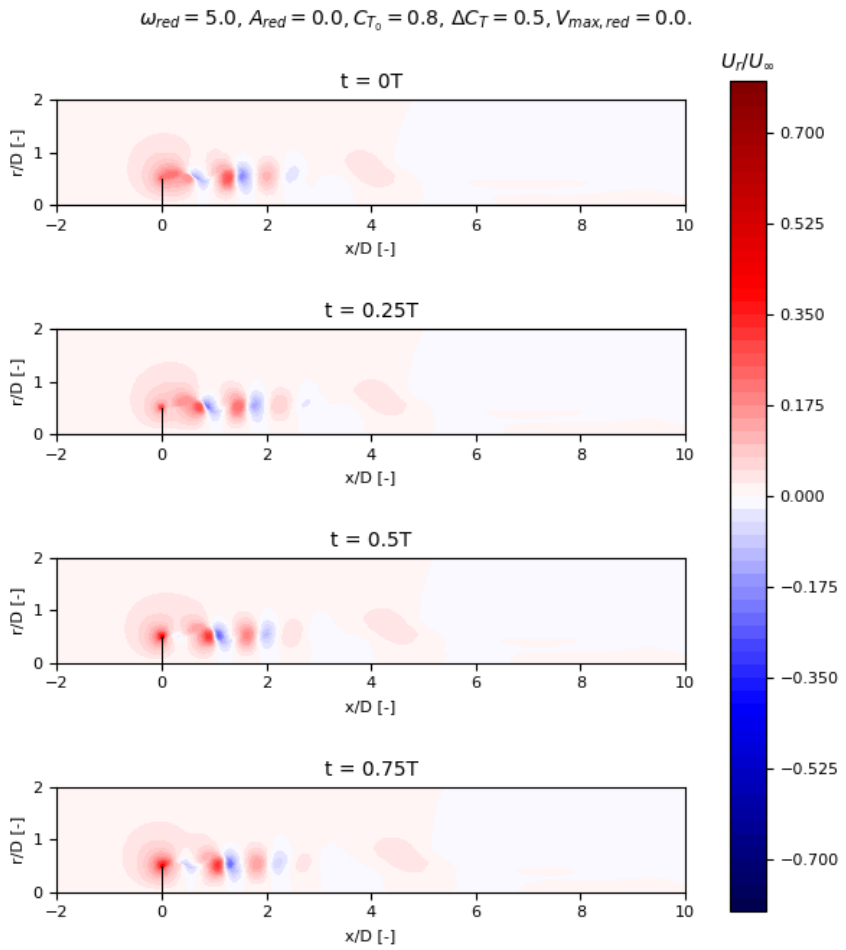

Figure A.1: Contour plots of the radial velocity field around the actuator disc for case 1.

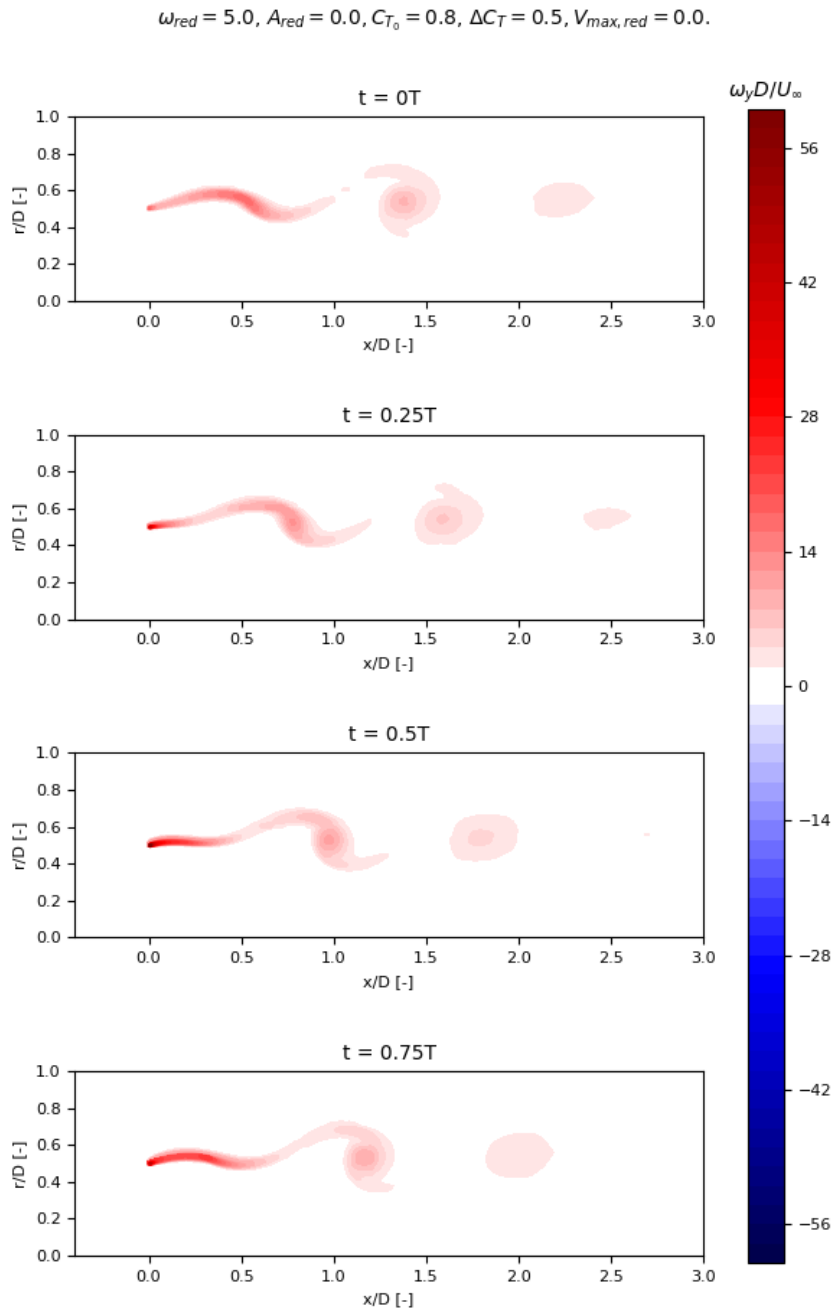

Figure A.2: Contour plots of the vorticity field around the actuator disc for case 1.

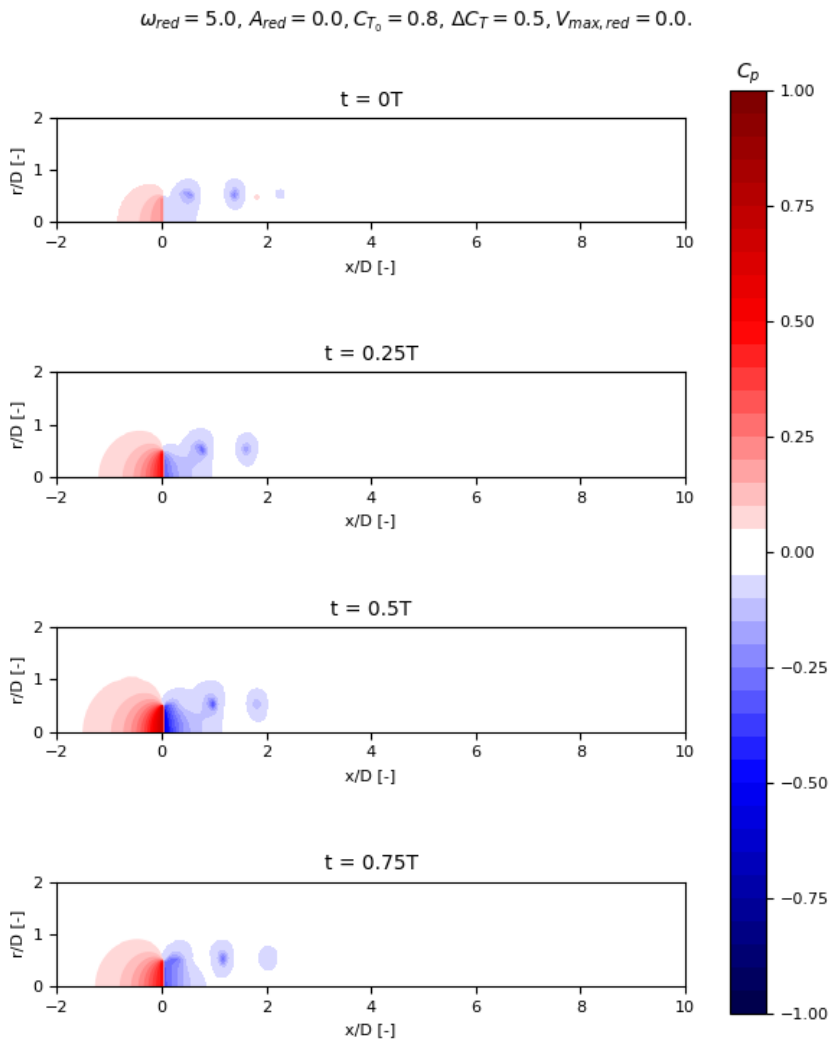

Figure A.3: Contour plots of the pressure field around the actuator disc for case 1.

A.2. Case 12

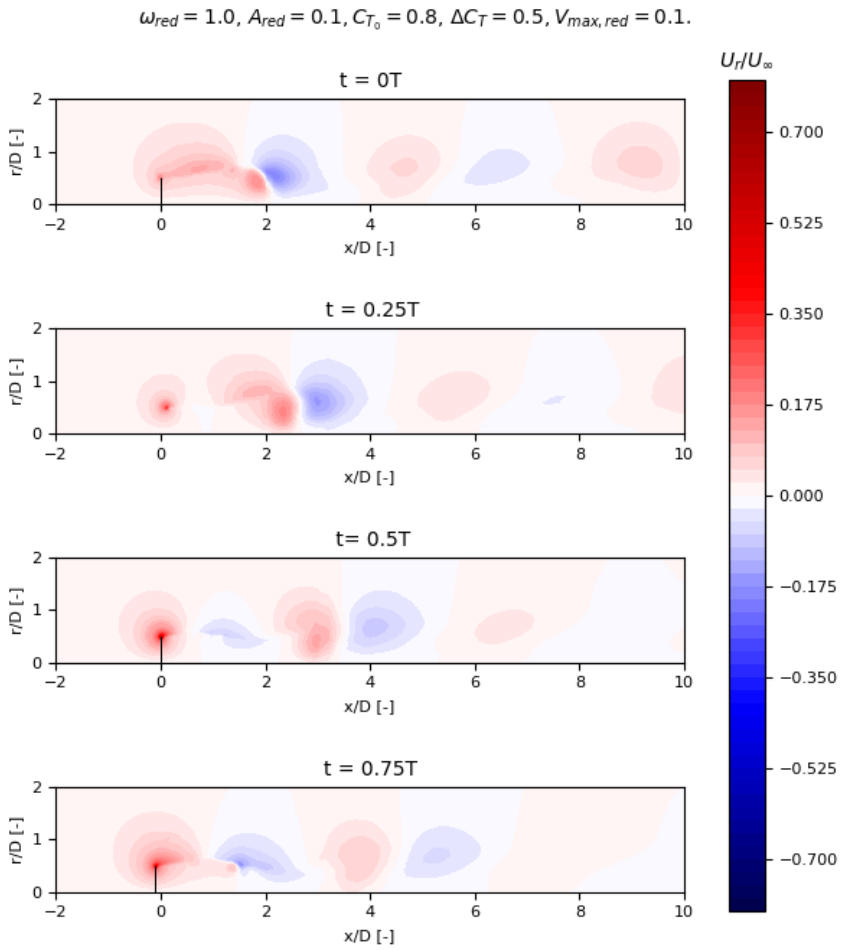

Figure A.4: Contour plots of the radial velocity field around the actuator disc for case 12.

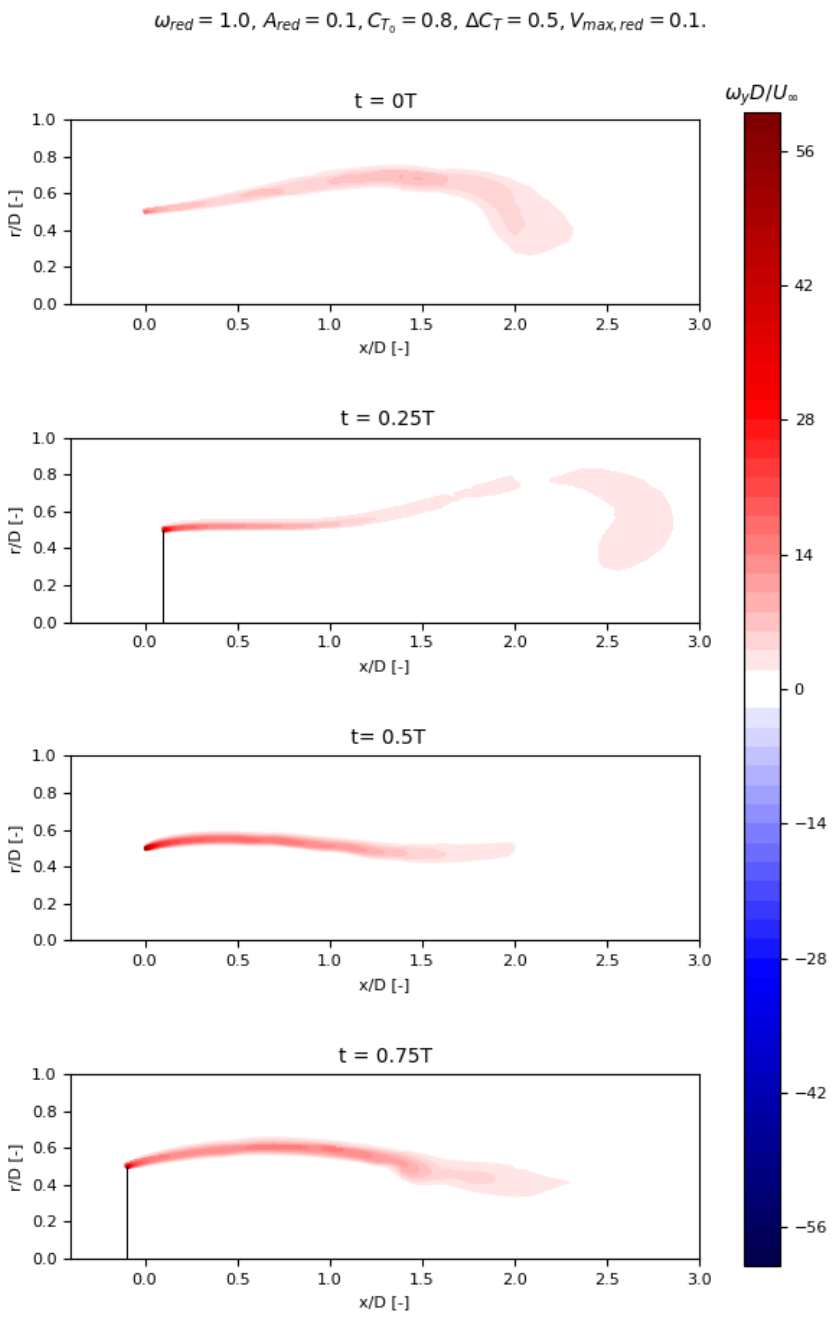

Figure A.5: Contour plots of the vorticity field around the actuator disc for case 12.

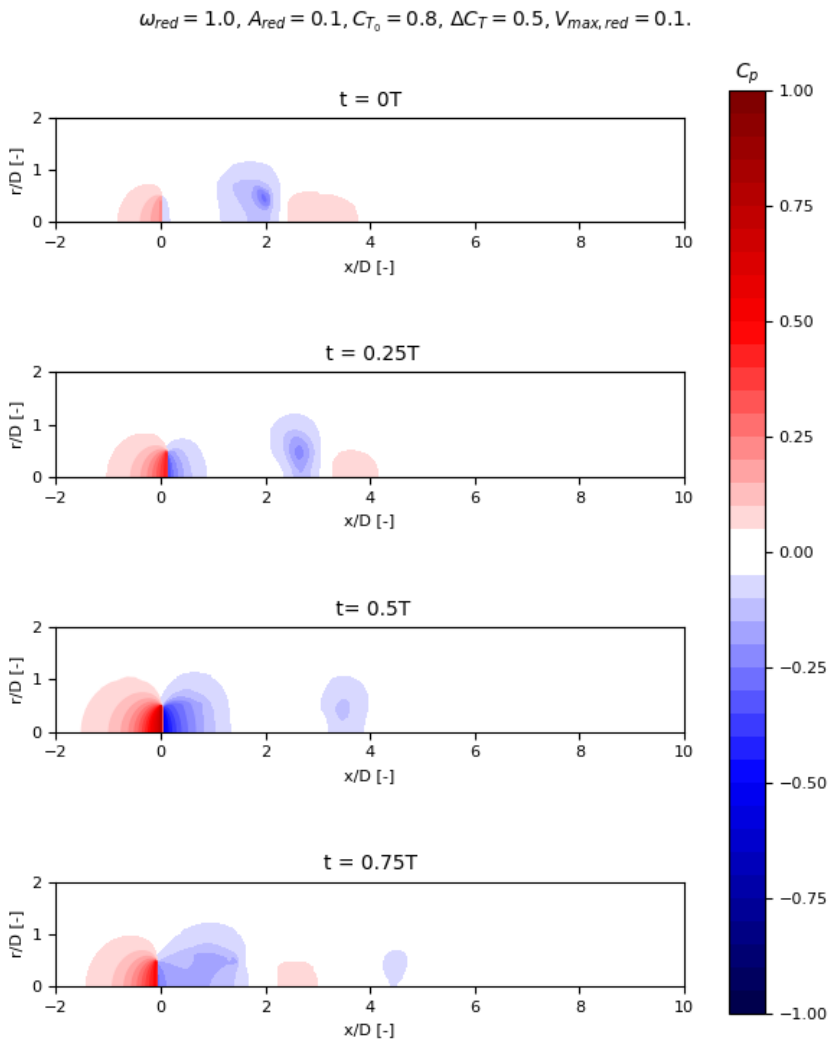

Figure A.6: Contour plots of the pressure field around the actuator disc for case 12.

A.3. Case 13

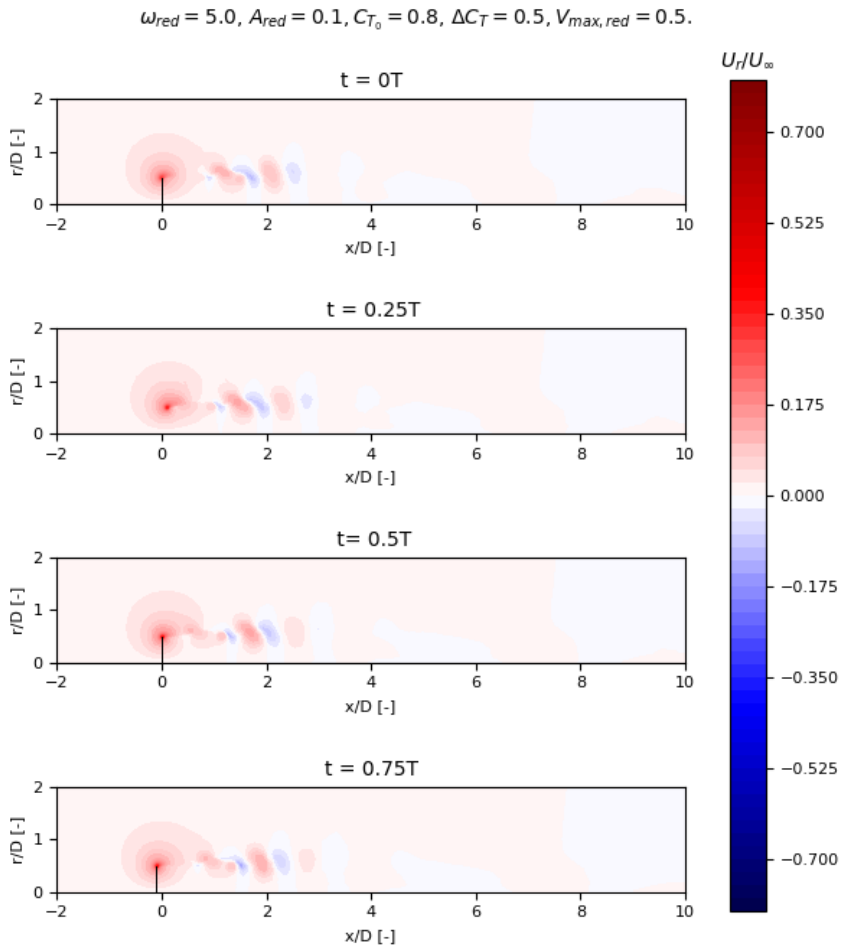

Figure A.7: Contour plots of the radial velocity field around the actuator disc for case 13.

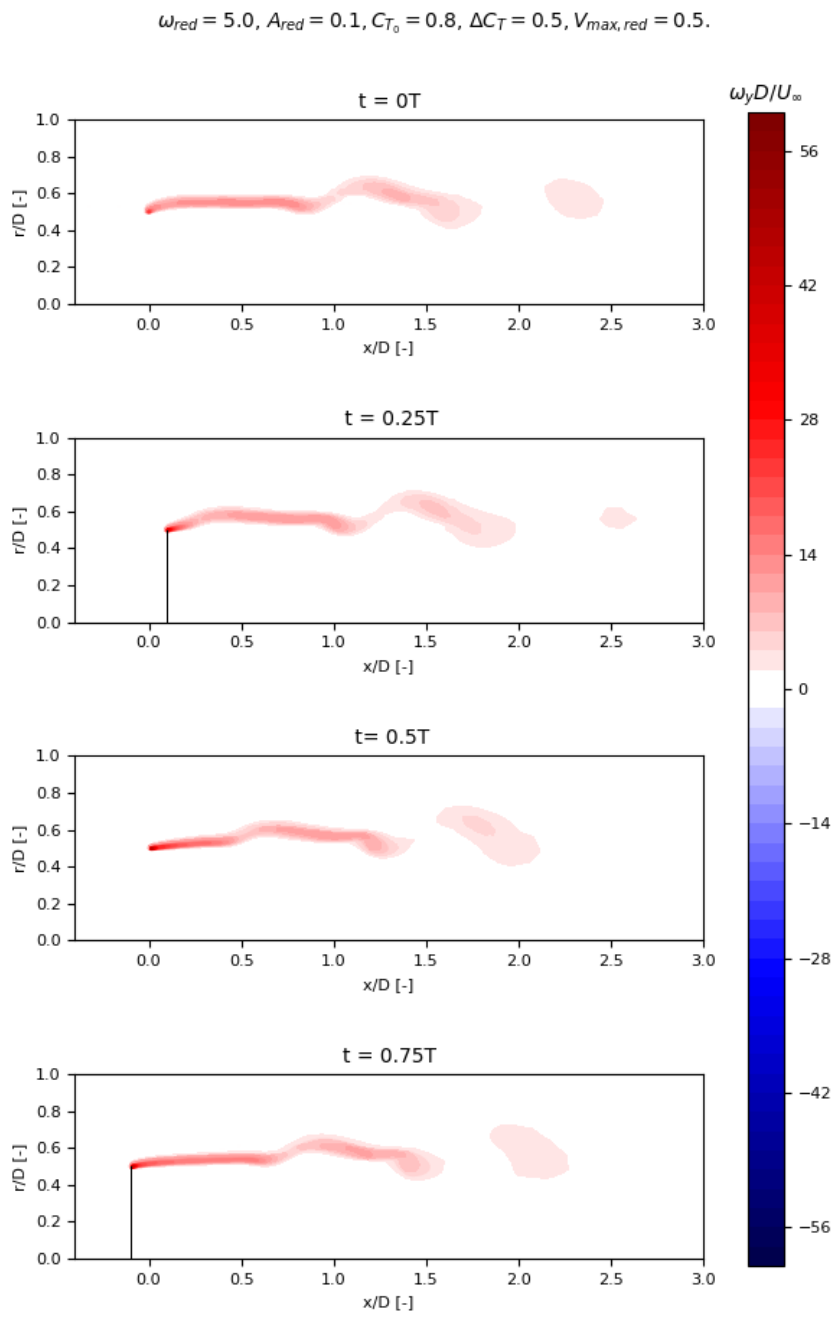

Figure A.8: Contour plots of the vorticity field around the actuator disc for case 13.

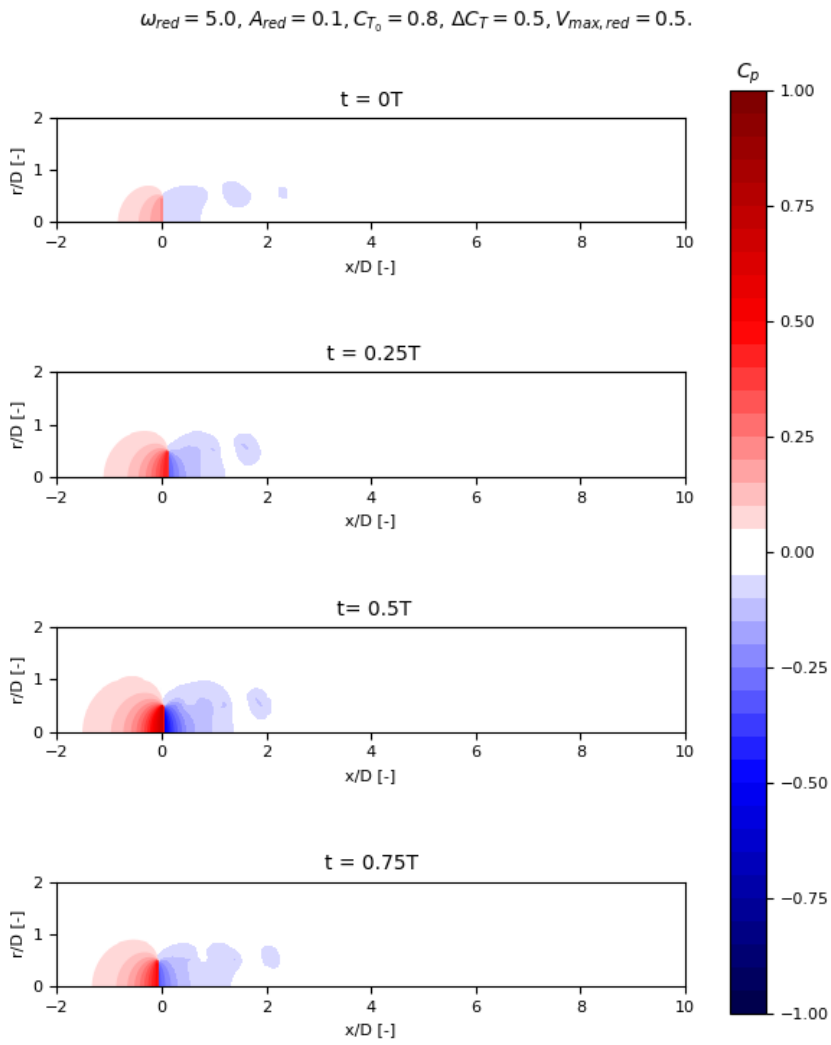

Figure A.9: Contour plots of the pressure field around the actuator disc for case 13.

A.4. Case 22

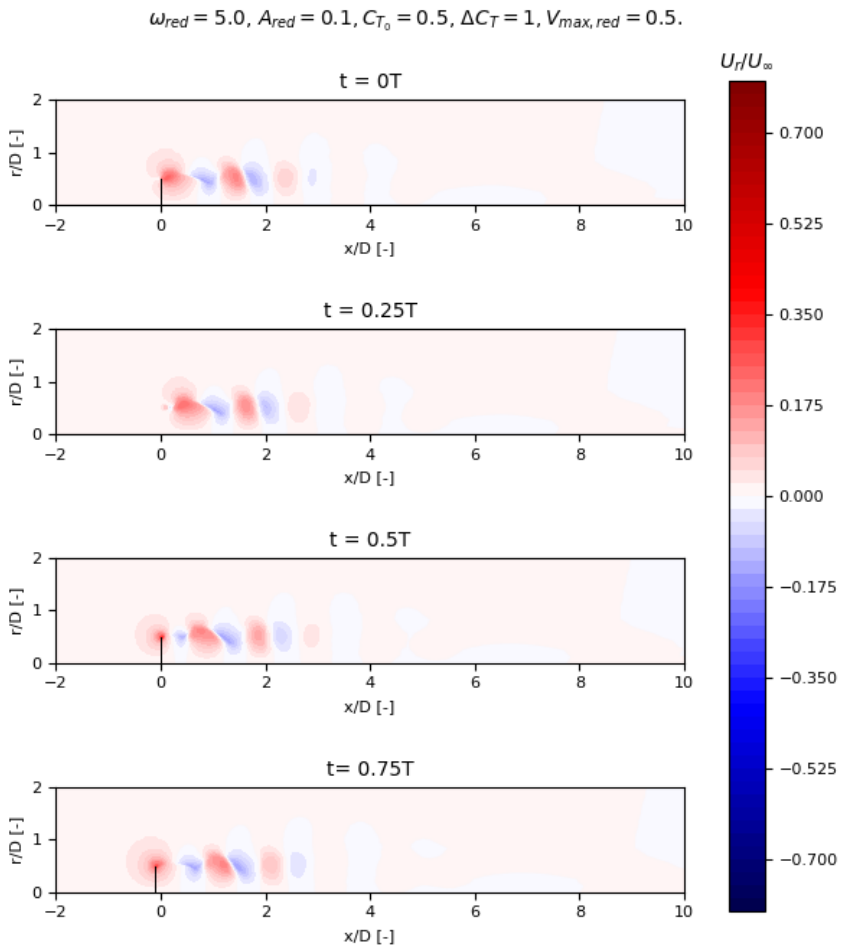

Figure A.10: Contour plots of the radial velocity field around the actuator disc for case 22.

A.5. Case 24

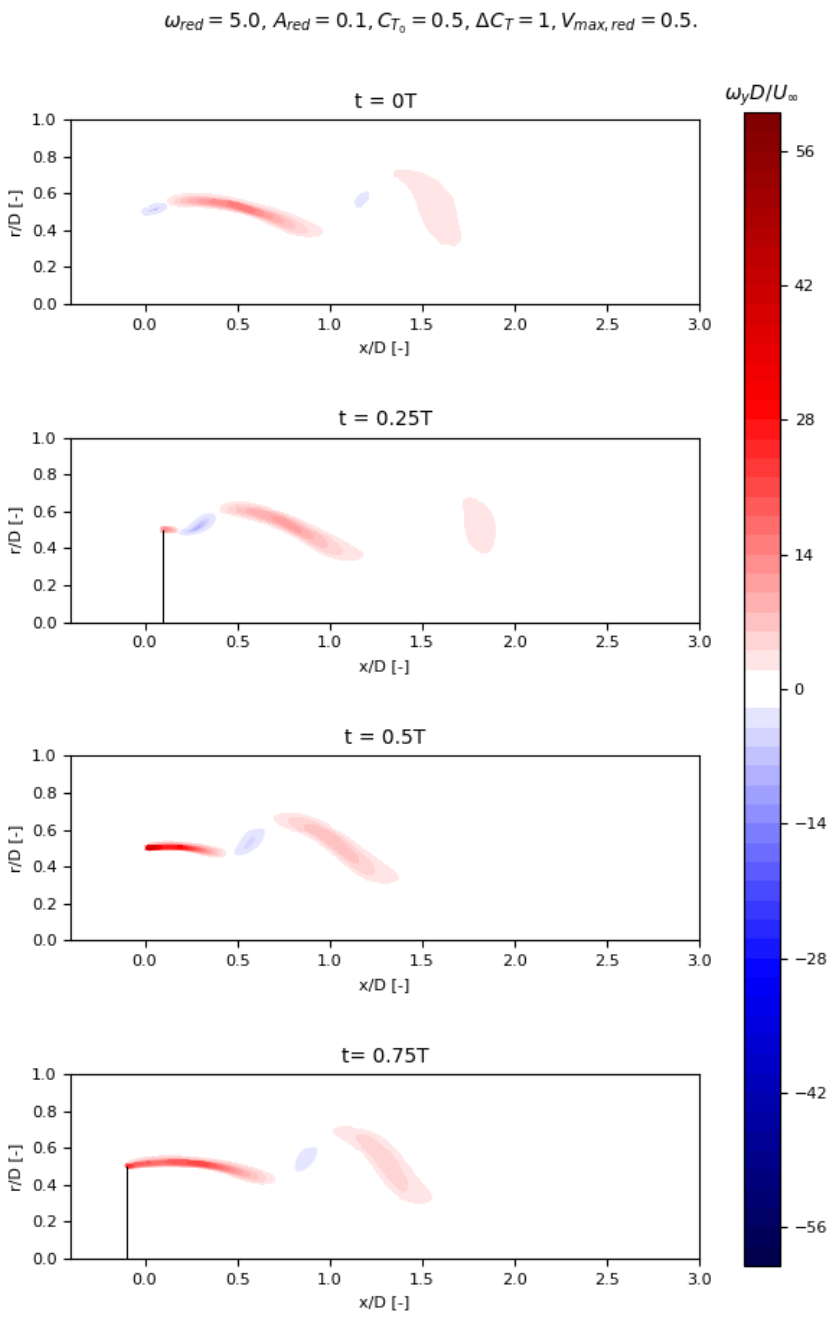

Figure A.11: Contour plots of the vorticity field around the actuator disc for case 22.

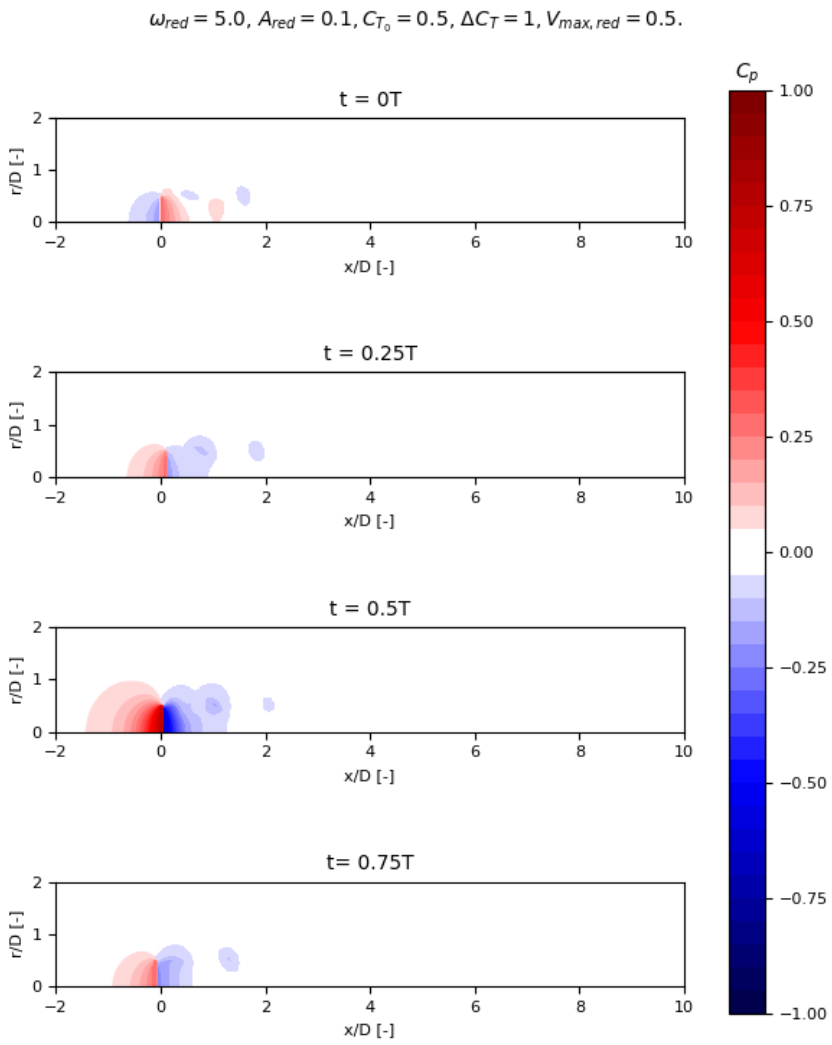

Figure A.12: Contour plots of the pressure field around the actuator disc for case 22.

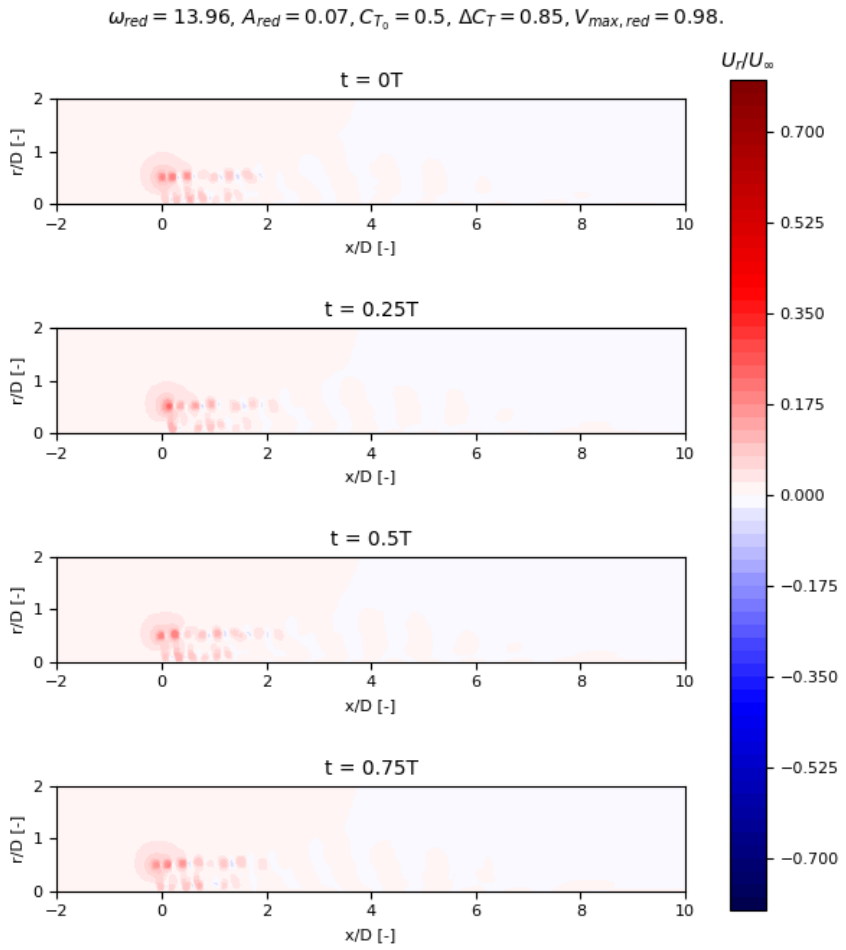

Figure A.13: Contour plots of the radial velocity field around the actuator disc for case 24.

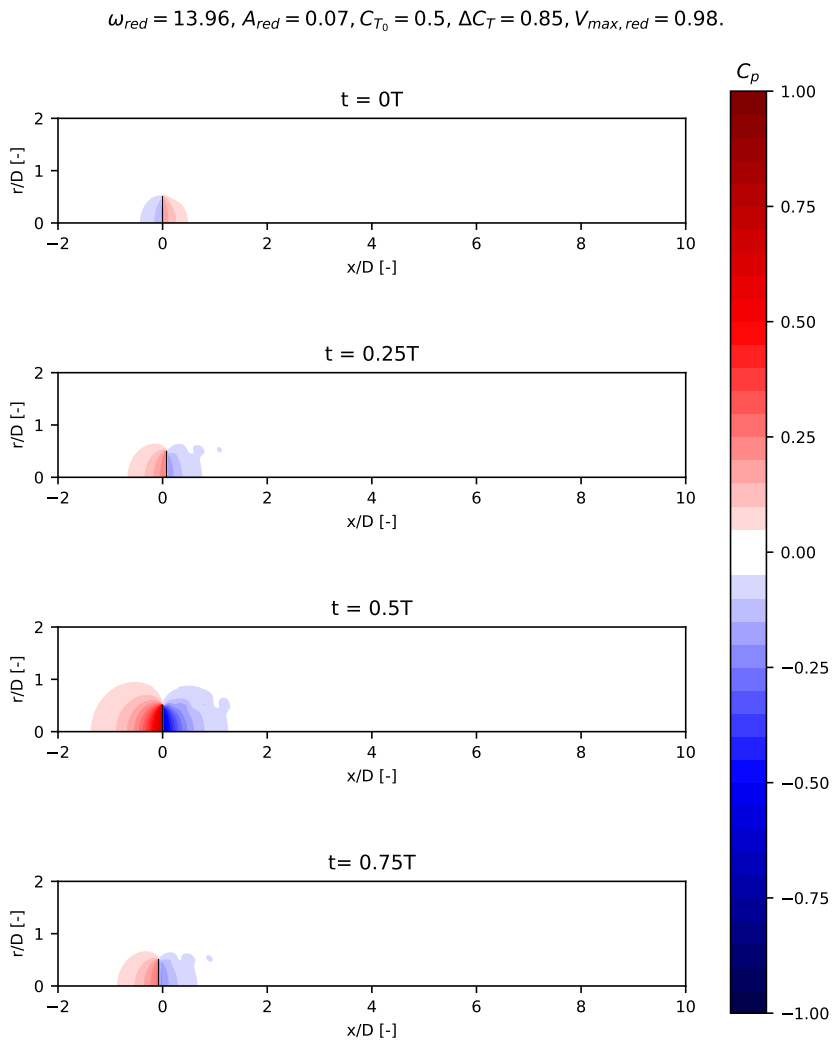

Figure A.14: Contour plots of the pressure field around the actuator disc for case 24.

B

Additional results of the unsteady actuator line simulations

B.1. Case 21

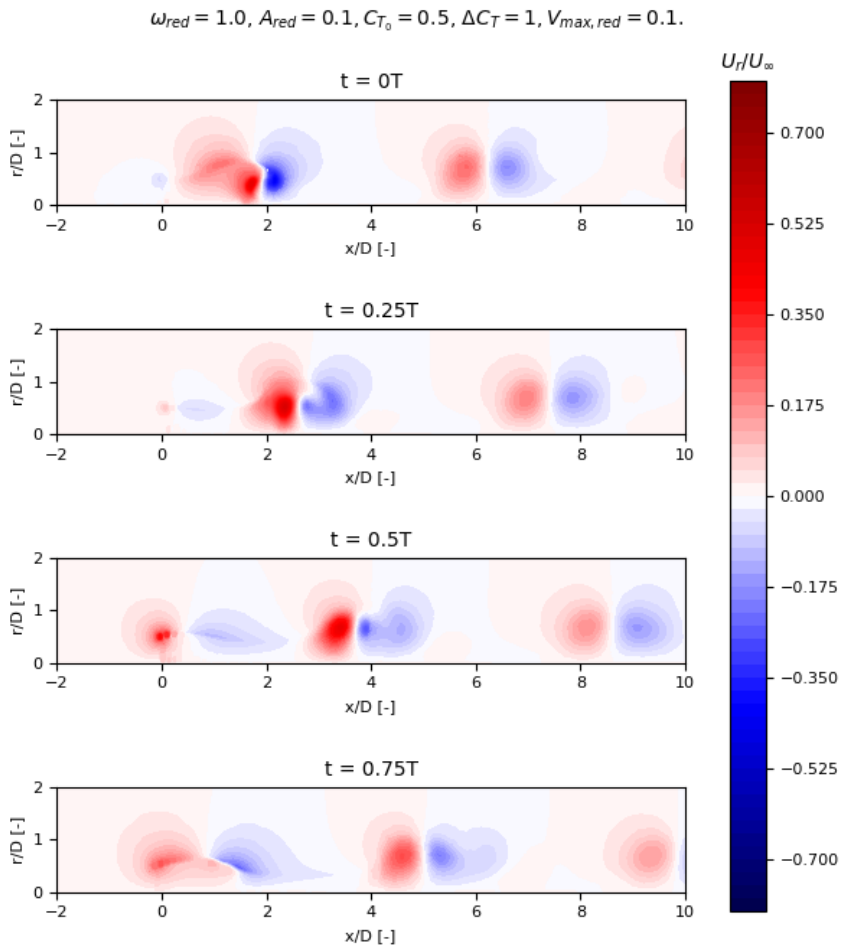

Figure B.1: Contour plots of the radial velocity field in a plane cutting one blade for case 21.

B.2. Case 24

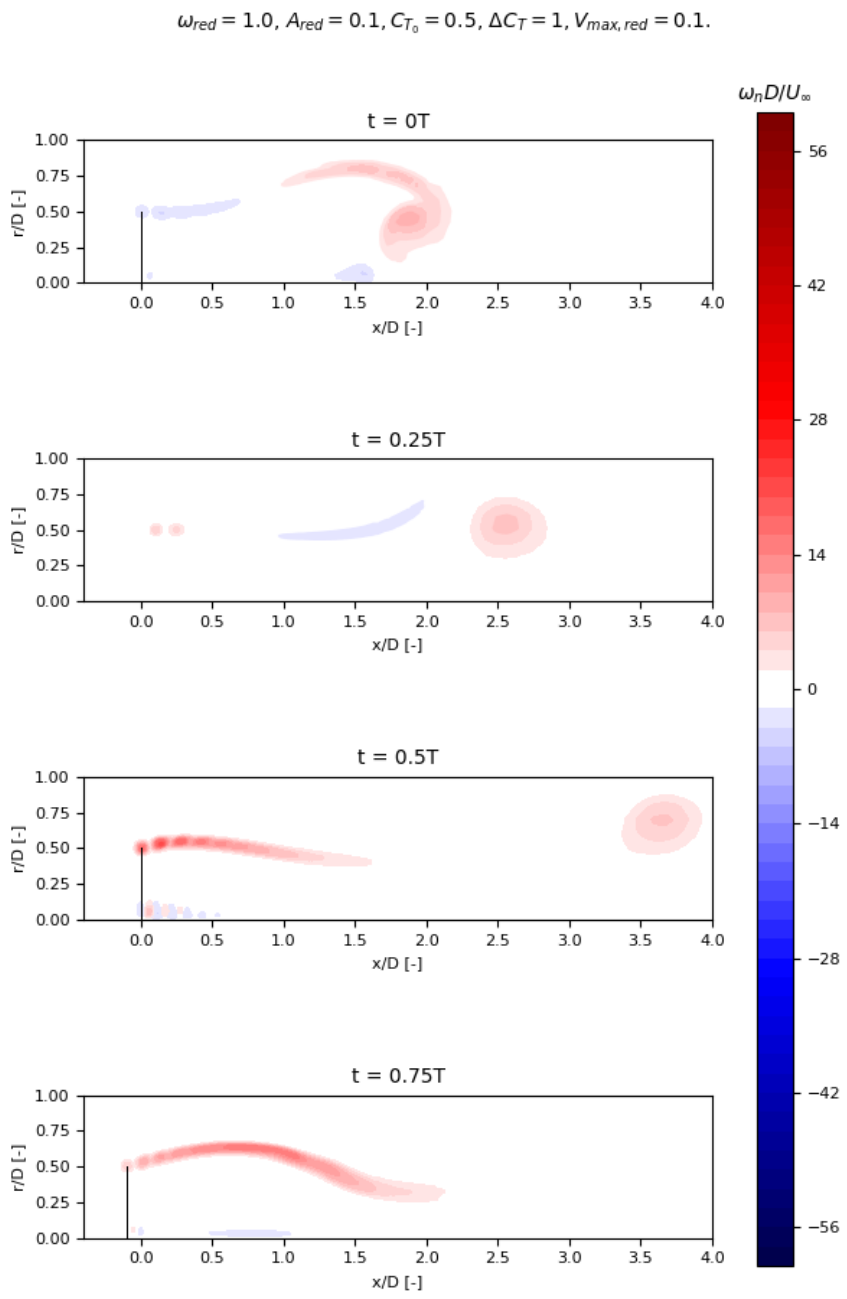

Figure B.2: Contour plots of the vorticity field in a plane cutting a blade for case 21.

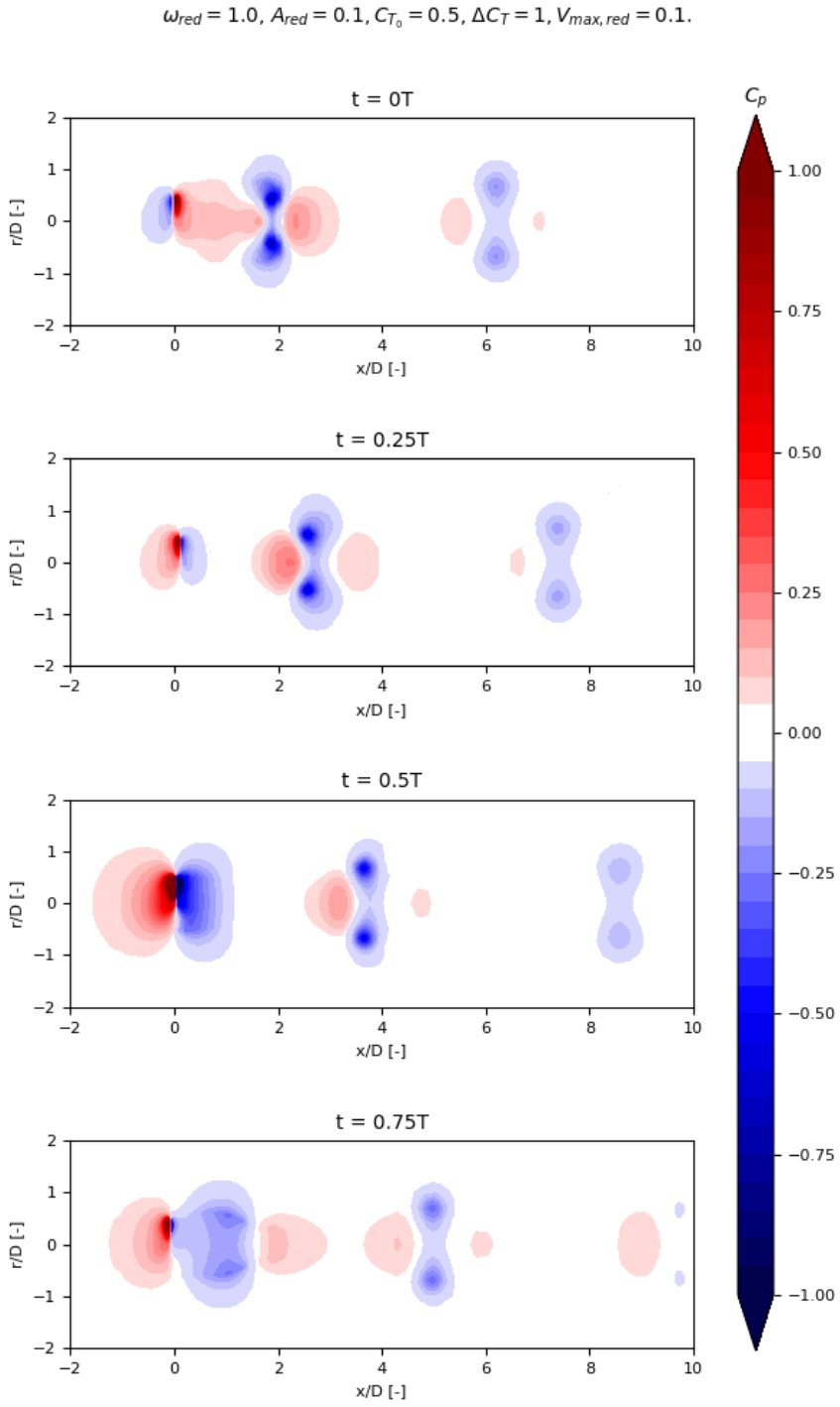

Figure B.3: Contour plots of the pressure field in a plane cutting a blade for case 21.

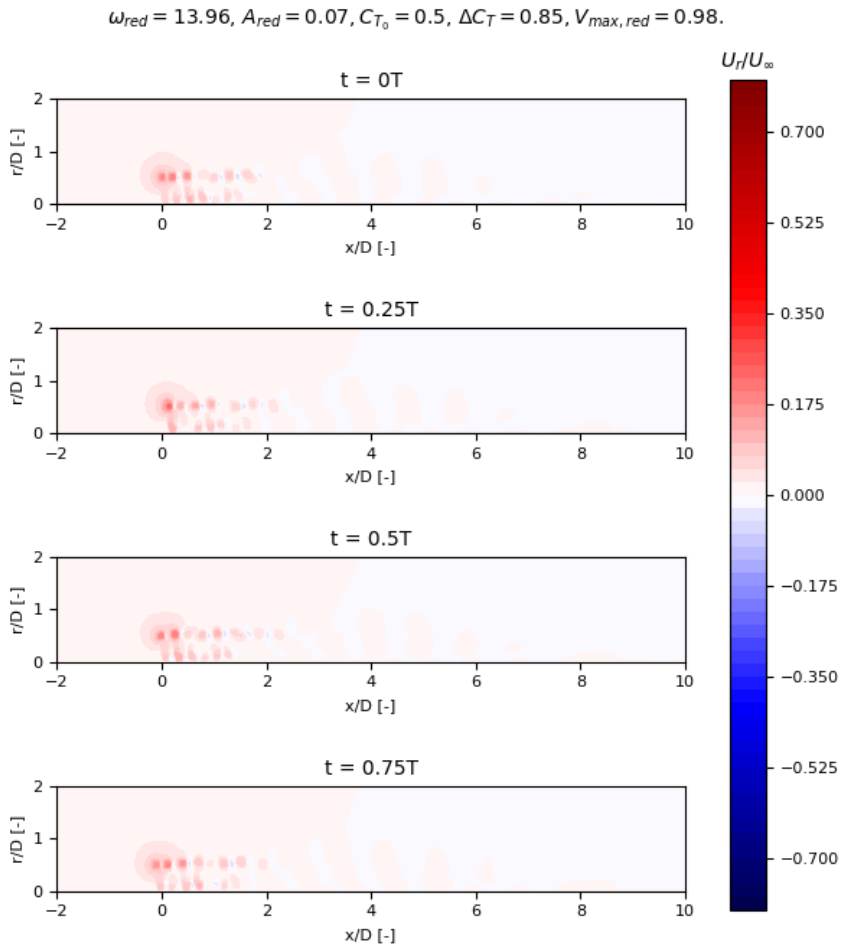

Figure B.4: Contour plots of the radial velocity field in a plane cutting one blade for case 24.

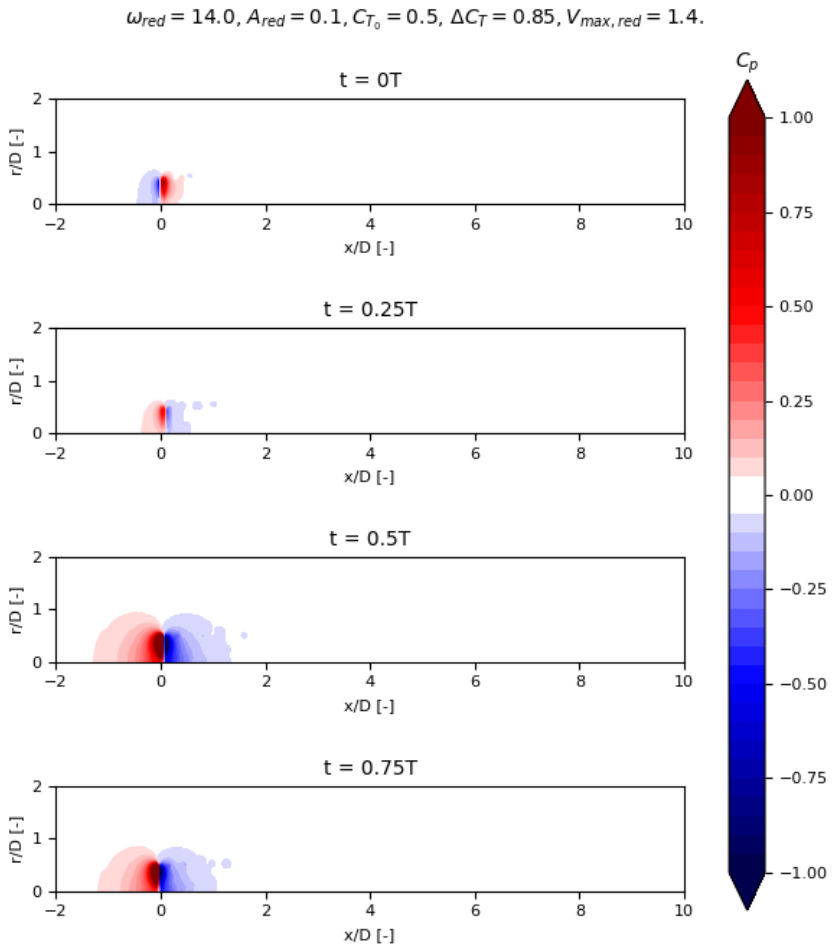

Figure B.5: Contour plots of the pressure field in a plane cutting a blade for case 24.

C

Code for actuator disc simulations with OpenFOAM

In this appendix, the code used for the actuator disc simulations is OpenFOAM is given. As explained in section 3.1, this code can be used to create a *movingActuatorDisc* class, derived from the *actuationDiskSource* already present in OpenFOAM. In section C.1, the file *movingActuatorDisc.H* is reported. This file contains the class declarations. Next, the two source files *movingActuatorDisc.C* and *movingActuatorDiscTemplates.C* are included in sections C.2 and C.3. These three files together form the source code of the *movingActuatorDisc* class. For further information on compilation of OpenFOAM source code, see [18]. Finally, an example of the *fvOptions* file containing the inputs for the creation of a surging actuator disc is given in section C.4.

C.1. movingActuatorDisc.H

```
/*---------------------------------------------------------------------------*\
  =========                 |
  \\      /  F ield         | OpenFOAM: The Open Source CFD Toolbox
   \\    /   O peration     |
    \\  /    A nd           | www.openfoam.com
     \\/     M anipulation  |
-------------------------------------------------------------------------------
    Copyright (C) 2011-2017 OpenFOAM Foundation
    Copyright (C) 2020 ENERCON GmbH
    Copyright (C) 2020 OpenCFD Ltd.
-------------------------------------------------------------------------------
License
    This file is part of OpenFOAM.

    OpenFOAM is free software: you can redistribute it and/or modify it
    under the terms of the GNU General Public License as published by
    the Free Software Foundation, either version 3 of the License, or
    (at your option) any later version.

    OpenFOAM is distributed in the hope that it will be useful, but WITHOUT
    ANY WARRANTY; without even the implied warranty of MERCHANTABILITY or
    FITNESS FOR A PARTICULAR PURPOSE.  See the GNU General Public License
    for more details.

    You should have received a copy of the GNU General Public License
    along with OpenFOAM.  If not, see <http://www.gnu.org/licenses/>.
```

```
Class
    Foam::fv::movingActuatorDisc

Group
    grpFvOptionsSources

Description
    Applies sources on velocity, i.e. \c U, to enable actuator disk models
    for aero/hydro thrust loading of horizontal axis turbines on surrounding
    flow field in terms of energy conversion processes.

    Available options for force computations:
    \verbatim
      Froude          | Froude's one-dimensional ideal actuator disk method
      variableScaling | Variable-scaling actuator disk method
    \endverbatim

    The expressions for \c Froude method:
    \f[
        T = 2 \rho A | \vec{U_o} \cdot \vec{n} |^2 a (1-a)
    \f]
    with
    \f[
        a = 1 - \frac{C_p}{C_T}
    \f]
    where
    \vartable
      T         | Thrust magnitude
      \rho      | Monitored incoming fluid density
      A         | Actuator disk planar surface area
      \vec{U_o} | Incoming velocity spatial-averaged on monitored region
      \vec{n}   | Surface-normal vector of the actuator disk pointing upstream
      a         | Axial induction factor
      C_p       | Power coefficient
      C_T       | Thrust coefficient
    \endvartable

    The expressions for \c variableScaling method:
    \f[
        T = 0.5 \rho A | \vec{U_m} \cdot \vec{n} |^2 C_T^*
    \f]
    with
    \f[
        C_T^* = C_T \left( \frac{ |\vec{U_{ref}}| }{ |\vec{U_m}| } \right)^2
    \f]
    where
    \vartable
        T         | Thrust magnitude
        \rho      | Monitored incoming fluid density
        A         | Actuator disk planar surface area
        \vec{U_m} | Incoming velocity spatial-averaged on actuator disk
        \vec{n}   | Surface-normal vector of the actuator disk pointing upstream
        \vec{U_{ref}} | Incoming velocity spatial-averaged on monitored region
        C_T       | Thrust coefficient
        C_T^*     | Calibrated thrust coefficient
```

```
    \endvartable

    Reference
    \verbatim
        Froude's one-dimensional ideal actuator disk (tags:F,BJSB):
            Froude, R. E. (1889).
            On the part played in propulsion by differences of fluid pressure.
            Trans. Inst. Naval Architects, 30, 390.

            Burton, T., Jenkins, N., Sharpe, D., & Bossanyi, E. (2011).
            Wind energy handbook, 2nd edition.
            Chichester, the United Kingdom. John Wiley & Sons.
            Print ISBN:978-0-470-69975-1
            DOI:10.1002/9781119992714

        Variable-scaling method (tags:LSRMKT,LS):
            van der Laan, M. P., Sørensen, N. N., Réthoré, P. E.,
            Mann, J., Kelly, M. C., & Troldborg, N. (2015).
            The □ε□kfP model applied to double wind turbine
            wakes using different actuator disk force methods.
            Wind Energy, 18(12), 2223-2240.
            DOI:10.1002/we.1816

            van der Laan, M. P., Sørensen, N. N., Réthoré, P. E., Mann, J.,
            Kelly, M. C., Troldborg, N., Hansen, K. S., & Murcia, J. P. (2015).
            The □ε□kfP model applied to wind farms.
            Wind Energy, 18(12), 2065-2084.
            DOI:10.1002/we.1804
    \endverbatim

    Corrections applied to:
    \verbatim
      U          | Velocity     [m/s]
    \endverbatim

    Required fields:
    \verbatim
      U          | Velocity     [m/s]
    \endverbatim

Usage
    Example by using \c constant/fvOptions:
    \verbatim
    movingActuatorDisc1
    {
        // Mandatory entries (unmodifiable)
        type            movingActuatorDisc;

        // Mandatory (inherited) entries (unmodifiable)
        selectionMode   <mode>;     // e.g. cellSet as shown below
        cellSet         <cellSetName>;

        // Mandatory entries (runtime modifiable)
        diskArea        40.0;
        diskDir         (1 0 0);
        Cp              <Function1>;
```

```
    Ct              <Function1>;

    // Conditional optional entries (unmodifiable)
    monitorMethod   <points|cellSet>;
    monitorCoeffs
    {
        // Option-1
        points
        (
            (p1x p1y p1z)
            (p2x p2y p2z)
            ...
        );

        // Option-2
        cellSet     <monitorCellSet>;
    }

    // Optional entries (unmodifiable)
    variant         <forceMethod>;

    // Optional entries (runtime modifiable)
    sink            true;
    writeFileStart  0;
    writeFileEnd    100;

    // Optional (inherited) entries
    ...
}
\endverbatim

where the entries mean:
\table
  Property   | Description                          | Type | Req'd    | Dflt
  type       | Type name: movingActuatorDisc        | word | yes      | -
  diskArea   | Actuator disk planar surface area    | scalar | yes | -
  diskDir    | Surface-normal vector of the actuator disk <!--
             --> pointing upstream                  | vector   | yes | -
  Cp         | Power coefficient                    | Function1 | yes | -
  Ct         | Thrust coefficient                   | Function1 | yes | -
  monitorMethod | Type of incoming velocity monitoring method   <!--
             -->    - see below                    | word | no  | points
  variant    | Type of the force computation method - see below <!--
             -->                                   | word | no  | Froude
  sink         | Flag for body forces to act as a source (true)  <!--
             -->  or a sink (false)                | bool   | no  | true
  writeFileStart | Start time for file output      | scalar | no  | 0
  writeFileEnd   | End time for file output        | scalar | no  | VGREAT
\endtable

The inherited entries are elaborated in:
  - \link fvOption.H \endlink
  - \link cellSetOption.H \endlink
  - \link writeFile.H \endlink
  - \link Function1.H \endlink
```

```
    Options for the \c monitorMethod entry:
    \verbatim
      points  | Monitor incoming velocity field at a given set of points
      cellSet | Monitor incoming velocity field at a given cellSet
    \endverbatim

    Options for the \c variant entry:
    \verbatim
      Froude          | Froude's one-dimensional ideal actuator disk method
      variableScaling | Variable-scaling actuator disk method
    \endverbatim

SourceFiles
    movingActuatorDisc.C
    movingActuatorDiscTemplates.C

\*---------------------------------------------------------------------------*/

#ifndef movingActuatorDisc_H
#define movingActuatorDisc_H

#include "cellSetOption.H"
#include "writeFile.H"
#include "Function1.H"

// * * * * * * * * * * * * * * * * * * * * * * * * * * * * * * * * * * * * * //

namespace Foam
{
namespace fv
{

/*---------------------------------------------------------------------------*\
                    Class movingActuatorDisc Declaration
\*---------------------------------------------------------------------------*/

class movingActuatorDisc
:
    public cellSetOption,
    public functionObjects::writeFile
{
protected:

    // Protected Enumerations

        //- Options for the force computation method types
        enum forceMethodType
        {
            FROUDE,                 //!< "Froude's ideal actuator disk method"
            VARIABLE_SCALING,       //!< "Variable-scaling actuator disk method"
        };

        //- Names for forceMethodType
        static const Enum<forceMethodType> forceMethodTypeNames;

        //- Options for the incoming velocity monitoring method types
```

```
        enum monitorMethodType
        {
            POINTS,                 //!< "A set of points"
            CELLSET                 //!< "A cellSet"
        };

        //- Names for monitorMethodType
        static const Enum<monitorMethodType> monitorMethodTypeNames;


    // Protected Data

        //- The type of the force computation method
        const enum forceMethodType forceMethod_;

        //- The type of incoming velocity monitoring method
        const enum monitorMethodType monitorMethod_;

        //- Flag for body forces to act as a source (true) or a sink (false)
        label sink_;

        //- Start time for file output
        scalar writeFileStart_;

        //- End time for file output
        scalar writeFileEnd_;

        //- Actuator disk planar surface area [m2]
        scalar diskArea_;

        //- Surface-normal vector of the actuator disk pointing upstream
        vector diskDir_;

        //- Velocity vs power coefficients
        autoPtr<Function1<scalar>> UvsCpPtr_;

        //- Velocity vs thrust coefficients
        autoPtr<Function1<scalar>> UvsCtPtr_;

        //- Set of cells whereat the incoming velocity is monitored
        labelList monitorCells_;

        //- data defined by Arianna
        vector Umon_;
        scalar rhomon_;
        scalar point1x_;
        scalar point2x_;
        scalar point1y_;
        scalar point2y_;
        scalar point1z_;
        scalar point2z_;
        scalar Amplitudex_;
        scalar frequencyx_;
        scalar radius_;
        scalar delta_Ct_;
        scalar phase_Ct_;
```

```
        scalar frequency_Ct_;

        scalar x1;
        scalar x2;

    // Protected Member Functions

        //- Output file header information
        virtual void writeFileHeader(Ostream& os);


private:

    // Private Member Functions

        //- Locate the set of cells whereat the incoming velocity is monitored
        void setMonitorCells(const dictionary& dict);

        //- Compute the selected force computation method type
        template<class AlphaFieldType, class RhoFieldType>
        void calc
        (
            const AlphaFieldType& alpha,
            const RhoFieldType& rho,
            fvMatrix<vector>& eqn
        );

        //- Compute Froude's ideal actuator disk method
        template<class AlphaFieldType, class RhoFieldType>
        void calcFroudeMethod
        (
            const AlphaFieldType& alpha,
            const RhoFieldType& rho,
            fvMatrix<vector>& eqn
        );

        //- Compute variable-scaling actuator disk method
        template<class AlphaFieldType, class RhoFieldType>
        void calcVariableScalingMethod
        (
            const AlphaFieldType& alpha,
            const RhoFieldType& rho,
            fvMatrix<vector>& eqn
        );


public:

    //- Runtime type information
    TypeName("movingActuatorDisc");


    // Constructors

        //- Construct from components
        movingActuatorDisc
```

```
        (
            const word& name,
            const word& modelType,
            const dictionary& dict,
            const fvMesh& mesh
        );

        //- No copy construct
        movingActuatorDisc(const movingActuatorDisc&) = delete;

        //- No copy assignment
        void operator=(const movingActuatorDisc&) = delete;


    //- Destructor
    virtual ~movingActuatorDisc() = default;


    // Member Functions

        // Access

            //- Normal disk direction
            const vector& diskDir() const
            {
                return diskDir_;
            }

            //- Disk area
            scalar diskArea() const
            {
                return diskArea_;
            }


         // Add explicit and implicit contributions

            //- Source term to momentum equation
            virtual void addSup
            (
                fvMatrix<vector>& eqn,
                const label fieldi
            );

            //- Source term to compressible momentum equation
            virtual void addSup
            (
                const volScalarField& rho,
                fvMatrix<vector>& eqn,
                const label fieldi
            );

            //- Source term to phase-compressible momentum equation
            virtual void addSup
            (
                const volScalarField& alpha,
```

```
            const volScalarField& rho,
            fvMatrix<vector>& eqn,
            const label fieldi
        );


    // IO

        //- Read dictionary
        virtual bool read(const dictionary& dict);
};


// * * * * * * * * * * * * * * * * * * * * * * * * * * * * * * * * * * * * * * * * //

} // End namespace fv
} // End namespace Foam

// * * * * * * * * * * * * * * * * * * * * * * * * * * * * * * * * * * * * * * * * //

#ifdef NoRepository
    #include "movingActuatorDiscTemplates.C"
#endif

// * * * * * * * * * * * * * * * * * * * * * * * * * * * * * * * * * * * * * * * * //

#endif

// ************************************************************************* //
```

C.2. movingActuatorDisc.C

```
/*---------------------------------------------------------------------------*\
  =========                 |
  \\      /  F ield         | OpenFOAM: The Open Source CFD Toolbox
   \\    /   O peration     |
    \\  /    A nd           | www.openfoam.com
     \\/     M anipulation  |
-------------------------------------------------------------------------------
    Copyright (C) 2011-2016 OpenFOAM Foundation
    Copyright (C) 2020 ENERCON GmbH
    Copyright (C) 2018-2020 OpenCFD Ltd
-------------------------------------------------------------------------------
License
    This file is part of OpenFOAM.

    OpenFOAM is free software: you can redistribute it and/or modify it
    under the terms of the GNU General Public License as published by
    the Free Software Foundation, either version 3 of the License, or
    (at your option) any later version.

    OpenFOAM is distributed in the hope that it will be useful, but WITHOUT
    ANY WARRANTY; without even the implied warranty of MERCHANTABILITY or
    FITNESS FOR A PARTICULAR PURPOSE.  See the GNU General Public License
    for more details.

    You should have received a copy of the GNU General Public License
```

```
    along with OpenFOAM.  If not, see <http://www.gnu.org/licenses/>.

\*---------------------------------------------------------------------------*/

#include "movingActuatorDisc.H"
#include "geometricOneField.H"
#include "addToRunTimeSelectionTable.H"

// * * * * * * * * * * * * * * * * Static Data Members * * * * * * * * * * * * * * * //

namespace Foam
{
namespace fv
{
    defineTypeNameAndDebug(movingActuatorDisc, 0);
    addToRunTimeSelectionTable(option, movingActuatorDisc, dictionary);
}
}


const Foam::Enum
<
    Foam::fv::movingActuatorDisc::forceMethodType
>
Foam::fv::movingActuatorDisc::forceMethodTypeNames
({
    { forceMethodType::FROUDE, "Froude" },
    { forceMethodType::VARIABLE_SCALING, "variableScaling" },
});


const Foam::Enum
<
    Foam::fv::movingActuatorDisc::monitorMethodType
>
Foam::fv::movingActuatorDisc::monitorMethodTypeNames
({
    { monitorMethodType::POINTS, "points" },
    { monitorMethodType::CELLSET, "cellSet" },
});


// * * * * * * * * * * * * * * Protected Member Functions  * * * * * * * * * * * * * //

void Foam::fv::movingActuatorDisc::writeFileHeader(Ostream& os)
{
    writeFile::writeHeader(os, "Actuation disk source");
    writeFile::writeCommented(os, "Time");
    writeFile::writeCommented(os, "Uref");
    //writeFile::writeCommented(os, "Cp");
    writeFile::writeCommented(os, "Ct");
    writeFile::writeCommented(os, "x1");
    writeFile::writeCommented(os, "x2");

    if (forceMethod_ == forceMethodType::FROUDE)
    {
```

```
        writeFile::writeCommented(os, "a");
        writeFile::writeCommented(os, "T");
    }
    else if (forceMethod_ == forceMethodType::VARIABLE_SCALING)
    {
        writeFile::writeCommented(os, "Udisk");
        //writeFile::writeCommented(os, "CpStar"); //Arianna
        //writeFile::writeCommented(os, "CtStar"); //Arianna
        writeFile::writeCommented(os, "T");
        //writeFile::writeCommented(os, "P"); //Arianna

    }

    os  << endl;
}


// * * * * * * * * * * * * * * * Private Member Functions  * * * * * * * * * * * //

void Foam::fv::movingActuatorDisc::setMonitorCells(const dictionary& dict)
{
    switch (monitorMethod_)
    {
        case monitorMethodType::POINTS:
        {
            Info<< "    - selecting cells using points" << endl;

            labelHashSet selectedCells;

            List<point> monitorPoints;

            const dictionary* coeffsDictPtr = dict.findDict("monitorCoeffs");
            if (coeffsDictPtr)
            {
                coeffsDictPtr->readIfPresent("points", monitorPoints);
            }
            else
            {
                monitorPoints.resize(1);
                dict.readEntry("upstreamPoint", monitorPoints.first());
            }

            for (const auto& monitorPoint : monitorPoints)
            {
                const label celli = mesh_.findCell(monitorPoint);
                if (celli >= 0)
                {
                    selectedCells.insert(celli);
                }

                const label globalCelli = returnReduce(celli, maxOp<label>());
                if (globalCelli < 0)
                {
                    WarningInFunction
                        << "Unable to find owner cell for point "
                        << monitorPoint << endl;
```

```
                }
            }

            monitorCells_ = selectedCells.sortedToc();
            break;
        }
        case monitorMethodType::CELLSET:
        {
            Info<< "    - selecting cells using cellSet "
                << cellSetName_ << endl;

            monitorCells_ = cellSet(mesh_, cellSetName_).sortedToc();
            break;
        }
        default:
        {
            FatalErrorInFunction
                << "Unknown type for monitoring of incoming velocity"
                << monitorMethodTypeNames[monitorMethod_]
                << ". Valid monitor method types : "
                << monitorMethodTypeNames
                << exit(FatalError);
        }
    }
}


// * * * * * * * * * * * * * * * * * * Constructors  * * * * * * * * * * * * * * * * * //

Foam::fv::movingActuatorDisc::movingActuatorDisc
(
    const word& name,
    const word& modelType,
    const dictionary& dict,
    const fvMesh& mesh

)
:
    cellSetOption(name, modelType, dict, mesh),
    writeFile(mesh, name, modelType, coeffs_),
    forceMethod_
    (
        forceMethodTypeNames.getOrDefault
        (
            "variant",
            coeffs_,
            forceMethodType::FROUDE
        )
    ),
    monitorMethod_
    (
        monitorMethodTypeNames.getOrDefault
        (
            "monitorMethod",
            coeffs_,
            monitorMethodType::POINTS
```

```
        )
    ),
    sink_
    (
        coeffs_.getOrDefault<bool>("sink", true)
      ? 1
      : -1
    ),
    writeFileStart_(coeffs_.getOrDefault<scalar>("writeFileStart", 0)),
    writeFileEnd_(coeffs_.getOrDefault<scalar>("writeFileEnd", VGREAT)),
    diskArea_
    (
        coeffs_.getCheck<scalar>
        (
            "diskArea",
            scalarMinMax::ge(VSMALL)
        )
    ),
    diskDir_
    (
        coeffs_.getCheck<vector>
        (
            "diskDir",
            [&](const vector& vec){ return mag(vec) > VSMALL; }
        ).normalise()
    ),
    UvsCpPtr_(Function1<scalar>::New("Cp", coeffs_)),
    UvsCtPtr_(Function1<scalar>::New("Ct", coeffs_)),

    //start of part added by Arianna
    Umon_
    (
        coeffs_.getCheck<vector>
        (
            "Umon",
            [&](const vector& vec){ return mag(vec) > VSMALL; }
        )
    ),

    rhomon_(coeffs_.getOrDefault<scalar>("rhomon", 1)),

    Amplitudex_(coeffs_.getOrDefault<scalar>("Ax", 0)),
    frequencyx_(coeffs_.getOrDefault<scalar>("fx", 0)),


    delta_Ct_(coeffs_.getOrDefault<scalar>("delta_Ct", 0)),
    phase_Ct_(coeffs_.getOrDefault<scalar>("phase_Ct", 0)),
    frequency_Ct_(coeffs_.getOrDefault<scalar>("frequency_Ct", frequencyx_)),

    point1x_(coeffs_.getOrDefault<scalar>("p1x", 0)),
    point2x_(coeffs_.getOrDefault<scalar>("p2x", 0)),
    point1y_(coeffs_.getOrDefault<scalar>("p1y", 0)),
    point2y_(coeffs_.getOrDefault<scalar>("p2y", 0)),
    point1z_(coeffs_.getOrDefault<scalar>("p1z", 0)),
    point2z_(coeffs_.getOrDefault<scalar>("p2z", 0)),
```

```
    x1(coeffs_.getOrDefault<scalar>("x1_0", point1x_)),
    x2(coeffs_.getOrDefault<scalar>("x2_0", point2x_)),




    radius_
    (
        coeffs_.getCheck<scalar>
        (
            "radius",
            scalarMinMax::ge(VSMALL)
        )
    ),

    // end of part added by Arianna

    monitorCells_()
{
    setMonitorCells(coeffs_);

    fieldNames_.setSize(1, "U");

    applied_.setSize(fieldNames_.size(), false);

    Info<< "    - creating actuation disk zone: " << this->name() << endl;

    Info<< "    - force computation method: "
        << forceMethodTypeNames[forceMethod_] << endl;

    writeFileHeader(file());
}


// * * * * * * * * * * * * * * * * * * Member Functions  * * * * * * * * * * * * * * * * * //

void Foam::fv::movingActuatorDisc::addSup
(
    fvMatrix<vector>& eqn,
    const label fieldi
)
{
    if (V() > VSMALL)
    {
        calc(geometricOneField(), geometricOneField(), eqn);
    }
}


void Foam::fv::movingActuatorDisc::addSup
(
    const volScalarField& rho,
    fvMatrix<vector>& eqn,
    const label fieldi
)
```

```
{
    if (V() > VSMALL)
    {
        calc(geometricOneField(), rho, eqn);
    }
}


void Foam::fv::movingActuatorDisc::addSup
(
    const volScalarField& alpha,
    const volScalarField& rho,
    fvMatrix<vector>& eqn,
    const label fieldi
)
{
    if (V() > VSMALL)
    {
        calc(alpha, rho, eqn);
    }
}


bool Foam::fv::movingActuatorDisc::read(const dictionary& dict)
{
    if (cellSetOption::read(dict) && writeFile::read(dict))
    {
        dict.readIfPresent("sink", sink_);
        dict.readIfPresent("writeFileStart", writeFileStart_);
        dict.readIfPresent("writeFileEnd", writeFileEnd_);
        dict.readIfPresent("diskArea", diskArea_);
        if (diskArea_ < VSMALL)
        {
            FatalErrorInFunction
                << "Actuator disk has zero area: "
                << "diskArea = " << diskArea_
                << exit(FatalIOError);
        }

        dict.readIfPresent("diskDir", diskDir_);
        diskDir_.normalise();
        if (mag(diskDir_) < VSMALL)
        {
            FatalErrorInFunction
                << "Actuator disk surface-normal vector is zero: "
                << "diskDir = " << diskDir_
                << exit(FatalIOError);
        }

        return true;
    }

    return false;
}
```

```
// ************************************************************************* //
```

C.3. movingActuatorDiscTemplates.C

```
/*---------------------------------------------------------------------------*\
  =========                 |
  \\      /  F ield         | OpenFOAM: The Open Source CFD Toolbox
   \\    /   O peration     |
    \\  /    A nd           | www.openfoam.com
     \\/     M anipulation  |
-------------------------------------------------------------------------------
    Copyright (C) 2011-2016 OpenFOAM Foundation
    Copyright (C) 2020 ENERCON GmbH
    Copyright (C) 2018-2020 OpenCFD Ltd
-------------------------------------------------------------------------------
License
    This file is part of OpenFOAM.

    OpenFOAM is free software: you can redistribute it and/or modify it
    under the terms of the GNU General Public License as published by
    the Free Software Foundation, either version 3 of the License, or
    (at your option) any later version.

    OpenFOAM is distributed in the hope that it will be useful, but WITHOUT
    ANY WARRANTY; without even the implied warranty of MERCHANTABILITY or
    FITNESS FOR A PARTICULAR PURPOSE.  See the GNU General Public License
    for more details.

    You should have received a copy of the GNU General Public License
    along with OpenFOAM.  If not, see <http://www.gnu.org/licenses/>.

\*---------------------------------------------------------------------------*/

#include "movingActuatorDisc.H"
#include "fvMesh.H"
#include "fvMatrix.H"
#include "volFields.H"
#include "mathematicalConstants.H"

// * * * * * * * * * * * * * * * Private Member Functions  * * * * * * * * * * * //

template<class AlphaFieldType, class RhoFieldType>
void Foam::fv::movingActuatorDisc::calc
(
    const AlphaFieldType& alpha,
    const RhoFieldType& rho,
    fvMatrix<vector>& eqn
)
{
    switch (forceMethod_)
    {
        case forceMethodType::FROUDE:
        {
            calcFroudeMethod(alpha, rho, eqn);
            break;
        }
```

```
        case forceMethodType::VARIABLE_SCALING:
        {
            calcVariableScalingMethod(alpha, rho, eqn);
            break;
        }

        default:
            break;
    }
}


template<class AlphaFieldType, class RhoFieldType>
void Foam::fv::movingActuatorDisc::calcFroudeMethod
(
    const AlphaFieldType& alpha,
    const RhoFieldType& rho,
    fvMatrix<vector>& eqn
)
{
    const vectorField& U = eqn.psi();
    vectorField& Usource = eqn.source();
    const scalarField& cellsV = mesh_.V();

    // Compute upstream U and rho, spatial-averaged over monitor-region
    vector Uref(Zero);
    scalar rhoRef = 0.0;
    label szMonitorCells = monitorCells_.size();

    for (const auto& celli : monitorCells_)
    {
        Uref += U[celli];
        rhoRef = rhoRef + rho[celli];
    }
    reduce(Uref, sumOp<vector>());
    reduce(rhoRef, sumOp<scalar>());
    reduce(szMonitorCells, sumOp<label>());

    if (szMonitorCells == 0)
    {
        FatalErrorInFunction
            << "No cell is available for incoming velocity monitoring."
            << exit(FatalError);
    }

    Uref /= szMonitorCells;
    rhoRef /= szMonitorCells;

    const scalar Ct = sink_*UvsCtPtr_->value(mag(Uref));
    const scalar Cp = sink_*UvsCpPtr_->value(mag(Uref));

    if (Cp <= VSMALL || Ct <= VSMALL)
    {
        FatalErrorInFunction
           << "Cp and Ct must be greater than zero." << nl
           << "Cp = " << Cp << ", Ct = " << Ct
```

```
            << exit(FatalIOError);
    }

    // (BJSB:Eq. 3.9)
    const scalar a = 1.0 - Cp/Ct;
    const scalar T = 2.0*rhoRef*diskArea_*magSqr(Uref & diskDir_)*a*(1 - a);

    for (const label celli : cells_)
    {
        Usource[celli] += ((cellsV[celli]/V())*T)*diskDir_;
    }

    if
    (
        mesh_.time().timeOutputValue() >= writeFileStart_
     && mesh_.time().timeOutputValue() <= writeFileEnd_
    )
    {
        Ostream& os = file();
        writeCurrentTime(os);

        //os  << Uref << tab << Cp << tab << Ct << tab << a << tab << T << tab
            //<< endl;

          os  << Uref << tab << Ct << tab << x1 << tab << x2
            << tab << T <<
            endl;
    }
}


template<class AlphaFieldType, class RhoFieldType>
void Foam::fv::movingActuatorDisc::calcVariableScalingMethod
(
    const AlphaFieldType& alpha,
    const RhoFieldType& rho,
    fvMatrix<vector>& eqn
)
{
    const vectorField& U = eqn.psi();
    vectorField& Usource = eqn.source();
    const scalarField& cellsV = mesh_.V();

    // Monitor and average monitor-region U and rho
    vector Uref(Zero);
    scalar rhoRef = 0.0;
    label szMonitorCells = monitorCells_.size();

    //for (const auto& celli : monitorCells_) // commented by Arianna
    //{
        //Uref += U[celli]; //commented by Arianna
        //rhoRef = rhoRef + rho[celli]; //commented by Arianna

    //}
    //reduce(Uref, sumOp<vector>()); //commented by Arianna
    //reduce(rhoRef, sumOp<scalar>()); //commented by Arianna
```

```
    //reduce(szMonitorCells, sumOp<label>()); //commented by Arianna


    /*if (szMonitorCells == 0) //Added by Arianna
    {
        FatalErrorInFunction
            << "No cell is available for incoming velocity monitoring."
            << exit(FatalError);
    }*/

   //Uref /= szMonitorCells; //commented by Arianna
    Uref = Umon_;
    const scalar magUref = mag(Uref);
    //rhoRef /= szMonitorCells; commented by Arianna
        rhoRef= rhomon_;


    // Monitor and average U and rho on actuator disk
    vector Udisk(Zero);
    scalar rhoDisk = 0.0;
    scalar totalV = 0.0;

    // for (const auto& celli : cells_) start of part modified by Arianna

    const pointField& ctrs = mesh_.cellCentres(); //added by Arianna.
      //From cylinderToCell.C
    scalar t = mesh_.time().value(); //added by Arianna.
      //From turbinesFoam/actuatorLineSource.C
/*const scalar t =    //Added by Arianna. From writeFile.C
    (
        useUserTime_
      ? fileObr_.time().timeOutputValue()
      : fileObr_.time().value()
    );*/

    Info << "t:" << t << endl;

    scalar x1_new = point1x_ +
      Amplitudex_ * sin(constant::mathematical::twoPi*frequencyx_*t);
    scalar x2_new = point2x_ +
      Amplitudex_ * sin(constant::mathematical::twoPi*frequencyx_*t);
    Info << "x1:" << x1 << endl;
    Info << "x2:" << x2 << endl;
    Info << "x1_new:" << x1_new << endl;
    Info << "x2_new:" << x2_new << endl;


    if (cos(constant::mathematical::twoPi*frequencyx_*t)>0)
        {
        if (x1_new >= x2)
                {
                x2 = x2_new;
                x1 = x1_new;
                }
        }
```

```
if (cos(constant::mathematical::twoPi*frequencyx_*t)<0)
    {
    if (x2_new <= x1)
            {
            x2 = x2_new;
            x1 = x1_new;
            }
    }

 vector point1_(x1, point1y_, point1z_);
 vector point2_(x2, point2y_, point2z_);


 vector axis = (point2_ - point1_);
 scalar magAxis2 = magSqr(axis);
 scalar orad2 = sqr(radius_);


forAll (ctrs, celli)
{

vector d = ctrs[celli] - point1_;
     scalar magD = d & axis;

if ((magD > 0) && (magD < magAxis2))
     {
         const scalar d2 = (d & d) - sqr(magD)/magAxis2;
         if (d2 < orad2)

            {
            Udisk += U[celli]*cellsV[celli];
            rhoDisk += rho[celli]*cellsV[celli];
            totalV += cellsV[celli];
            }
    }
} //end of part modified by Arianna
 reduce(Udisk, sumOp<vector>());
 reduce(rhoDisk, sumOp<scalar>());
 reduce(totalV, sumOp<scalar>());

 if (totalV < SMALL)
 {
     FatalErrorInFunction
         << "No cell in the actuator disk."
         << exit(FatalError);
 }

 Udisk /= totalV;
 const scalar magUdisk = mag(Udisk);
 rhoDisk /= totalV;

 if (mag(Udisk) < SMALL)
 {
     FatalErrorInFunction
         << "Velocity spatial-averaged on actuator disk is zero." << nl
         << "Please check if the initial U field is zero."
```

```
        << exit(FatalError);
}

// Interpolated thrust/power coeffs from power/thrust curves
//const scalar Ct = sink_*UvsCtPtr_->value(magUref);

//formula for the varying thrust coefficient, by Arianna
    const scalar Ct = sink_*(UvsCtPtr_->value(magUref) -
delta_Ct_*cos(constant::mathematical::twoPi*frequency_Ct_*t + phase_Ct_));

Info << "Ct:" << Ct << endl;
const scalar Cp = sink_*UvsCpPtr_->value(magUref);

/*if (Cp <= VSMALL || Ct <= VSMALL)
{
    FatalErrorInFunction
       << "Cp and Ct must be greater than zero." << nl
       << "Cp = " << Cp << ", Ct = " << Ct
       << exit(FatalIOError);
}*/

// Calibrated thrust/power coeffs from power/thrust curves (LSRMTK:Eq. 6)
const scalar CtStar = Ct*sqr(magUref/magUdisk);
const scalar CpStar = Cp*pow3(magUref/magUdisk);

// Compute calibrated thrust/power (LSRMTK:Eq. 5)
 //const scalar T = 0.5*rhoRef*diskArea_*magSqr(Udisk & diskDir_)*CtStar;
//const scalar P = 0.5*rhoRef*diskArea_*pow3(mag(Udisk & diskDir_))*CpStar;

const scalar T = 0.5*rhoRef*diskArea_*sqr(magUref)*Ct; //Arianna
const scalar P = 0.5*rhoRef*diskArea_*pow3(magUref)*Cp; //Arianna
//for (const label celli : cells_) //start of part modified by Arianna

forAll(ctrs, celli)
{ //Added by Arianna

 vector d = ctrs[celli] - point1_;
 scalar magD = d & axis;

if ((magD > 0) && (magD < magAxis2)) //added by Arianna
     {
          scalar d2 = (d & d) - sqr(magD)/magAxis2; //added by Arianna
         if (d2 < orad2) //added by Arianna

            {
            Usource[celli] += (cellsV[celli]/totalV*T)*diskDir_;
            }
    }
 }

if
(
    mesh_.time().timeOutputValue() >= writeFileStart_
 && mesh_.time().timeOutputValue() <= writeFileEnd_
)
{
```

```
        Ostream& os = file();
        writeCurrentTime(os);

        /*os  << Uref << tab << Cp << tab << Ct
            << Udisk << tab << CpStar << tab << CtStar << tab << T << tab << P
            << endl; */ //commented by Arianna

            os  << Uref << tab << Ct << tab << x1 << tab << x2 << tab
            << Udisk << tab << T
            << endl;
    }
}


// ************************************************************************* //
```

C.4. Example of *fvOptions* file

```
/*---------------------------------*- C++ -*----------------------------------*\
| =========                 |
|
| \\      /  F ield         | OpenFOAM: The Open Source CFD Toolbox
|
|  \\    /   O peration     | Version:  3.0.x
|
|   \\  /    A nd           | Web:      www.OpenFOAM.org
|
|    \\/     M anipulation  |
|
\*---------------------------------------------------------------------------*/
FoamFile
{
    version     2.0;
    format      ascii;
    class       dictionary;
    location    "system";
    object      fvOptions;
}
// * * * * * * * * * * * * * * * * * * * * * * * * * * * * * * * * * * * * * //



FoamFile
{
 version 2.0;
 format ascii;
 class dictionary;
 location "constant";
 object fvOptions;
}

disk1
{
  type movingActuatorDisc;
  variant variableScaling;       // variableScaling;
  selectionMode cellSet;
  cellSet actuationDisk1;
```

```
    diskArea 0.19635;
    diskDir (1 0 0);
    writeToFile true;
    sink true;
    Cp 0.5789;
    Ct 0.8;
    delta_Ct 0.2;
    p1x 0;
    p2x 0.0043783;
    p1y 0;
    p2y 0;
    p1z 0;
    p2z 0;
    Ax 0;
    fx 8.753522;
    radius 0.5;
    Umon (11 0 0);
    monitorMethod points;
    monitorCoeffs
    {
        points
        (
            (-5 0 3)
        );
    }
}


// ************************************************************************* //
```

Bibliography

[1] E. Branlard and M. Gaunaa. “Cylindrical vortex wake model: right cylinder”. In: *Wind Energy* 18.11 (Nov. 2015), pp. 1973–1987. ISSN: 10954244. DOI: 10.1002/we.1800.

[2] E. Branlard. *Wind Turbine Aerodynamics and Vorticity-Based Methods, Fundamentals and Recent Applications*. Springer, 2017, p. 634. ISBN: 9783319551630. DOI: 10.1007/978-3-319-55164-7.

[3] E. Branlard, K. Dixon, and M. Gaunaa. “Vortex methods to answer the need for improved understanding and modelling of tip□loss factors”. In: *IET Renewable Power Generation* 7.4 (July 2013), pp. 311–320. ISSN: 1752-1416. DOI: 10.1049/iet-rpg.2012.0283.

[4] T. Burton, N. Jenkins, D. Sharpe, and E. Bossanyi. *Wind Energy Handbook*. Second edition. New York: Wiley, 2011, pp. 39–136. ISBN: 9780470699751.

[5] S. Butterfield, W. Musial, J. Jonkman, and P. Sclavounos. “Engineering Challenges for Floating Offshore Wind Turbines”. In: (Sept. 2007). URL: https://www.osti.gov/biblio/917212.

[6] F. Castellani and A. Vignaroli. “An application of the actuator disc model for wind turbine wakes calculations”. In: *Applied Energy* 101 (2013), pp. 432–440. ISSN: 0306-2619. DOI: https://doi.org/10.1016/j.apenergy.2012.04.039.

[7] Z. Chen, X. Wang, Y. Guo, and S. Kang. “Numerical analysis of unsteady aerodynamic performance of a floating offshore wind turbine under platform surge and pitch motions”. In: *Renewable Energy* 163 (2021), pp. 1849–1870. ISSN: 0960-1481. DOI: 10.1016/j.renene.2020.10.096.

[8] M. Collu and M. Borg. “Design of floating offshore wind turbines”. In: *Offshore Wind Farms: Technologies, Design and Operation*. Ed. by L. Ng, Chong Ng and Ran. Elsevier Ltd, 2016, pp. 359–385. ISBN: 9780081007808. DOI: 10.1016/B978-0-08-100779-2.00011-8.

[9] M. Cormier, M. Caboni, T. Lutz, K. Boorsma, and E. Krämer. “Numerical analysis of unsteady aerodynamics of floating offshore wind turbines”. In: *Journal of Physics: Conference Series* 1037.7 (2018). ISSN: 17426596. DOI: 10.1088/1742-6596/1037/7/072048.

[10] J. Dong and A. Viré. “Comparative analysis of different criteria for the prediction of vortex ring state of floating offshore wind turbines”. In: *Renewable Energy* 163 (2021), pp. 882–909. ISSN: 18790682. DOI: 10.1016/j.renene.2020.08.027.

[11] J. Dong, A. Viré, C. S. Ferreira, Z. Li, and G. Van Bussel. “A modified free wake vortex ring method for horizontal-axis wind turbines”. In: *Energies* 12.20 (2019), pp. 1–24. ISSN: 19961073. DOI: 10.3390/en12203900.

[12] D. M. Eggleston and F. Stoddard. *Wind turbine engineering design*. Van Nostrand Reinhold Company, 1987.

[13] European Commission. *2030 climate and energy goals for a competitive , secure and low-carbon EU economy*. Tech. rep. January. 2014. URL: https://ec.europa.eu/commission/presscorner/detail/en/IP_14_54.

[14] R. Farrugia, T. Sant, and D. Micallef. “A study on the aerodynamics of a floating wind turbine rotor”. In: *Renewable Energy* 86 (2016), pp. 770–784. ISSN: 18790682. DOI: 10.1016/j.renene.2015.08.063.

[15] C. Ferreira, W. Yu, A. Sala, and A. Vire. “Dynamic inflow model for a Floating Horizontal Axis Wind Turbine in surge motion”. In: *Wind Energy Science Discussions* 2021 (2021), pp. 1–22. DOI: 10.5194/wes-2021-34.

[16] H. Glauert. *The analysis of experimental results in the windmill brake and vortex ring states of an airscrew*. 1926.

[17] Global Wind Energy Council. *Global Offshore Wind Report 2020*. Tech. rep. February. 2020, p. 130.

[18] H.Nilsson, ed. *Proceedings of CFD with OpenSource Software*. 2020. URL: http://dx.doi.org/10.17196/OS_CFD#YEAR_2020.

[19] M. O. Hansen, J. N. Sørensen, S. Voutsinas, N. Sørensen, and H. A. Madsen. *State of the art in wind turbine aerodynamics and aeroelasticity*. June 2006. DOI: 10.1016/j.paerosci.2006.10.002.

[20] W. Heronemus. "Pollution-free energy from offshore winds". In: *Proceedings of the 8th Annual Conference and Exposition Marine Technology Society* (Sept. 1972).

[21] IRENA. *Future of Wind: Deployment, investment, technology, grid integration and socio-economic aspects (A Global Energy Transformation paper)*. Tech. rep. Abu Dhabi, 2019, pp. 1–88.

[22] M. Jeon, S. Lee, T. Kim, and S. Lee. "Wake Influence on Dynamic Load Characteristics of Offshore Floating Wind Turbines". In: *AIAA Journal* 54.11 (2016), pp. 3535–3545. DOI: 10.2514/1.J054584.

[23] J. M. Jonkman. "Dynamics of offshore floating wind turbines-model development and verification". In: *Wind Energy* 12.5 (July 2009), pp. 459–492. ISSN: 10954244. DOI: 10.1002/we.347.

[24] M. Karimirad. "Modeling aspects of a floating wind turbine for coupled wave-wind-induced dynamic analyses". In: *Renewable Energy* 53 (May 2013), pp. 299–305. ISSN: 09601481. DOI: 10.1016/j.renene.2012.12.006.

[25] J. Katz and A. Plotkin. *Low-Speed Aerodynamics*. 2nd ed. Cambridge Aerospace Series. Cambridge University Press, 2001. DOI: 10.1017/CBO9780511810329.

[26] K. KODAMA, K. TODA, and M. YAMAMOTO. "Investigation on RANS Computation for an Unsteady Turbulent Flow (In the Case of a Backward-Facing Step Flow with Periodic Perturbation)". In: *Journal of Fluid Science and Technology* 2.3 (2007), pp. 623–632. DOI: 10.1299/jfst.2.623.

[27] G. A. M. van Kuik and L. E. M. Lignarolo. "Potential flow solutions for energy extracting actuator disc flows". In: *Wind Energy* 19.8 (Aug. 2016), pp. 1391–1406. ISSN: 10954244. DOI: 10.1002/we.1902.

[28] R. Kyle, Y. C. Lee, and W. G. Früh. "Propeller and vortex ring state for floating offshore wind turbines during surge". In: *Renewable Energy* 155 (2020), pp. 645–657. ISSN: 18790682. DOI: 10.1016/j.renene.2020.03.105.

[29] M. Lamas and C. Rodríguez. "CFD Applied to Floating Offshore Wind Energy". In: *Floating Offshore Wind Farms*. Ed. by L. Castro-Santos and V. Diaz-Casas. 2016, pp. 126–138. ISBN: 978-3-319-27970-1.

[30] V. Leble and G. Barakos. "10-MW Wind Turbine Performance under Pitching and Yawing Motion". In: *Journal of Solar Energy Engineering, Transactions of the ASME* 139.4 (Aug. 2017). ISSN: 15288986. DOI: 10.1115/1.4036497.

[31] H. Lee and D. J. Lee. "Effects of platform motions on aerodynamic performance and unsteady wake evolution of a floating offshore wind turbine". In: *Renewable Energy* 143 (2019), pp. 9–23. ISSN: 18790682. DOI: 10.1016/j.renene.2019.04.134.

[32] J. G. Leishman. "Challenges in modelling the unsteady aerodynamics of wind turbines". In: *Wind Energy* 5.2□3 (2002), pp. 85–132. DOI: https://doi.org/10.1002/we.62.

[33] Y. Liu, Q. Xiao, A. Incecik, C. Peyrard, and D. Wan. "Establishing a fully coupled CFD analysis tool for floating offshore wind turbines". In: *Renewable Energy* 112 (Nov. 2017), pp. 280–301. ISSN: 18790682. DOI: 10.1016/j.renene.2017.04.052.

[34] H. A. Madsen, R. Mikkelsen, S. Øye, C. Bak, and J. Johansen. "A Detailed investigation of the Blade Element Momentum (BEM) model based on analytical and numerical results and proposal for modifications of the BEM model". In: *Journal of Physics: Conference Series*. Vol. 75. 1. Institute of Physics Publishing, June 2007, p. 012016. DOI: 10.1088/1742-6596/75/1/012016.

[35] S. Mancini, K. Boorsma, M. Caboni, M. Cormier, T. Lutz, P. Schito, and A. Zasso. “Characterization of the unsteady aerodynamic response of a floating offshore wind turbine to surge motion”. In: *Wind Energy Science* 5.4 (2020), pp. 1713–1730. ISSN: 23667451. DOI: 10.5194/wes-5-1713-2020.

[36] D. Micallef and T. Sant. “Loading effects on floating offshore horizontal axis wind turbines in surge motion”. In: *Renewable Energy* 83 (2015), pp. 737–748. ISSN: 18790682. DOI: 10.1016/j.renene.2015.05.016.

[37] P. J. Moriarty and A. C. Hansen. *AeroDyn Theory Manual*. Tech. rep. 2005.

[38] *OpenFOAM: User Guide: k-epsilon*. URL: https://www.openfoam.com/documentation/guides/latest/doc/guide-turbulence-ras-k-epsilon.html.

[39] *Paris Agreement*. URL: https://unfccc.int/documents/37107.

[40] F. Porté-Agel, Y.-T. Wu, H. Lu, and R. J. Conzemius. “Large-eddy simulation of atmospheric boundary layer flow through wind turbines and wind farms”. In: *Journal of Wind Engineering and Industrial Aerodynamics* 99.4 (2011). The Fifth International Symposium on Computational Wind Engineering, pp. 154–168. ISSN: 0167-6105. DOI: https://doi.org/10.1016/j.jweia.2011.01.011.

[41] “Power prediction of wind farms via a simplified actuator disk model”. In: *Journal of Marine Science and Engineering* 8.8 (2020). ISSN: 20771312. DOI: 10.3390/JMSE8080610.

[42] A. Rajan and F. L. Ponta. “A novel correlation model for horizontal axis wind turbines operating at high-interference flow regimes”. In: *Energies* 12.6 (2019). ISSN: 19961073. DOI: 10.3390/en12061148.

[43] J. G. Schepers. “Engineering models in wind energy aerodynamics: Development, implementation and analysis using dedicated aerodynamic measurements”. PhD thesis. Delft University of Technology, 2012, p. 319. ISBN: 978-94-6191-507-8. DOI: https://doi.org/10.4233/uuid:92123c07-cc12-4945-973f-103bd744ec87.

[44] R. Schwarze and F. Obermeier. “Performance and limitations of the unsteady RANS approach”. In: *PAMM* 6.1 (Dec. 2006), pp. 543–544. ISSN: 1617-7061. DOI: 10.1002/PAMM.200610252.

[45] T. Sebastian and M. A. Lackner. “Characterization of the unsteady aerodynamics of offshore floating wind turbines”. In: *Wind Energy* (2012). DOI: 10.1002/we.545.

[46] T. Sebastian and M. Lackner. “Analysis of the induction and wake evolution of an offshore floating wind turbine”. In: *Energies* 5.4 (2012), pp. 968–1000. ISSN: 19961073. DOI: 10.3390/en5040968.

[47] W. Z. Shen, W. J. Zhu, and J. N. Sørensen. “Actuator line/Navier–Stokes computations for the MEXICO rotor: comparison with detailed measurements”. In: *Wind Energy* 15.5 (2012), pp. 811–825. DOI: https://doi.org/10.1002/we.510.

[48] X. Shen, J. Chen, P. Hu, X. Zhu, and Z. Du. “Study of the unsteady aerodynamics of floating wind turbines”. In: *Energy* 145 (2018), pp. 793–809. ISSN: 03605442. DOI: 10.1016/j.energy.2017.12.100.

[49] N. Simisiroglou, H. Polatidis, and S. Ivanell. “Wind farm power production assessment: Introduction of a new actuator disc method and comparison with existing models in the context of a case study”. In: *Applied Sciences (Switzerland)* 9.3 (2019). ISSN: 20763417. DOI: 10.3390/app9030431.

[50] K. Sivalingam, S. Martin, and A. A. S. Wala. “Numerical Validation of Floating Offshore Wind Turbine Scaled Rotors for Surge Motion”. In: *Energies* 11.10 (2018). ISSN: 19961073. DOI: 10.3390/en11102578.

[51] H. Snel and J. Schepers. “Investigation and modelling of dynamic inflow effects”. In: (Mar. 1993).

[52] J. N. Sørensen, W. Z. Shen, and X. Munduate. “Analysis of wake states by a full-field actuator disc model”. In: *Wind Energy* 1.2 (1998), pp. 73–88. ISSN: 10954244. DOI: 10.1002/(sici)1099-1824(199812)1:2<73::aid-we12>3.0.co;2-l.

[53] J. N. Sørensen and A. Myken. “Unsteady actuator disc model for horizontal axis wind turbines”. In: *Journal of Wind Engineering and Industrial Aerodynamics* 39.1-3 (1992), pp. 139–149. ISSN: 01676105. DOI: 10.1016/0167-6105(92)90540-Q.

[54] J. N. Sørensen and W. Z. Shen. “Numerical Modeling of Wind Turbine Wakes ”. In: *Journal of Fluids Engineering* 124.2 (May 2002), pp. 393–399. ISSN: 0098-2202. DOI: 10.1115/1.1471361.

[55] P. R. Spalart and C. L. Rumsey. “Effective inflow conditions for turbulence models in aerodynamic calculations”. In: *AIAA Journal* 45.10 (2007), pp. 2544–2553. ISSN: 00011452. DOI: 10.2514/1.29373.

[56] M. Strach-Sonsalla and M. Muskulus. “Prospects of Floating Wind Energy”. In: *International Journal of Offshore and Polar Engineering* 26.02 (Sept. 2016), pp. 81–87. DOI: https://doi.org/10.17736/ijope.2016.jcr46.

[57] T. T. Tran and D. H. Kim. “A CFD study into the influence of unsteady aerodynamic interference on wind turbine surge motion”. In: *Renewable Energy* 90 (2016), pp. 204–228. ISSN: 18790682. DOI: 10.1016/j.renene.2015.12.013.

[58] T. T. Tran and D. H. Kim. “Fully coupled aero-hydrodynamic analysis of a semi-submersible FOWT using a dynamic fluid body interaction approach”. In: *Renewable Energy* 92 (July 2016), pp. 244–261. ISSN: 18790682. DOI: 10.1016/j.renene.2016.02.021.

[59] T. T. Tran and D. H. Kim. “The aerodynamic interference effects of a floating offshore wind turbine experiencing platform pitching and yawing motions”. In: *Journal of Mechanical Science and Technology* 29.2 (2015), pp. 549–561. ISSN: 09737723. DOI: 10.1007/s12206-015-0115-0.

[60] N. Troldborg. “Actuator Line Modeling of Wind Turbine Wakes”. English. PhD thesis. Jan. 2009. ISBN: 978-87-89502-80-9.

[61] N. Troldborg, J. N. Sorensen, and R. Mikkelsen. “Numerical simulations of wake characteristics of a wind turbine in uniform inflow”. In: *Wind Energy* 13.1 (2010), pp. 86–99. DOI: https://doi.org/10.1002/we.345.

[62] J. de Vaal, M. L. Hansen, and T. Moan. “Effect of wind turbine surge motion on rotor thrust and induced velocity”. In: *Wind Energy* 17.1 (Jan. 2014), pp. 105–121. ISSN: 10954244. DOI: 10.1002/we.1562.

[63] E. N. Wayman, P. D. Sclavounos, S. Butterfield, J. Jonkman, and W. Musial. “Coupled Dynamic Modeling of Floating Wind Turbine Systems: Preprint”. In: (Mar. 2006). DOI: 10.4043/18287-MS.

[64] E. Wayman. *Coupled Dynamics and Economic Analysis of Floating Wind Turbine Systems*. Tech. rep. 2004.

[65] B. Wen, X. Tian, X. Dong, Z. Peng, and W. Zhang. “Influences of surge motion on the power and thrust characteristics of an offshore floating wind turbine”. In: *Energy* 141 (2017), pp. 2054–2068. ISSN: 03605442. DOI: 10.1016/j.energy.2017.11.090.

[66] R. E. Wilson. *Applied aerodynamics of wind power machines,* Corvallis, Or., 1974.

[67] B. Xu, T. Wang, Y. Yuan, Z. Zhao, and H. Liu. “A Simplified Free Vortex Wake Model of Wind Turbines for Axial Steady Conditions”. In: *Applied Sciences* 8.6 (May 2018), p. 866. ISSN: 2076-3417. DOI: 10.3390/app8060866.

[68] W. Yu, V. W. Hong, C. Ferreira, and G. A. van Kuik. “Experimental analysis on the dynamic wake of an actuator disc undergoing transient loads”. In: *Experiments in Fluids* 58.10 (2017). ISSN: 07234864. DOI: 10.1007/s00348-017-2432-9.

[69] W. Yu, D. Tavernier, C. Ferreira, G. A. van Kuik, and G. Schepers. “New dynamic-inflow engineering models based on linear and nonlinear actuator disc vortex models”. In: *Wind Energy* 22.11 (2019), pp. 1433–1450. ISSN: 10991824. DOI: 10.1002/we.2380.